Analysis, Simulation and Measurements of CBS Antennas Loaded with Non-Uniformly Biased Ferrite Material

by

Victor Kononov

A Dissertation Presented in Partial Fulfillment
of the Requirements for the Degree
Doctor of Philosophy

Approved April 2012 by the
Graduate Supervisory Committee:

Constantine A. Balanis, Chair
George Pan
Subramaniam D. Rajan
James T. Aberle

ARIZONA STATE UNIVERSITY

May 2012

ABSTRACT

When ferrite materials are used in antenna designs, they introduce some interesting and unique performance characteristics. One of the attractive features, for example, is the ability to reconfigure the center frequency of the antenna. In addition, ferrite materials also introduce a number of challenges in the modeling and simulation of such antennas.

In order for the ferrite material to be useful in an antenna design, it usually is subjected to an external magnetic field. This field induces the internal magnetic field inside the ferrite material. The internal field plays a pivotal role in the radiation characteristics of the antenna. Thus, from the numerical point of view, accurate computation of this field is critical to the overall accuracy of the analysis. Usually the internal field is non-uniform and its computation is often a rather complex and non-trivial task. Therefore, to facilitate the modeling, simplifying assumptions, which introduce some kind of averaging, are often made.

In this study, ferrite-loaded cavity-backed slot antennas are used to demonstrate that averaging procedures can lead to very unsatisfactory results. For instance, it is common practice to assume that the external field is uniform by averaging its distribution. One of the pivotal points in this study is the demonstration that the external magnetic field plays a very significant role and should be included in the modeling without averaging, if the accurate results are to be attained. Results presented in this study clearly support this argument. A procedure which avoids such averaging is presented and verified by comparing simulations with measurements. In contrast to the previous formulations, the modeling methodology developed in this dissertation leads to accurate results which compare very well with measurements for both uniform and non-uniform field distributions. The utility of this methodology is especially evident for the case when the magnetic field is severely non-uniform.

To my parents: Vera and Georgiy Kononov.

ACKNOWLEDGEMENTS

Special thanks to my advisor Professor Constantine A. Balanis for his guidance, valuable advice and financial support. My sincere appreciation is extended to the other members of the committee Dr. George Pan, Dr. James T. Aberle, and Dr. Subramaniam D. Rajan for their suggestions and evaluation of the content of this dissertation. My very deep gratitude is expressed to Dr. Anastasis Polycarpou for his friendship, professional help, guidance and advice. Special thanks to Craig R. Birtcher for performing numerous measurements to support numerical predictions presented in this dissertation.

I would also like to express sincere appreciation to the Advanced Helicopter Electromagnetics (AHE) program and the U.S. Air-Force AFRL/RYDX (Electronics Exploration Branch) for their financial support of this research.

This dissertation would not be possible without the support and encouragement from my mother Vera Kononova, father Georgiy Kononov, and my sister Vera Kononova. Thank you.

TABLE OF CONTENTS

LIST OF TABLES

LIST OF FIGURES

Chapter 1

INTRODUCTION

The potential of ferrite materials in antenna designs was realized when scholars began systematic observation of their effects on the performance characteristics of the antennas. Many of these effects are a consequence of the non-linear nature of the ferrite materials; in particular, dependence of the permeability of the ferrite on the intensity of the magnetic bias field. For example, a ferrite slab positioned at the aperture of an antenna can introduce a deviation of the main beam from the direction normal to the aperture; this deviation is influenced by small changes in the magnetic field inside the material. Another example is the reconfigurability of the antenna in terms of its center frequency. For instance, if the cavity of the cavity-backed slot (CBS) antenna is loaded with ferrite material, it is possible to change the center frequency of the antenna by varying the strength and/or direction of the magnetic field inside the material. The consequence of such tunability is the increase of the total bandwidth of the antenna; at each frequency in the tunability range the individual bandwidth is still narrow, but the cumulative bandwidth over the entire range of the tunable frequencies is much wider. Thus, ferrite materials can greatly expand the operational characteristics of the antennas; but, they also introduce a number of challenges when it comes to their modeling.

Earlier attempts to investigate the effects on the ferrite materials on the radiation characteristics of the antennas date back to the 50's through 70's [1, 2, 3, 4] when the analysis was performed mainly with measurements. With the advancement of computers and increase in their computational efficiency, full-wave numerical methods became very popular; Method of Moments (MoM) [5, 6], Finite Element Method (FEM) [7], and Finite Difference Time Domain (FDTD) method [8] are presently rec-

ognized as very accurate tools for solving highly complex and analytically intractable problems. Nowadays, many commercially available professional software packages based on these methods exist to assist engineers and scientists in their antenna design, modeling, and simulation. Some of the most notable commercial software are HFSS (Ansys Corporation), WIPL-D Pro (WIPL-D d.o.o.), FEKO [EM Software & Systems-S.A. (Pty) Ltd], CST Studio (Computer Simulation Technology), to name just a few.

What is the problem?

Numerical methods are mathematical tools designed to solve complex practical problems. As such, they rely on the ability of the fundamental theory and mathematical models to accurately describe a given phenomenon. In the case of the ferrite materials, one such model/quantity is known as the *frequency dependent permeability tensor*. It describes the response of the ferrite material to a time-harmonic electromagnetic field.

The expressions for the components of this tensor are known; they depend on the frequency and the magnetic field inside the ferrite material [9]. This field is known as the *internal magnetic field* or the *magnetic bias field*; these terms will be used interchangeably in the following chapters. Because of the non-linear nature of the ferrite materials, the internal magnetic field can be very difficult to compute; therefore, it is not unusual to make various simplifying approximations. Such approximations, however, should be used with great care because their applicability is not always justified and they may lead to very inaccurate simulations.

Modeling and simulation of the magnetic field inside the ferrite material and its effect on the radiation characteristics of the ferrite-loaded CBS antennas constitutes a major part/topic of this work.

Why is it important?

Numerical methods constitute an invaluable tool which many engineers and scientists now rely upon; they are indispensable when it comes to the treatment of the practical problems involving complex structures and unique materials, such as ferrites. However, since these tools rely on mathematical models, an engineer attempting to design and analyze antennas using these tools, and perhaps compare simulations with measurements, should always keep in mind a very important question: "How well the theory and mathematical models represent the actual physical phenomenon?" A good engineer should be aware of the limitations of the mathematical models being used and the possible alternatives when a given model is no longer applicable.

When radiation characteristics of a ferrite-loaded CBS antenna are analyzed numerically, it is necessary to know how the ferrite material responds to time-harmonic electromagnetic fields. The permeability tensor describing this response depends on the internal magnetic field which can be computed/approximated in a number of ways. The overall accuracy of the analysis will depend on the chosen approximation. Therefore, the assessment of the applicability of these approximations is very important.

What has been done?

This study is the continuation of [10] and [11]. The main objective of these contributions was to demonstrate how ferrite-loaded cavity-backed slot antennas can be

modeled accurately. The issue in question is the computation of the magnetic field inside the ferrite material. As will be explained in more detail in the following chapters, this internal field depends on the so called *applied* and *demagnetizing* magnetic fields. To facilitate the analysis, simplifying assumptions regarding these fields are often made.

In [10], the applied and the demagnetizing fields are assumed to be uniform. As a consequence, the internal magnetic field is also uniform; same direction and magnitude everywhere in the ferrite material. However, the actual magnetic field distributions are not uniform; therefore, the assumption of the uniform fields was introduced by averaging these distributions. Although the results presented in [12] are in good agreement with measurements, we were able to show that by removing the above-mentioned assumptions it is possible to obtain slightly more accurate predictions at the expense of a more complex procedure [13].

In [11], a suggestion is made that better accuracy can be achieved if the internal magnetic field is obtained directly by solving the non-linear magnetostatic problem. The results presented in [14] show improvement over the previous results. However, in the formulation of the magnetostatic problem, it is still assumed that the applied magnetic field is uniform (similar averaging procedure as used in [10]). Therefore, the solution for the internal magnetic field is only partially accurate.

What needs to be done?

Despite being widely used, averaging applied magnetic field distribution is not always a good practice. Ignoring the non-uniformities cannot always be justified, which makes the numerical analysis and modeling prone to inaccuracies. In fact, it was demonstrated in [15] that when the non-uniformities are severe averaging the applied

field is unacceptable and leads to inaccurate results. Therefore, in situations when averaging is not an option, an alternative approach capable of providing more reliable results is needed.

What am I going to do?

The objectives of this dissertation are the following:

- Demonstrate the significance of the non-uniform applied magnetic field.
- Demonstrate that the procedures used in [12] and [14] are unable to provide adequate accuracy in designs with severe non-uniformities in the magnetic bias field.
- Demonstrate that to improve the accuracy, the non-uniform applied magnetic field distribution should be incorporated into the modeling.
- Present a procedure for the more accurate modeling of the ferrite-loaded CBS antennas.
- Simulate results and compare with measurements.
- Provide interpretation of the results.

How am I going to do it?

To achieve the objectives, a CBS antenna loaded with non-uniformly biased ferrite material is considered. Non-uniform biasing is achieved by subjecting the ferrite material to a severely non-uniform applied magnetic field. The input impedance of such an antenna is computed using procedures outlined in [12], [14], and the

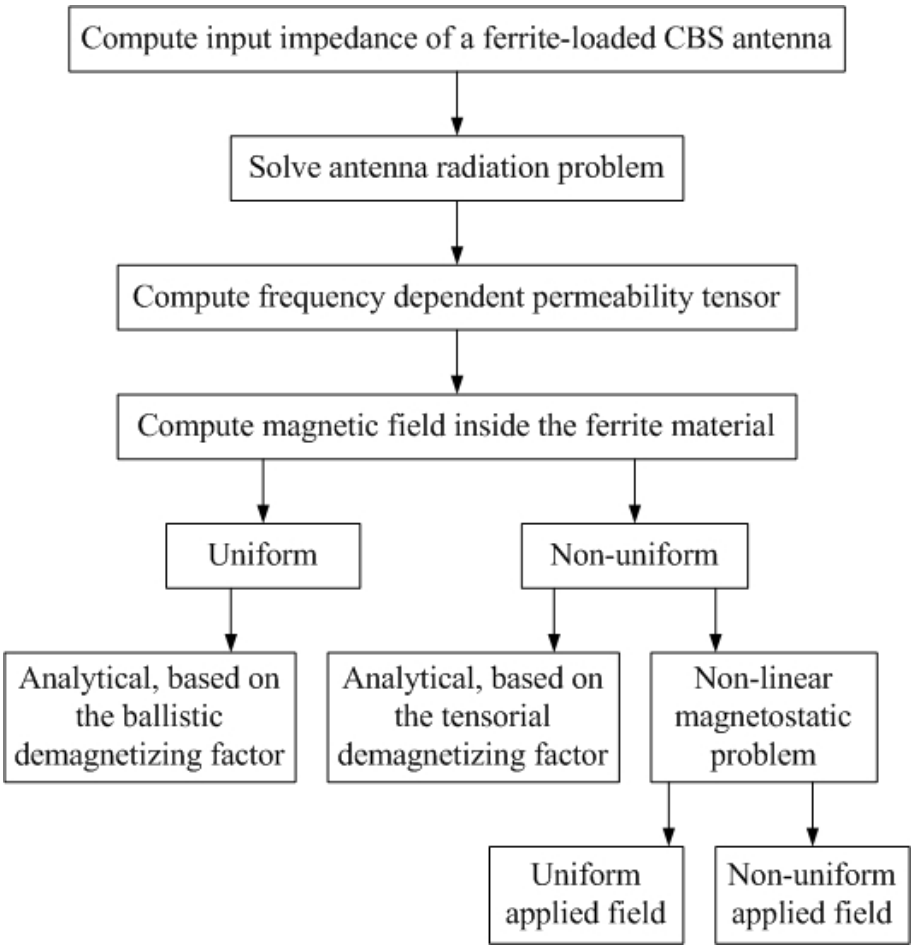

Figure 1.1: Main steps of the numerical analysis.

methodology presented here. Conclusions are drawn by comparing the simulated results with measurements.

Figure 1.1 outlines the main steps involved in the methodology utilized in this dissertation. The primary parameter of interest, the input impedance, is found by solving the antenna radiation problem using the hybrid FEM/MoM technique or pure FEM outlined in Chapter 2. To solve this problem, it is necessary to know the frequency dependent permeability tensor for the ferrite material. Computation of this tensor is discussed in Section 3.2. Since components of the tensor depend on the internal magnetic field, this field should be determined *a priori*. The internal

magnetic field can be assumed uniform or non-uniform. Computation of the uniform field is based on the average applied field and the ballistic demagnetizing factor. This approach was used in [12], and it will be briefly discussed in Section 4.1. Non-uniform internal magnetic field can be computed in a number of ways with varying degree of accuracy. One way is to follow the procedure of [12], but replace the average applied field with the actual field distribution and the ballistic (scalar) demagnetizing factor with its tensorial form. This approach was examined in [13] and will be omitted here. Another way is to solve the non-linear magnetostatic problem. Two options are available: one is to assume the uniform applied field, as in [14], and the other is to include the non-uniform applied field distribution in the modeling. The highlights of the former procedure are presented in Section 4.2. The latter procedure constitutes the main topic of this research; it is discussed in Section 4.3. Comparison of the simulated data with measurements is presented in Chapter 7.

Chapter 2

CAVITY-BACKED SLOT ANTENNAS

Generally speaking, a cavity-backed slot (CBS) antenna is a metallic enclosure which is capable of supporting propagation of the time-varying electromagnetic (EM) waves and allows their radiation through some kind of opening. The enclosure is usually referred to as the cavity or waveguide and the opening is referred to as the aperture. Waveguides and apertures can be of various geometrical shapes, among which rectangular and circular are the most common. The process of establishing time-varying EM fields inside the cavity is referred to as the *excitation* of the cavity. In transmission mode, the most common method of excitation is by means of a metallic probe attached to the inner conductor of the coaxial cable.

CBS antennas belong to the family of the aperture antennas. The most common examples of such antennas are horns and open-ended waveguides [16, 17]. One of the main advantages of the CBS antennas is their low profile. Such antennas are sometimes referred to as conformal antennas because they can be flush-mounted on a surface without significantly affecting its aerodynamic characteristics. In addition, they can be easily protected against harsh environments by simply covering the aperture with a dielectric material. These characteristics make CBS antennas very attractive for airborne platforms [17].

The resonant frequency of a CBS antenna is primarily a function of the cavity dimensions and the electromagnetic properties of the materials filling the cavity. Since majority of the airborne platforms operate in UHF and VHF frequency ranges, and are limited in terms of the available surface area, miniaturization of such antennas is often desirable. Usually, this is achieved by filling the cavity with dielectric materials of high permittivity. However, such miniaturization often leads to reduced

bandwidth and efficiency of the antenna. As an alternative, the cavity can also be loaded with ferrite materials which not only facilitate miniaturization, but also introduce a number of desirable features such as beam steering and reconfigurability (tunability).

2.1 Analysis.

Performance of any antenna is usually described in terms of parameters such as the center frequency, gain, input impedance, polarization, etc. [16]. In order to compute these parameters for the CBS antennas, it is necessary to know the electromagnetic field distributions inside the cavity and at the aperture. Determining these distributions analytically is only possible for a very small set of simple canonical geometries. For example, they are readily available in the literature for the closed rectangular, cylindrical and spherical cavities and infinitely long rectangular and cylindrical waveguides [6]. Practical CBS antennas usually involve open cavities or finite-length waveguides which may contain various, possibly anisotropic, dielectric and magnetic materials. In addition, metallic objects such as the probe and irregular geometrical features, such as the corrugated walls of a horn antenna, may be present. All of these extra features introduce significant variations to the ideal canonical geometry of an empty closed cavity and, as a result, render analytical analysis of practical CBS antennas nearly intractable. In such cases, they are often analyzed using full-wave numerical and computational methods such as the Method of Moments (MoM) and the Finite Element Method (FEM). The general idea behind these methods is the following.

- Divide the entire domain of the problem into smaller domains, usually called elements.

- Assume that the solution in each domain has a particular form. For example, the solution can be assumed to change linearly from one side of the element to the other.
- Substitute this approximation into the original equation describing the problem (integral or differential equation depending on the method) and form a system of algebraic equations.
- Solve this system of equations using direct or iterative methods.

Among the advantages of the finite element method are the relatively simple formulation and the final sparse matrices which can be stored and solved using a variety of well-developed sparse matrix solvers. However, since FEM does not incorporate the Sommerfeld radiation condition, the domain often has to be extended far from the sources, radiators, and scatterers. Such increase in the size of the domain is undesirable because it may significantly increase the computational size of the problem, which leads to the reduced computational efficiency. "A large computational domain not only produces more unknowns but also requires a finer mesh to suppress the dispersion error of the finite element solution" [7].

Integral equation methods (such as the MoM) incorporate the Sommerfeld radiation condition through the use of the appropriate Green's function and handle infinite domains naturally. In addition, they efficiently treat perfectly or highly conducting surfaces. The disadvantage of this method is that it is "difficult to implement for complex structures, and worst of all, it produces full matrices whose treatment requires excessive storage and computing time" [7]. In addition, it does not handle electromagnetically penetrable inhomogeneous materials as well as the FEM does [18].

The choice of the best numerical technique often depends on the problem under consideration. FEM is best for the problems involving closed regions containing various materials. A good problem for the finite element method is, for example, computation of the EM field distribution in a closed cavity loaded with many layers of different materials, including ferrites. MoM, on the other hand, is best for the open-domain problems like, for instance, scattering of the electromagnetic waves by metallic objects.

Numerical analysis of the ferrite-loaded cavity-backed slot antennas is often performed using commercial electromagnetic software, like Ansys HFSS. Alternatively, one may write his/her personal computer code. Advantages of using commercial software are numerous. Such software is usually reliable and versatile, it is fast and computationally efficient, and provides a lot of flexibility at the pre- and post-processing stages. However, many details and intricacies of the involved phenomena are often hidden or not obvious to the user of commercial software. Therefore, writing a personal, "home-built" code has certain advantages as well. Solving a problem from its infancy provides more insight into the fundamental governing processes, and better understanding and interpretation of the results and phenomena. In addition, expressions describing a given phenomenon can be easily modified, should such a need arise. For example, the expressions for the components of the permeability tensor (see Section 3.2) can be easily modified if desired; whereas, in the commercial software, such flexibility is not available. Another obvious advantage is the cost; commercially available professional EM software is usually very expensive. In this study, Ansys HFSS, as well as our own Fortran FEM code, were used to analyze the ferrite-loaded CBS antennas.

2.2 Hybrid FEM/MoM.

As was mentioned in the previous section, analysis of scattering and radiation is often carried out using integral equation methods and/or finite element methods. However, neither of these methods is completely suitable for the analysis of the ferrite-loaded CBS antennas. On the one hand, the problem is open because the cavity radiates into free space, which suggests that the MoM should be used. On the other hand, the problem involves anisotropic ferrite materials, which suggests that the FEM should be used.

To eliminate the disadvantages of the two methods but maintain their advantages, their hybridization was proposed in [19]. The general idea is to divide the total domain of the problem into open and closed regions and use the most appropriate method to formulate the electromagnetic fields in each region. For example, Figure 2.1 shows a CBS antenna mounted on the infinite ground plane and radiating into free space. As far as the numerical analysis is concerned, the domain consists of the cavity, which can be considered as the closed region, and the half-space above the infinite ground plane, which is clearly an open infinite region. Fields inside the cavity can be formulated using FEM; whereas, fields above the ground plane can be formulated using MoM.

Such separation into regions is based on the surface equivalence principle [6]. The two regions are coupled through the aperture in the cavity where the electric and magnetic fields should satisfy the following continuity conditions

$$\hat{z} \times \vec{E}|_{z=0^+} = \hat{z} \times \vec{E}|_{z=0^-} \tag{2.1}$$

$$\hat{z} \times [\nabla \times \vec{E}]_{z=0^+} = \hat{z} \times [\frac{1}{\mu_r} \nabla \times \vec{E}]_{z=0^-} \tag{2.2}$$

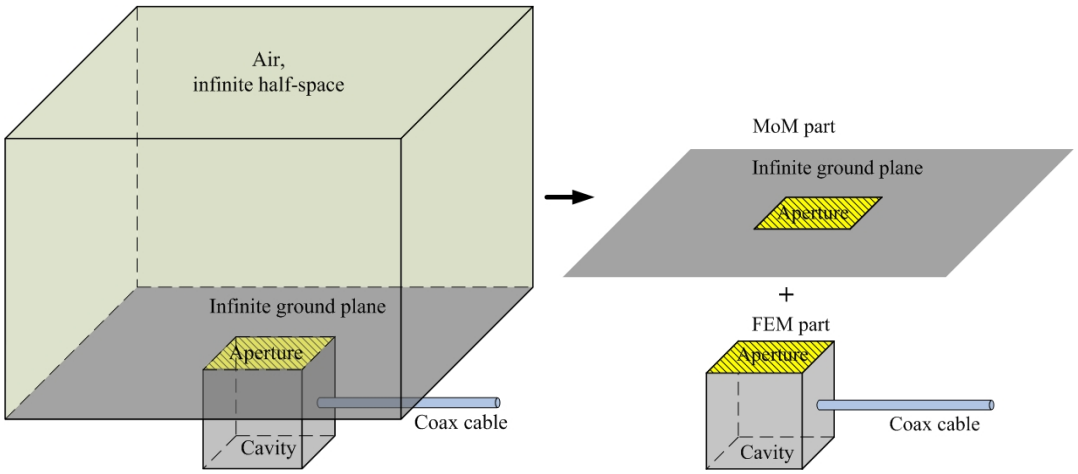

Figure 2.1: General representation of a cavity-backed slot antenna and its separation into open and closed domains for numerical analysis.

These expressions are recognized as the boundary conditions on the tangential components of the electric and magnetic fields across a source free interface between two media [6].

It should be noted that if the hybrid FEM/MoM is not available, the pure FEM is a better candidate for the 'right' numerical technique for our analysis rather than the pure MoM. Even if the domain is infinite, it is still possible to use FEM, as long as the domain is properly closed using some kind of truncating boundary with appropriate boundary conditions. Our simulations using Ansys HFSS are based on the pure FEM method with the first-order ABC or PML closing boundary. The reason why MoM is not applicable is because the problem involves anisotropic ferrite materials. One very powerful commercial software, WIPL-D, which is based on the integral equation method of moments, is quite capable of analyzing very complex structures including cavity antennas loaded with various dielectric materials. However, at the time of writing this work, it does not support anisotropic ferrite materials and therefore cannot be used in our analysis.

One advantage of using the pure FEM over the hybrid FEM/MoM is that the hybrid method relies on the assumption that the ground plane is infinite. Physically, this is not the case. This disadvantage is most noticeable in the simulated radiation patterns. If the ground plane is assumed infinite, some features of the measured radiation patterns cannot be reproduced in the simulations using hybrid FEM/MoM; i.e., the back radiation and the ripple structure of the patterns. However, it is fair to say that such disagreement is usually of secondary importance. Even when the hybrid FEM/MoM with the infinite ground plane is used, the overall agreement between the simulated and measured patterns is very good. If more accurate simulations are required, the hybrid FEM/MoM can be supplemented by the uniform theory of diffraction (UTD) to take into account the effect of the finite ground plane [6, 10].

Our Fortran FEM code is based on the hybrid FEM/MoM technique. The next two sections present an outline of the formulation and the main expressions of this technique. The details of the formulation can be found in [10].

2.3 Boundary Integral Method Formulation.

The boundary integral method is used to formulate the electromagnetic field above the ground plane; region ($z \geq 0$). We assume that this field is generated by some known electric field distribution in the aperture, $\vec{E}_a$. Mathematically, the problem is described by the Helmholtz vector wave equation

$$\nabla \times \nabla \times \vec{E}(\vec{r}) - \beta_o^2 \vec{E}(\vec{r}) = 0 \tag{2.3}$$

and the boundary conditions

$$\vec{E}(\vec{r} = \infty) = 0 \tag{2.4}$$

$$\vec{E}_{tan}(\vec{r} \in \text{ ground plane}) = 0 \tag{2.5}$$

$$\vec{E}(\vec{r} \in \text{ aperture}) = \vec{E}_a \tag{2.6}$$

where the subscript "tan" stands for *tangential*. Solution to this problem is given in terms of the free-space dyadic Green's function $\overline{\vec{G}}_o$ (bar on top denotes dyadic quantity) [7]

$$\vec{E}(\vec{r}) = 2\int_{S_{aper}} [\hat{a}_z \times \vec{E}(\vec{r}')] \cdot [\nabla' \times \overline{\vec{G}}_o(\vec{r}, \vec{r}')] dS' \tag{2.7}$$

where

$$\overline{\vec{G}}_o(\vec{r}, \vec{r}') = \left(\overline{\vec{I}} - \frac{1}{\beta_o^2}\nabla\nabla'\right) \frac{e^{-j\beta_o|\vec{r}-\vec{r}'|}}{4\pi|\vec{r}-\vec{r}'|} \tag{2.8}$$

If the electric field distribution $\vec{E}_a$ were known, we could substitute $\vec{E}(\vec{r}') = \vec{E}_a$ and solve (2.7) for the electric field at any point above the ground plane. Unfortunately, $\vec{E}_a$ is not known *a priori*; therefore, (2.7) will have to be combined with the finite element formulation of the next section to obtain the desired field distributions. The curl of (2.7) is given by

$$\nabla \times \vec{E}(\vec{r}) = 2\beta_o^2 \int_{S_{aper}} (\hat{a}_z \times \vec{E}(\vec{r}')) \cdot \overline{\vec{G}}_o(\vec{r}, \vec{r}') dS' \tag{2.9}$$

2.4 Finite Element Method Formulation.

Electric field inside the cavity and coaxial cable satisfies the Helmholtz vector wave equation

$$\nabla \times ([\mu_r]^{-1}\nabla \times \vec{E}) - \beta_o^2[\varepsilon_r]\vec{E} = 0 \tag{2.10}$$

and the boundary conditions

$$\vec{E}_{tan}(\vec{r} \in \text{ metallic parts}) = 0 \tag{2.11}$$

$$\vec{E}(\vec{r} \in \text{ aperture}) = \vec{E}_a \tag{2.12}$$

$$\vec{E}(\vec{r} \in \text{ coax excitation plane}) = \hat{a}_\rho \frac{E_o}{\rho}(e^{-\gamma z} + Re^{\gamma z}) \tag{2.13}$$

where, E_o is the amplitude of the electric field, $\gamma = \alpha + j\beta_z$, α is the attenuation constant, $\beta_z = \beta_o\sqrt{\epsilon_r\mu_r}$ is the coax wave number, and (ϵ_r, μ_r) are the relative per-

mittivity and permeability of the coaxial cable, respectively, and R is the reflection coefficient.

Approximate solution to this problem can be found using the Finite Element Method; details of the formulation can be found in [12] and appendix A. Cavity and coaxial cable are discretized into smaller elements and the solution within each element is assumed to be of the form

$$\vec{E}^e = \sum_{j=1}^{6} \vec{N}_j^e E_j^e \tag{2.14}$$

where N_j^e are the interpolation functions and E_j^e are the unknown expansion coefficients. The elements are tetrahedra and the unknown expansion coefficients represent the magnitude of the electric field along the edges of an element; each element has six edges [7]. Thus, for each element e, (2.14) can be written in the form of a (6×6) matrix

$$[K^e + Y^e + B^e]\{E^e\} = \{b^e\} \tag{2.15}$$

where

$$K^e = \int_{\Omega^e} (\nabla \times \vec{N}_i) \cdot ([\mu_r]^{-1} \nabla \times \vec{N}_j) - \beta_o^2 \vec{N}_i \cdot ([\varepsilon_r] \vec{N}_j) d\Omega^e \tag{2.16}$$

$$Y^e = -2\beta_o^2 \int_{S^e_{aper}} (\hat{n} \times \vec{N}_i) \cdot \left([\mu_r]^{-1} \int_{S^e_{aper}} (\hat{n} \times \vec{N}_j) \cdot \overline{\overline{G}}_o dS'^e \right) dS^e \tag{2.17}$$

$$B^e = -\gamma \int_{S^e_{coax}} (\hat{n} \times \vec{N}_i) \cdot ([\mu_r]^{-1} \hat{n} \times \vec{N}_j) dS^e \tag{2.18}$$

$$b^e = -2\gamma \int_{S^e_{coax}} (\hat{n} \times \vec{N}_i) \cdot ([\mu_r]^{-1} \hat{n} \times \vec{E}^{inc}) dS^e \tag{2.19}$$

Integrals (2.16, 2.18, 2.19) can be solved analytically and (2.17) should be solved numerically [12].

Chapter 3

FERRITE MATERIALS

There are two basic types of ferromagnetic materials: metallic, and metallic oxide. Metallic ferromagnetic materials have a very complex crystal structure known as the *hexagonal magnetoplumbite structure*. They are used widely as permanent magnets [20]. Common examples of this type are Ferroxdure and the familiar laminated steel used in power transformers.

The other type of the ferromagnetic materials, metallic oxide, is commonly referred to as ferrite. Ferrites are essentially ceramics, they are made by sintering a mixture of various metallic oxides. Ferrites have a variety of crystal structures, two main classes which are used in microwave devices are:

- Spinel ferrites. These are the oldest known ferrites, they are named after and have the same structure as the mineral spinel, $MgAl_2O_4$.
- Garnets. The crystal structure of garnets is more complex, it is that of the classical garnet $Ca_3Fe_2(SiO_4)_3$. The most well known garnet is yttrium-iron garnet (YIG).

Of particular interest to the antenna designers is the absorption loss of the ferrite materials characterized by the quantity known as the *resonance linewidth*, denoted ΔH. Garnets have lower absorption loss than spinel ferrites and, from that point of view, are preferred for the antenna applications. Materials used in this work are manufactured by Trans-Tech. According to their catalog, ΔH for the spinel ferrites is in the range $(150 - 650)$ Oe, and for the microwave garnets, $(10 - 200)$ Oe [21]. Materials used in our measurements and simulations are garnets but they will be referred to as ferrites from now on.

Detailed discussion of the chemical composition and crystal structure of the ferrite materials is outside the scope of this work and can be found elsewhere [22, 23, 24]. What is important, is that the chemical composition and the lattice structure are such that when ferrites are subjected to an external magnetic field, they interact with it by acquiring magnetization. As a matter of fact, all materials interact with the magnetic field. The degree of interaction depends on the presence of permanent magnetic moments in the constituents of the matter (atoms, molecules etc); the interaction is stronger when the magnetic moments are present and weaker when they are absent. Ferrites are known to strongly interact with the magnetic field. The stronger effect is due to the tendency of the magnetic moments to align themselves along the direction of the magnetic field [25], thus producing a net magnetization in the material. (Such description is highly simplified because it ignores the effect of the structure of the crystalline lattice which can have profound effect on the magnetic properties of the material [22].)

The origin of the magnetic moment of an atom is two-fold, it is the combined effect of the electron spin and the electron orbital motion. Spin is the intrinsic property of an electron. This is a quantum mechanical notion which has no analogy in classical physics. Nevertheless, magnetic moment due to spin is often explained by describing the electron as a spinning sphere - "electron behaves as if it were a spinning magnetic top whose magnetic moment lies along its axis of rotation" [24]. The second source of the magnetic moment, electron orbital motion, is due to the assumption that in an atom electrons move around the nucleus. Such orbital motion constitutes tiny loops of current which are commonly called *magnetic dipoles* [26]. So, the total magnetic moment of an atom is the sum of the magnetic moments due to the electron spin and the electron orbital motion. These magnetic moments interact with each other giving rise to the spin-orbit coupling. The measure of this coupling is

called *Landé g-factor*; it is unity for purely orbital motion and two for pure spin [25]. The g-factor is part of the so-called *gyromagnetic ratio* γ, defined as the ratio of the magnetic dipole moment to the angular momentum of a particle. For a free electron, $\gamma = \frac{ge}{2mc}$, where e and m represent charge and mass of the electron and $c \simeq 3 \times 10^8$ (m/s) is the speed of light. According to the Trans-Tech data-sheet, typical values of the g-factor are $1.98 - 2.10$ indicating that spin is the main contributor to the magnetic moment in the ferrite materials. When $g = 2$, the gyromagnetic ratio is $\gamma = 1.76 \times 10^7$ (rad/sec Oe). Gyromagnetic ratio appears in the frequency dependent permeability tensor, as will be shown in Section 3.2.

A ferrite material can be viewed as an assembly of magnetic moments. These moments interact with the static, as well as the time-varying magnetic fields. It is important to know how ferrites interact with these fields. There are a number of properties which characterize this interaction, the following three are the most relevant in our analysis:

- Initial magnetization curve or B-H curve. It represents the relationship between the static magnetic field H and the static magnetic induction B inside the ferrite material. Essentially, it gives the static permeability of the ferrite material. This property is relevant for the magnetostatic analysis.

- Saturation magnetization. This is the maximum value of the initial magnetization curve. It is relevant for both, magnetostatic and RF analysis.

- Resonance linewidth. This property characterizes the absorption loss of the ferrite material. It is relevant for the RF analysis.

3.1 Ferrite Materials in Static Magnetic Field.

As was mentioned in the previous section, ferrite materials can be viewed as an assembly of magnetic moments. In the absence of an external magnetic field, all magnetic moments have random orientations and their vector sum is zero. When a static external magnetic field is applied, moments begin to rotate in the attempt to align themselves in the direction of the applied field. But, in doing so they must overcome the energy of the thermal agitation which tends to destroy the alignment. A simple 'order of magnitude' comparison of the thermal and potential energies of a single magnetic moment in the presence of the applied magnetic field shows that very strong fields ($\sim 10^8$ A/m) are needed to overcome the thermal agitation. On the other hand, it is an experimental fact that fields of the order of $10 - 10^2$ A/m are sufficient to induce magnetization [27]. Solution to this problem was proposed in 1907 by Weiss who suggested that "ferromagnetic materials could exhibit a large spontaneous magnetization even at low fields because the elementary magnetic moments were by no means independent but were strongly coupled by an internal field proportional to the magnetization itself, which he termed molecular field" [27]. He also postulated that "a ferromagnetic material is subdivided into regions, called magnetic domains. In each domain, the degree of magnetic moment alignment is dictated by the molecular field, but the orientation of the spontaneous magnetization can vary from domain to domain" [27]. Today, the existence of the magnetic domains is an observable experimental fact. Figure 3.1 depicts cartoon representation of the domain structure for the demagnetized and partially magnetized ferrites. The arrows indicate orientation of the net magnetic moment in the domains. Domain structure represents the balance between different competing energies (exchange energy, magneto crystalline anisotropy, magnetostatic energy) such that the total energy is minimum.

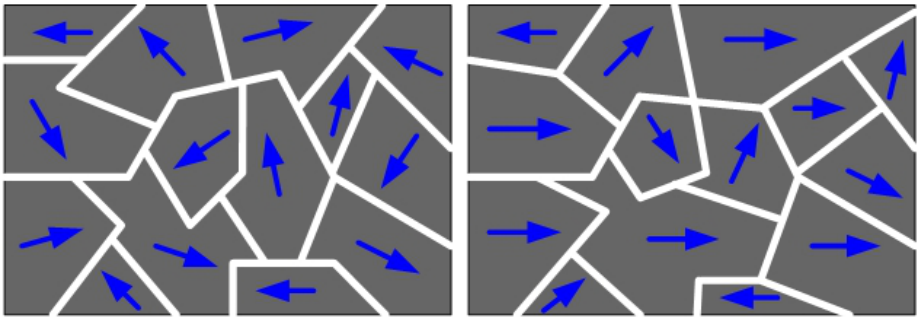

(a) Demagnetized. (b) Partially magnetized.

Figure 3.1: Ferrite magnetic domains.

When ferrite material is subjected to an external magnetic field, it responds by acquiring a certain magnetization, usually denoted as $\vec{M}$. The situation is analogous to the polarization of the dielectrics under the influence of the applied electric field. Unlike in dielectrics, however, magnetization in magnetic materials is a non-linear function of the magnetic field. The well known constitutive relationship between the magnetization $\vec{M}$ and the magnetic field $\vec{H}$ is $\vec{M} = \chi\vec{H}$, where χ is the magnetic susceptibility. When χ is constant, $\vec{M}$ is a linear function of $\vec{H}$. In ferromagnetic materials, the susceptibility χ is itself a function of $\vec{H}$; in such a case, the relationship $\vec{M} = \chi\vec{H}$ is non-linear. Thus, magnetic flux density is also a non-linear function of the magnetic field, $\vec{B} = \mu(\vec{H})\vec{H}$, where permeability $\mu = 1 + \chi$. Such a non-linear relationship can be quite complex. Figure 3.2a shows typical $\vec{B}$ *vs.* $\vec{H}$ and μ *vs.* $\vec{H}$ curves which clearly demonstrate the non-linear dependence of the magnetic flux on the magnetic intensity [28].

Non-linear behavior of the magnetization vector can be explained in terms of the domain processes. With reference to Figure 3.2b, the process of macroscopic magnetization occurs in three stages [28, 29]:

a) In weak fields, the domains with the same orientation as the applied magnetic field grow at the expense of the domains with the opposite orientation. This stage is sometimes called *domain growth*.

b) In medium fields, magnetic moments having different orientation acquire enough energy to rotate to the direction nearest to the field direction. This stage is sometimes called *domain rotation*.

c) In strong fields, the process of *coherent rotation* takes place. Coherent rotation occurs when the applied field is sufficiently intense to supply all magnetic moments with enough energy to overcome all other energies and align themselves with the direction of the applied field. The result is a single-domain sample. This state of the ferrite material is called *technical saturation*. Further increase in the strength of the applied magnetic field will only yield a very slow increase in the magnitude of the magnetization.

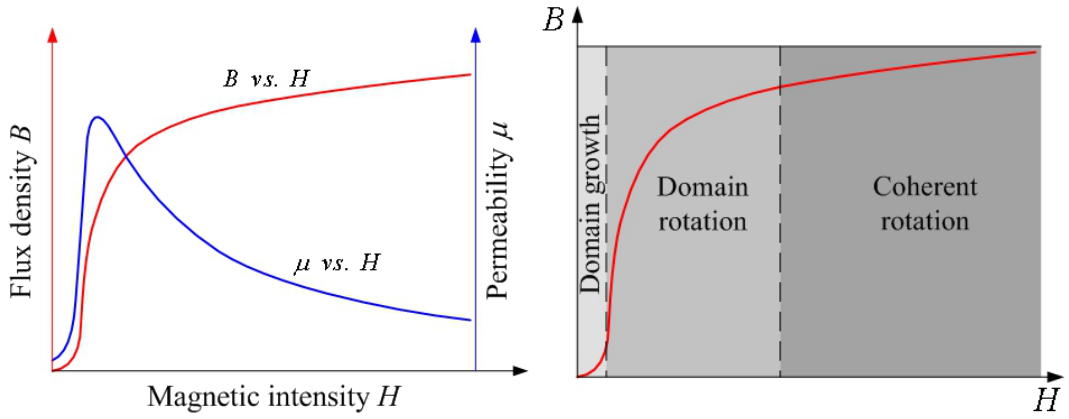

(a) Typical curves. (b) Domain processes.

Figure 3.2: Non-linear dependence of the magnetic flux on the magnetic intensity.

The knowledge of the B-H curves is essential for the non-linear magnetostatic analysis. Usually they are provided by the manufacturer of the ferrite materials. If only one curve is provided, then it is assumed that the material is isotropic in the

static magnetic field; abscissa of such a curve represents the magnitude of the internal magnetic field $|\vec{H}|$ and the ordinate represents the magnitude of the internal magnetic induction $|\vec{B}|$. If the ferrite is anisotropic in the static magnetic field, then several curves, one for each principal direction, are needed to fully describe its response to the magnetic field [30]. Very often these curves are not available, in which case they are approximated using various mathematical model [27, 31, 32, 33].

3.2 Ferromagnetic Resonance.

When a magnetic moment is subjected to a magnetic field, it tends to rotate and align with the direction of the field, trying to minimize its energy. However, the magnetic moment due to a spinning electron behaves differently because a spinning electron behaves like a gyroscope; instead of spinning in the gravitational field, it spins in the magnetic field. Figure 3.3a shows a gyroscopical motion of a spinning electron in the static magnetic field H. As can be seen, it implies that the magnetic top of the magnetic moment follows a circular trajectory about the direction of the applied field. It should be noted that the spinning top, if free to precess under the action of an external field H, will maintain its inclination angle θ with respect to the field. "No matter how strong the force applied may be, the only effect of increasing the force on the freely precessing top is to make the precession faster" [34]. In other words, the applied magnetic field will not change the direction of the magnetic moment of a freely spinning electron.

Such gyroscopical motion implies that an initially randomly oriented magnetic moment will remain randomly oriented even after the application of the magnetic field, which means that it would be impossible to magnetize the material [23]. This, obviously, contradicts the experimental fact that ferrites acquire magnetization when subjected to an external magnetic field. The contradiction can be resolved by taking

into account the damping forces such as friction. Under the influence of these forces, "...any gyroscope when set in motion and left to precess, will slowly spiral to its equilibrium position" [24]. This situation is illustrated in Figure 3.3b where the total damping force is directed towards the axis of precession. Thus, when damping forces are accounted for, magnetic moment of a spinning electron will eventually align with the direction of the applied magnetic field; as a result, magnetization becomes possible.

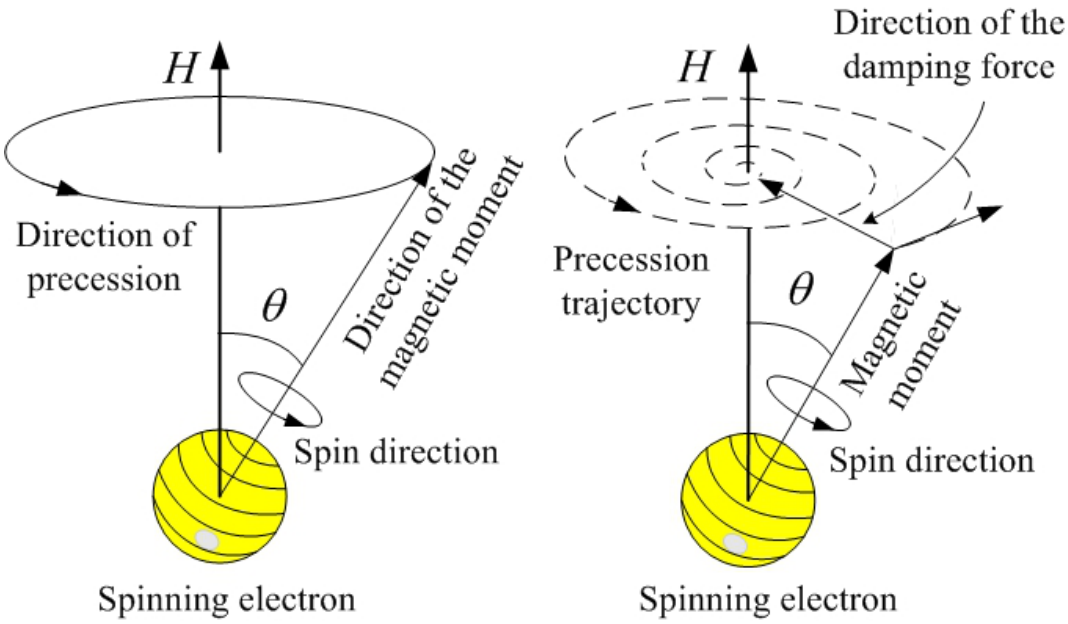

(a) Precession without damping.

(b) Precession with damping.

Figure 3.3: Precession of the magnetic moment in the static magnetic field.

Suppose that a small alternating magnetic field is superimposed on to the already present static magnetic field. For the sake of simplicity, let the alternating magnetic field be such that its magnitude is varying in a linear fashion perpendicular to the direction of the static field; if the static field is in the z-direction, the dynamic field is in the xy-plane and it may be assumed, without the loss of generality, that it is varying along, say, the x-direction. As a result, the total magnetic field (static plus dynamic) will exhibit mild (provided that the amplitude of the dynamic field is

small) oscillations between directions A and B as shown in Figure 3.4. Let's assume that initially the electron spin axis is vertical under the influence of the magnetic force H. "If the direction of the force H is suddenly altered to the position A, the electron, behaving like a gyroscope, will precess about the axis A along the circular path a-b. If, when the electron has reached position b, the direction of the force H changes to the position B, the electron axis will precess along the new circular path b-c" [24].

The alternating field supplies energy to the electron. If the energy is supplied at the correct rate, the precession orbit (inclination angle) of the electron will grow larger and larger. Damping forces, however, oppose such behavior. The effect of damping therefore is such that some of the energy is absorbed or transferred to another form like heat. Such exchange of energy eventually reaches an equilibrium and the precession/inclination angle reaches a finite value. This phenomenon is referred to as *resonance absorption*.

Ferromagnetic resonance was discovered by Griffith (1946), and the theory of the resonance effect was proposed by Kittel (1948) [35, 36]. Polder showed in 1949 that the frequency dependent permeability is a rank two tensor [37].

$$\mu = \begin{bmatrix} \mu_{xx} & \mu_{xy} & \mu_{xz} \\ \mu_{yx} & \mu_{yy} & \mu_{yz} \\ \mu_{zx} & \mu_{zy} & \mu_{zz} \end{bmatrix} \tag{3.1}$$

Derivation of the expressions for the components of this tensor can be found in almost any book covering ferrite materials [23, 38]. It is common practice to assume that the internal magnetic field is unidirectional (has only one component). When the field is not unidirectional, the derivation follows the same steps and the

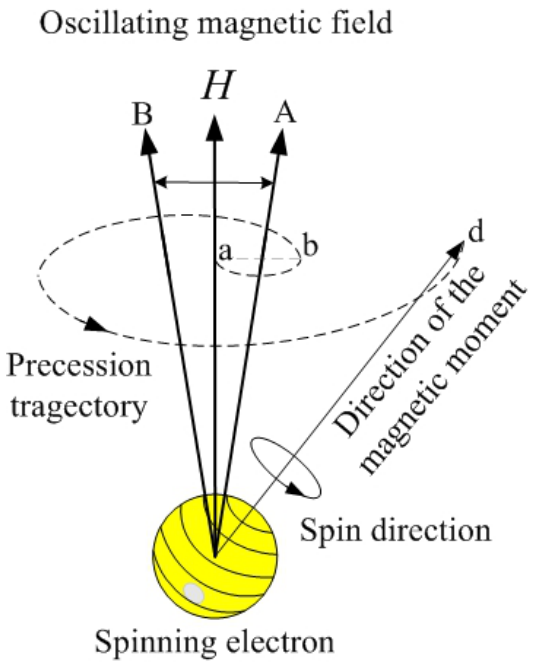

Figure 3.4: Precessional motion of a spinning electron in a magnetic field which oscillates between the directions A and B.

permeability tensor can be written as [39, 40]

$$[\mu] = I + (-\chi[R][R] - j\kappa[R]) \tag{3.2}$$

where, I is the (3×3) identity matrix and

$$\chi \equiv \frac{\omega_m \omega_o}{\omega_o^2 - \omega^2} \ , \quad \kappa \equiv \frac{\omega \omega_o}{\omega_o^2 - \omega^2} \tag{3.3}$$

$$[R] \equiv \begin{bmatrix} 0 & -\cos(\theta_z) & \cos(\theta_y) \\ \cos(\theta_z) & 0 & -\cos(\theta_x) \\ -\cos(\theta_y) & \cos(\theta_x) & 0 \end{bmatrix} \tag{3.4}$$

In (3.3), $\omega_m = \gamma M_s$, $\omega_o = \gamma(H + j\frac{\Delta H}{2})$, $\gamma = \frac{g}{2} 1.7588 \times 10^{11}$ is the gyromagnetic ratio, g is the Landé factor, M_s is the saturation magnetization, $H = |\vec{H}^i|$ is the magnitude of the magnetic field inside the ferrite material. In (3.4), the direction cosines are defined as $\cos(\theta_j) = \frac{H_j^i}{|\vec{H}^i|}$ where $j = x, y, z$.

When $\vec{H}^i$ is in the arbitrary direction, (3.2) is, in general, a full tensor with no zero entries. However, if $\vec{H}^i$ is unidirectional, (3.2) reduces to the well known expressions usually found in the literature [9]. For example, if the internal magnetic field has only x component, (3.2) becomes

$$[\mu] = \begin{bmatrix} 1 & 0 & 0 \\ 0 & \mu & j\kappa \\ 0 & -j\kappa & \mu \end{bmatrix} \tag{3.5}$$

where the diagonal components are defined as $\mu = 1 + \chi$.

Chapter 4

INTERNAL MAGNETIC FIELD

As was mentioned in Section 3.1, all materials interact with the external magnetic field. This interaction depends on the presence of the magnetic moments in the constituents of matter and is most prominent in ferromagnetic materials. Macroscopically, such interaction can be described in simple terms by considering the following three magnetic fields:

- Applied (external) magnetic field.
- Demagnetizing magnetic field.
- Internal (biasing) magnetic field.

The *applied magnetic field* $\vec{H}^a$ is produced by the macroscopic sources such as permanent magnets and electromagnets. This is the field in the vacuum around the source, i.e., in the absence of all other materials. When a ferromagnetic material like ferrite is submerged in this field, it acquires a non-zero magnetization in the direction of the applied field. It is said that the material is magnetized. The consequence of such magnetization is the induced magnetic field referred to as the *demagnetizing magnetic field* $\vec{H}^d$; it is usually in the opposite direction to the applied field. Thus, the total field inside the material is the superposition of the applied and the demagnetizing fields. The resultant field is usually called the *internal magnetic field* $\vec{H}^i$. In equation form, these fields are related by

$$\vec{H}^i = \vec{H}^a + \vec{H}^d \tag{4.1}$$

The magnetic field H appearing in the permeability tensor (3.2) through ω_o is such an internal field. Accurate computation of this quantity is a non-trivial

task; therefore, to facilitate the analysis, simplifying assumptions are often made. One of the simplest and most common simplifications is to assume that the internal field is uniform (same direction and magnitude everywhere in the ferrite material). There are cases when this assumption is valid and reasonably accurate results can be achieved [12]. However, fundamentals of electromagnetism tell us that this field cannot possibly be totally uniform because of the following:

- The internal magnetic field is the result of the applied magnetic field which is produced by the permanent magnets or electromagnets. The intensity of the applied field is inversely proportional to the square of the distance from the source. Thus, the intensity of the internal field must also be a function of distance.

- The magnetic field has to satisfy boundary conditions at the interfaces between different media. Satisfying these boundary conditions will inevitably introduce non-uniformities in the demagnetizing magnetic field, which will consequently introduce non-uniformities in the internal field distribution. For this reason, even if the applied field is uniform, the internal field is still non-uniform.

- Flux lines of the magnetic field have to form closed loops, which means that, in general, the direction of the field cannot remain constant.

These reasons tell us that the assumption of the uniformity of the internal magnetic field may easily be faulty. This may lead to significant inaccuracies in the computation of the permeability tensor which most probably will lead to very inaccurate simulations of the antenna radiation characteristics.

4.1 Uniform Field: *Approach 1.*

The most common approach to computing the internal magnetic field $\vec{H}^i$ is based on the following equation

$$\vec{H}^i = \vec{H}^a + \vec{H}^d \tag{4.2}$$

where $\vec{H}^i$, $\vec{H}^a$, and $\vec{H}^d$ are the internal, applied, and demagnetizing magnetic fields, respectively. The applied magnetic field can be found by solving the magnetostatic problem using, for instance, the Finite Element Method (see Sections 5.1 and 5.2). Computing the demagnetizing field is more difficult, but it can sometimes be expressed as [41]

$$H_i^d = -4\pi \sum_j N_{ij} M_j \tag{4.3}$$

where M_j represents the components of the magnetization vector and N_{ij} the elements of the demagnetizing tensor, $(i, j = x, y, z)$.

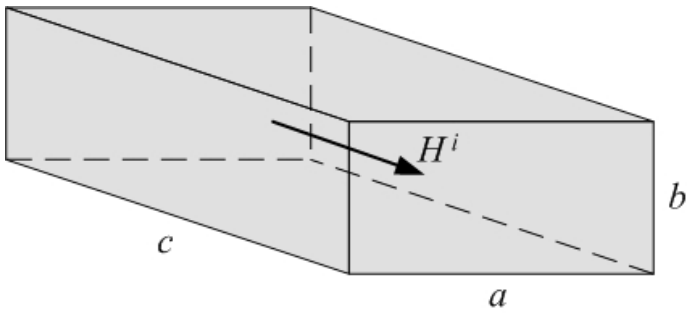

Figure 4.1: General designation of the dimensions of the ferrite material for use in equation 4.5.

The vector equation 4.2 can be simplified if all the quantities are assumed to be scalar

$$H^i = H^a_{ave} - 4\pi M_s N_b \tag{4.4}$$

where H^a_{ave} represents the volumetric average of the applied field, $4\pi M_s$ is the satu-

ration magnetization, and N_b is the ballistic demagnetizing factor [42]

$$\begin{aligned} N_b &= \frac{1}{2\pi pq}\left[4pq\cot^{-1}\left(\frac{h(p,q)}{4pq}\right)\right. \\ &+ qH(p,q)+pH(q,p)-qH(0,q)-pH(0,p) \\ &+ \left. h(0,q)+h(0,p)-h(p,q)-1\right] \end{aligned} \tag{4.5}$$

where

$$h(u,v) = \sqrt{1+4u^2+4v^2} \tag{4.6}$$

$$H(u,v) = \ln\left[\frac{h(u,v)+2v}{h(u,v)-2v}\right] \tag{4.7}$$

$$p=\frac{a}{c} \quad , \quad q=\frac{b}{c} \tag{4.8}$$

and a, b, c are the dimensions of the ferrite material designated in such a way that the magnetic field is along c as shown in Figure 4.1.

Equation 4.4 is currently the most widely used expression for the internal magnetic field [9, 25, 38]. It was also used for the analysis of the ferrite-loaded CBS antennas in [12]. This procedure will be referred to as *Approach 1*. In summary, it consists of the following steps:

- Remove all the materials from the cavity and compute/measure the applied magnetic field in the volume of the cavity where the ferrite material will be.
- Compute the average applied magnetic field H^a_{ave}.
- Compute the ballistic demagnetizing factor (4.5).
- Compute the demagnetizing field $H^d = 4\pi M_s N_b$.
- Compute the internal magnetic field (4.4).

The advantage of this procedure is that it is straightforward, transparent and relatively simple. But, it suffers from some disadvantages which impede its accuracy.

First of all, in order to use it, explicit knowledge of the applied and demagnetizing fields is required. As was already pointed out, computation of the applied field usually does not pose significant difficulties but the demagnetizing field can be quite problematic. Unfortunately, closed-form expressions based on the tensorial and ballistic demagnetizing factors do not guarantee accurate computation of this field. Therefore, even though the applied field in (4.4) can be computed quite accurately, the demagnetizing term is often very approximate and can be a major source of inaccuracies in this approach. Another drawback is that the applied, demagnetizing, and internal fields are all uniform quantities. It was pointed out that, in general, it is not true and in the cases of very severe non-uniformities such an approximation may lead to significant errors.

This approach was also employed in [39, 13] where the vector equation 4.2 is used instead of (4.4). The applied field is found using FEM and the components N_{ij} of the demagnetizing tensor are computed using analytical expressions derived in [41]. In (4.3), the magnetization $\vec{M}$ is assumed to be in the same direction as the internal field $\vec{H}^i$ and its components are written as $M_j = 4\pi M_s \frac{H_j^i}{|\vec{H}^i|}$. Details of the formulation and procedure can be found in the provided references. Suffice it to say, it was possible to achieve slightly more accurate results by using the vector equation 4.2 instead of its scalar counterpart (4.4).

4.2 Non-uniform Field: *Approach 2.*

To avoid explicit computation of the demagnetizing field $\vec{H}^d$, an alternative approach was suggested in [14] where the internal field $\vec{H}^i$ is found by solving the non-linear magnetostatic problem. This approach will be referred to as *Approach 2.*

- Remove all materials from the cavity and compute/measure the applied magnetic field in the volume of the cavity where the ferrite material will be.
- Compute the average applied magnetic field.
- Solve the non-linear magnetostatic problem for the internal magnetic field using the total scalar potential formulation.

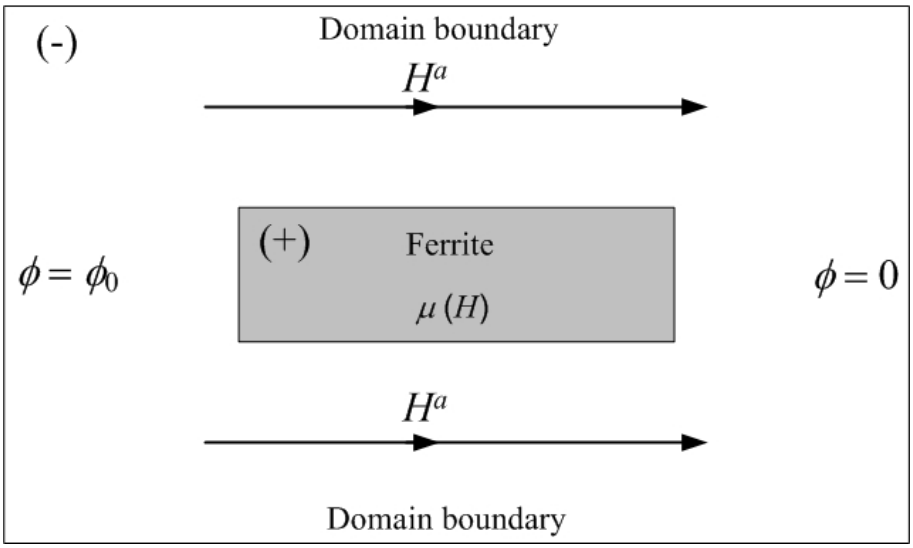

Figure 4.2: Domain of a non-linear problem for total potential formulation.

A non-linear problem that can be tackled by this approach is shown graphically in Figure 4.2. The entire domain of the problem consists of the ferrite material and the free space around it. It is important that the domain does not contain any magnetic sources. In such a case, the magnetic field satisfies the following source-free static Maxwell equations:

$$\nabla \times \vec{H} = 0 \ , \quad \nabla \cdot \vec{B} = 0 \tag{4.9}$$

From the curl equation, it follows that $\vec{H} = -\nabla\phi$ where ϕ is referred to as the *total scalar potential*. Using the constitutive relationship $B = \mu H$ and substituting for H, the divergence equation becomes $-\nabla \cdot \mu\nabla\phi = 0$. If the computational domain is

divided into regions occupied by the magnetic material, denoted by the superscript '+', and free space, denoted by the superscript '−', then (4.9) can be reformulated in terms of the total scalar potential

$$\nabla \cdot (\mu^+ \nabla \phi^+) = 0 \tag{4.10}$$

subject to the continuity conditions

$$\phi^+ = \phi^- \tag{4.11}$$

$$\mu^+ \frac{\partial \phi^+}{\partial n} - \mu^- \frac{\partial \phi^-}{\partial n} = 0 \tag{4.12}$$

In the actual physical setup, the ferrite material is subjected to the applied magnetic field generated by the magnetic sources such as permanent magnets and/or electromagnets. Since this formulation does not support magnetic sources, the applied field has to be specified in some way other than modeling the actual sources. One way to do it is through boundary conditions, by enforcing a potential difference on the opposite walls of the domain. Figure 4.2 shows that the potential on the left wall is set to $\phi = \phi_0$ and the potential on the right wall is set to zero, $\phi = 0$. Such boundary conditions ensure that the entire domain is permeated by the uniform magnetic field denoted H^a. This field is supposed to emulate the effect of the applied magnetic field produced by the actual magnetic sources.

The advantage of this procedure is that it does not require explicit computation of the demagnetizing field. The computed internal magnetic field is presumably more accurate because this approach is more rigorous in taking into account the effect of the finite dimensions of the ferrite material. It relies on the fundamental principles of electromagnetism to properly enforce the continuity condition of the magnetic field at the air-ferrite interface. The disadvantage of this formulation is that it does not support modeling of the magnetic sources, which precludes accurate representation of complex, real applied magnetic fields. Most of the time, the

applied field is modeled as uniform by simply specifying the potential difference on the opposite walls of the domain. As was discussed in the beginning of this chapter, the applied field is one of the sources of the non-uniformities in the internal field. When the applied field is severely non-uniform, so is the internal field. Ignoring such non-uniformities will most probably lead to inaccurate analysis. Thus, even though Approach 2 does alleviate some drawbacks of Approach 1, it still relies on one potentially serious approximation.

4.3 Non-uniform Field: *Approach 3.*

The approach presented in this section attempts to improve upon the drawbacks of Approach 2; namely, incorporate the modeling of the applied magnetic field in the formulation. This approach will be referred to as *Approach 3.*

To include the applied magnetic field in the modeling, we need to be able to solve a non-linear magnetostatic problem graphically illustrated in Figure 4.3. Contrary to the domain depicted in Figure 4.2, this domain consists of the sources of the magnetic field (coils, permanent magnets, electromagnets), denoted by J, ferrite material, and surrounding free space. The problem statement is the following: "Knowing current J, what is the magnetic field $\vec{H}^i$ inside the ferrite material?" There are a number of ways such a magnetostatic problem can be formulated. We use the reduced scalar potential approach [43].

The magnetic fields $\vec{B}$ and $\vec{H}$ satisfy the static Maxwell equations

$$\nabla \times \vec{H} = \vec{J}\,, \quad \nabla \cdot \vec{B} = 0 \tag{4.13}$$

where $\vec{J}$ is the known current density. Magnetic field $\vec{H}$ can be expressed as the superposition of two fields

$$\vec{H} = \vec{H}_{BS} + \vec{H}_m \tag{4.14}$$

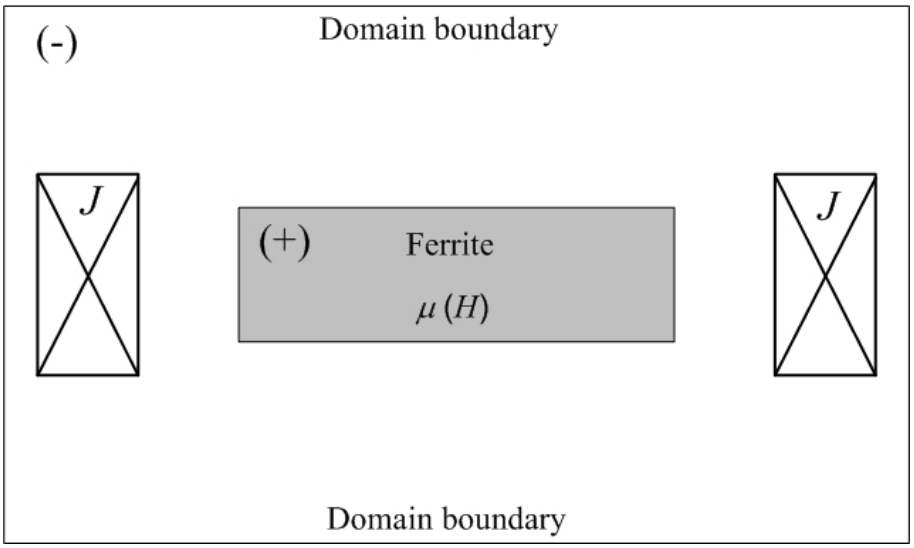

Figure 4.3: Domain of a non-linear problem for reduced scalar potential formulation.

where $\vec{H}_{BS}$ is the field produced by the current density $\vec{J}$ in the absence of all materials and $\vec{H}_m$ is the field due to the magnetization of the ferrite material. $\vec{H}_{BS}$ can be computed using the Biot-Savart Law [26]; its curl and divergence are given by $\nabla \times \vec{H}_{BS} = \vec{J}$ and $\nabla \cdot \vec{B}_{BS} = 0$, respectively. Therefore, when (4.14) is substituted in (4.13), it is found that the field $\vec{H}_m$ is irrotational and can be expressed as the gradient of some scalar potential, $\vec{H}_m = -\nabla\phi_m$. Potential ϕ_m is referred to as the *reduced scalar potential*.

If the computational domain is divided into regions with magnetic materials, denoted by the superscript '$^+$', and regions with sources, denoted by the superscript '$^-$', the original problem (4.13) can be reformulated in terms of the reduced scalar potential

$$\nabla \cdot (\mu^+ \nabla \phi_m^+) = \nabla \cdot (\mu^+ \vec{H}_{BS}) \tag{4.15}$$

subject to the continuity conditions

$$\phi_m^+ = \phi_m^- \tag{4.16}$$

$$\mu^+ \frac{\partial \phi_m^+}{\partial n} - \mu^- \frac{\partial \phi_m^-}{\partial n} = (\mu^+ - \mu^-)\hat{n} \cdot \vec{H}_{BS} \tag{4.17}$$

Such non-linear magnetostatic problem can be solved using the nodal Finite Element Method, if the original open domain is properly truncated using some kind of enclosing boundary.

To solve (4.15) it is necessary to know the static permeability $\mu = \mu_{stat}(H) = \frac{B(H)}{H}$ or the initial B-H curve of the ferrite material. Discussion of the ferrite magnetization curves is presented in Section 5.3. What is important here is that since $\mu_{stat}(H)$ is the function of the unknown internal magnetic field, the magnetostatic problem (4.15) has to be solved iteratively. The following update equation was used for this purpose [44]

$$\mu_{new} = a\mu_{old} + b\mu_{stat}(H) \tag{4.18}$$

where μ_{new} and μ_{old} are the permeabilities for the current and previous iterations, respectively, and a and b satisfy the relationship $a + b = 1$.

Chapter 5

MODELING USING ANSYS MAXWELL 3D

Approaches 1 and 2, which were discussed in Chapter 4, require explicit knowledge of the applied magnetic field, which can be measured or determined by solving a linear magnetostatic problem. Using this applied field, the internal field in Approach 1 is found by applying equation 4.4, and the internal field in Approach 2 is found by solving the non-linear magnetostatic problem using the total scalar potential formulation. Approach 3 does not require explicit knowledge of the applied field. The internal field is computed directly by solving the non-linear magnetostatic problem using the reduced scalar potential formulation. Thus, regardless of which approach is used, either linear or non-linear magnetostatic problem has to be solved to obtain the magnetic field inside the ferrite material. In this study, this problem was solved using our own Fortran FEM code as well as the commercial software Ansys Maxwell 3D.

Crucial to the computation of the internal magnetic field is the applied field. It has to be modeled explicitly in Approaches 1 and 2 and implicitly in Approach 3. In the latter approach, it enters the formulation indirectly through modeling of the actual sources of the magnetic field. Depending on the application, the applied magnetic field can be produced by electromagnets or permanent magnets. An electromagnet consists of one or more current coils which are usually wound on a magnetically soft material such as iron. The purpose of iron is to concentrate magnetic flux in a desired direction. The intensity of the magnetic field generated by such a magnet is controlled by the strength of the current in the coils. Permanent magnets are usually chemical composites with permanent magnetization. The advantage of using permanent magnets, instead of the electromagnets, is that they do not require current coils and power sources to generate magnetic field. In addition, permanent

magnets are usually lighter and smaller than electromagnets. On the other hand, very serious and obvious disadvantage of using permanent magnets is their fixed magnetic field. Reconfigurability/tunability of a ferrite-loaded CBS antenna relies on our ability to dynamically vary the intensity of the applied field. While with the electromagnets the variation of the applied magnetic field is achieved electronically by changing the current in the coil, with the permanent magnets it can be achieved mechanically by moving magnets closer or further away from the ferrite material.

5.1 Modeling the Electromagnets.

Photographs of two biasing configurations using two-pole and one-pole electromagnets are shown in Figure 5.1. Their dimensions are given in Figures 5.2 and 5.3 for the two-pole and one pole configurations, respectively. Designation of the electromagnets as one-pole and two-pole is just a convenient way of distinguishing the two different configurations. Obviously, both electromagnets have two poles. In the two-pole configuration, the cavity is placed between the two poles of the electromagnet whereas in the one-pole configuration only one side of the cavity is next to the pole and the other side is free; both are illustrated graphically in Figure 5.2 and 5.3, respectively. The one-pole configuration generates a much more non-uniform applied magnetic field.

A typical Ansys Maxwell 3D model for the magnetostatic problem is shown in Figure 5.4. The entire structure consists of the iron (blue), two coils (orange), two coil terminals (black), ferrite material (magenta), and enclosing boundary (light blue). (when solving for the applied field in Approaches 1 and 2, the ferrite material should be removed.) Cavity walls are not modeled because they are non-ferrous objects and therefore, transparent to the static magnetic field. The size of the enclosing boundary is $(38.0 \times 24.0 \times 31.0)$ cm. In order to solve this problem using Ansys

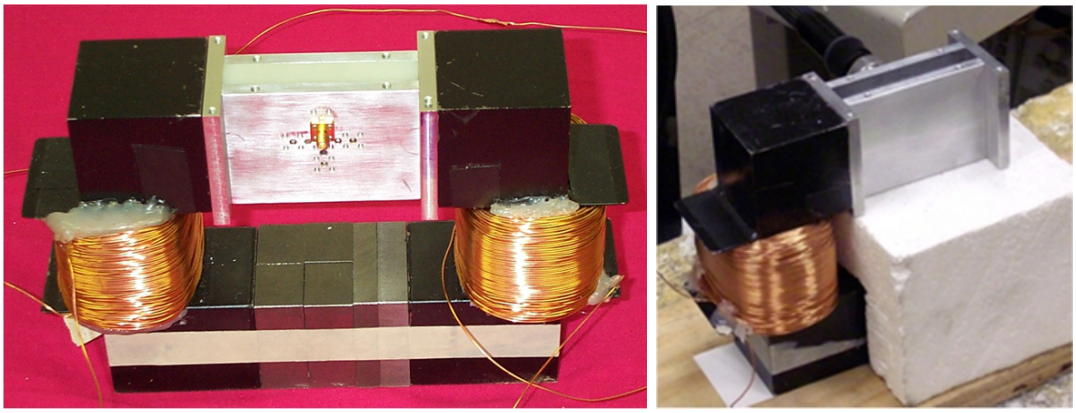

(a) Two-pole electromagnet (b) One-pole electromagnet

Figure 5.1: Biasing configurations using electromagnets.

Maxwell 3D, the following information about the actual physical setup is required:

- Permeability of the ferrite material.
- Permeability of the iron core.
- Current in the coils.
- Number of turns in the coils.

The knowledge of the ferrite permeability is of utmost importance for the computation of the internal magnetic field when Approaches 2 or 3 are used. Ferrites are non-linear materials; therefore, to accurately model them, their magnetization curves are required. Such curves are usually provided by the manufacturer but sometimes they can also be approximated using mathematical models [27, 31, 32, 33]. The issue with the ferrite permeability will be discussed in detail in Section 5.3. Until then, it is assumed that the ferrite material is removed from the cavity. In essence, the main problem that we are concerned with until Section 5.3 is accurate modeling of the applied magnetic field. In order to compute this field, the remaining three items on the list should be addressed.

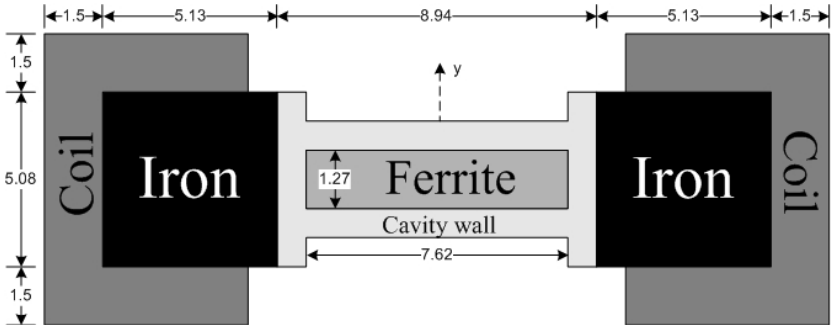

(a) Top view

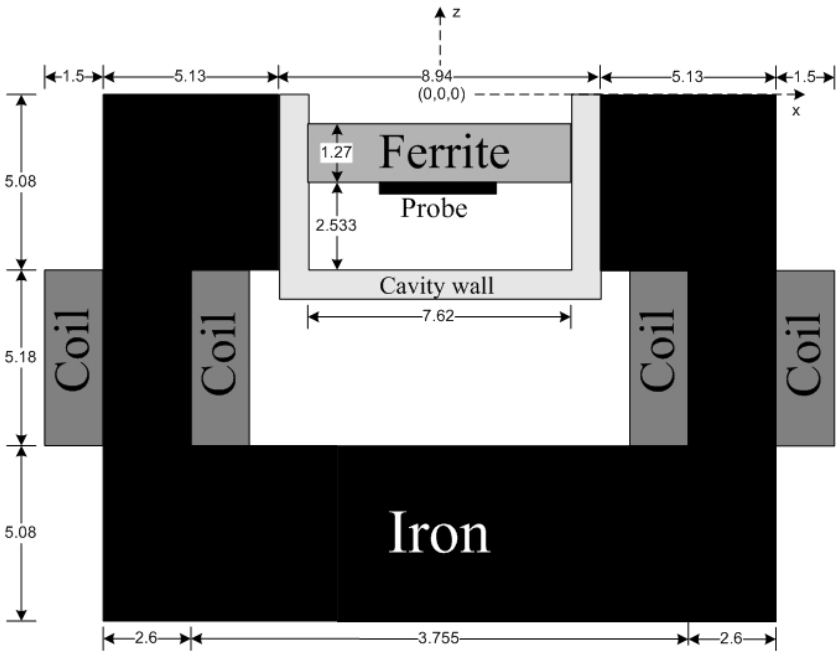

(b) Side view

Figure 5.2: Dimensions of the two-pole electromagnet (units of length: cm).

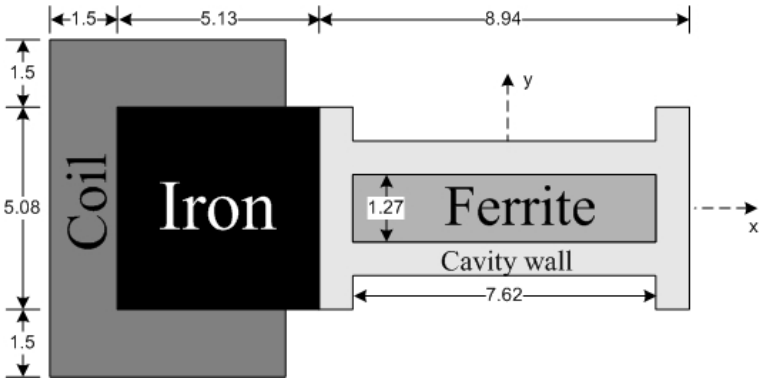

(a) Top view

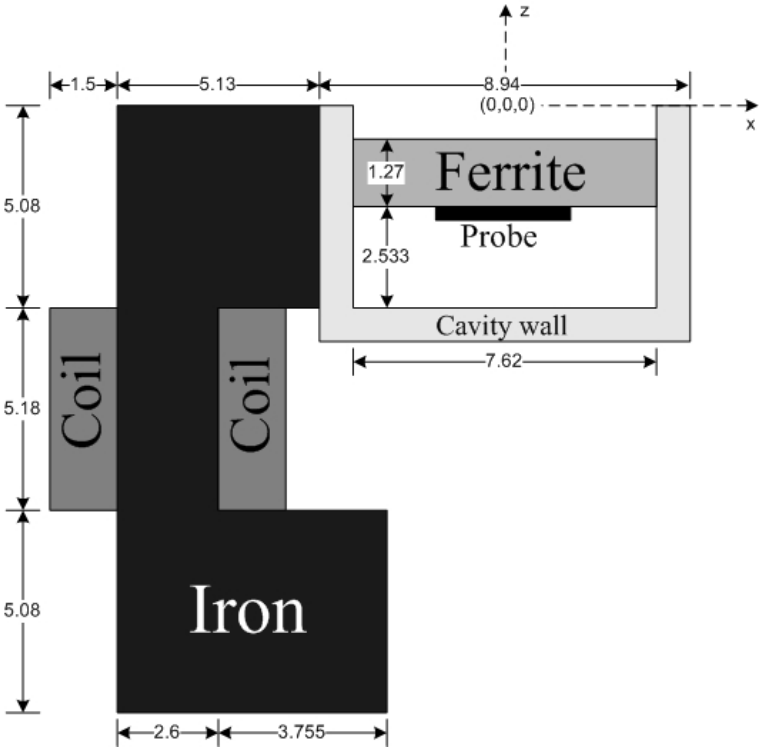

(b) Side view

Figure 5.3: Dimensions of the one-pole electromagnet (units of length: cm).

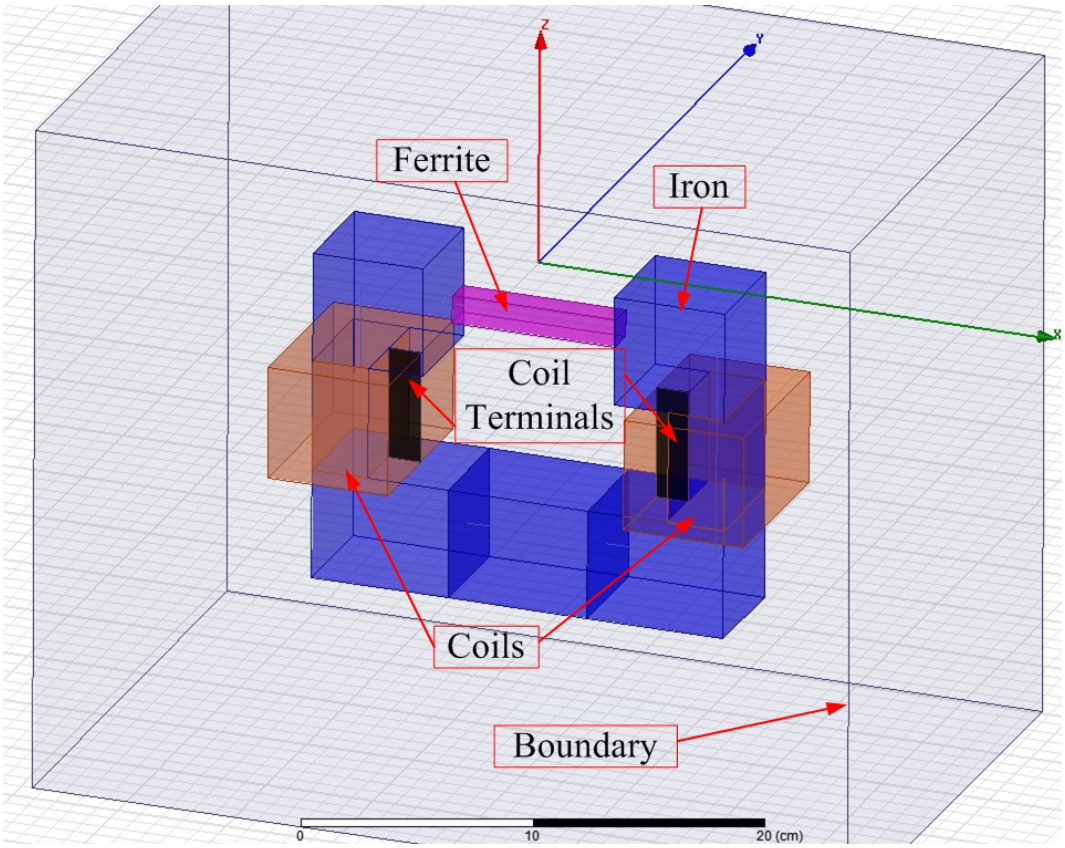

Figure 5.4: Ansys Maxwell 3D model of the two-pole electromagnet and the ferrite material.

Permeability of the Iron Core.

Iron is a ferrous material. This means that, just like in ferrites, its permeability is a non-linear function of the magnetic field and in order to model iron accurately, its B-H curve is required. Unfortunately, such a curve may not be available. To make matters worse, it may not even be known with certainty what material the core of the electromagnet is made of.

Let us say we do not know exactly what material is used for the core of our electromagnet, but we know that it is a soft magnetic material. A number of B-H curves for the magnetically soft materials can be found in [45]. Suppose that we narrowed down our choice to the following three:

- Ingot iron.
- Steel-1008 (cold drawn carbon steel, annealed).
- Steel-1010.

The B-H curves for these materials are shown in Figure 5.5. The curve for the ingot iron is copied from [45] and the other two curves are taken from the Ansys Maxwell 3D material database. So, the question is then: "Which one of these curves describes the core of our electromagnet?" Such a question may be difficult to answer without additional information. However, in our magnetostatic problem we are not interested in the accurate computation of the magnetic field inside the iron. What is important to us is the accurate computation of the magnetic field produced by the electromagnet as a whole. So, a more relevant question to us is: "How critical are these curves to the computation of the applied magnetic field?" In other words, what we want to know is, if using one B-H curve instead of the other, will it result in

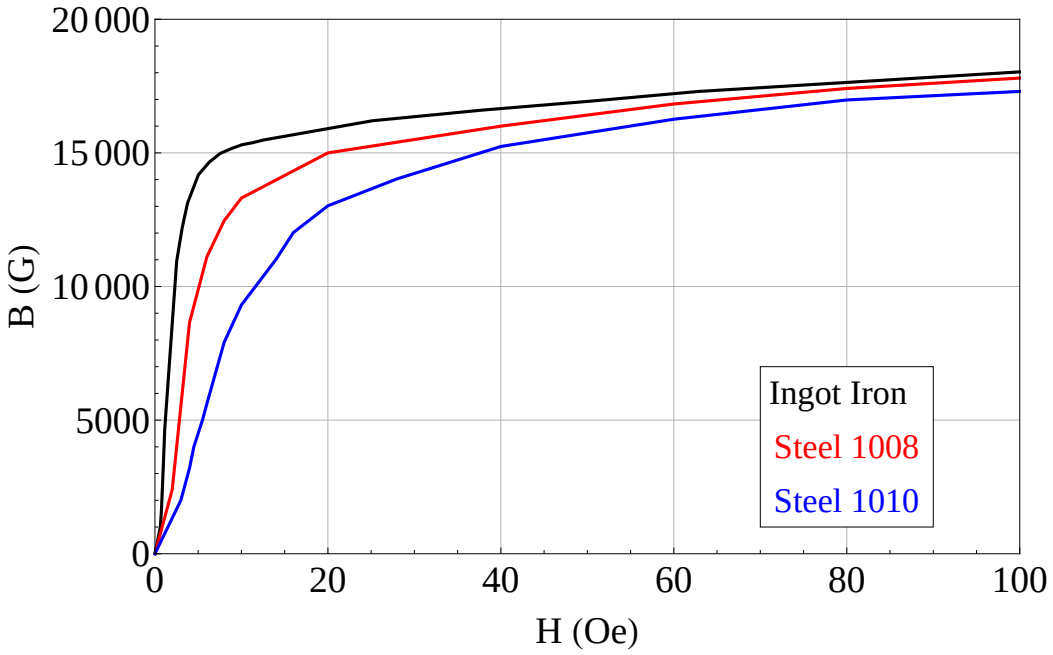

Figure 5.5: B-H curves for three soft magnetic materials.

a significantly different applied magnetic field? To answer this question, all we need to do is simulate the applied magnetic field using each of the B-H curves in Figure 5.5 and compare the results. Such a comparison is shown in Figure 5.6. As can be seen, the three computations are very close to each other; apart from a very small difference, $3 - 6$ Oe, the curves are nearly identical. Thus, either of the B-H curves in Figure 5.5 can be used to model the iron core.

This statement may seem trivial since the curves in Figure 5.5 are not that different. To put things in perspective, Figure 5.7a shows the permeability of iron in each simulation. The multicolored bar on the bottom of the figure identifies different regions in the iron. The distributions are plotted along the line marked *plot line* in Figure 5.7b, where the numbers in brackets identify the distance to the end of each region along the x-axis in Figure 5.7a. Each color of the bar corresponds to the same color on this line; for instance, the green sections on the bar correspond to the green sections on the plot line, etc. As can be seen, unlike the applied magnetic field, the

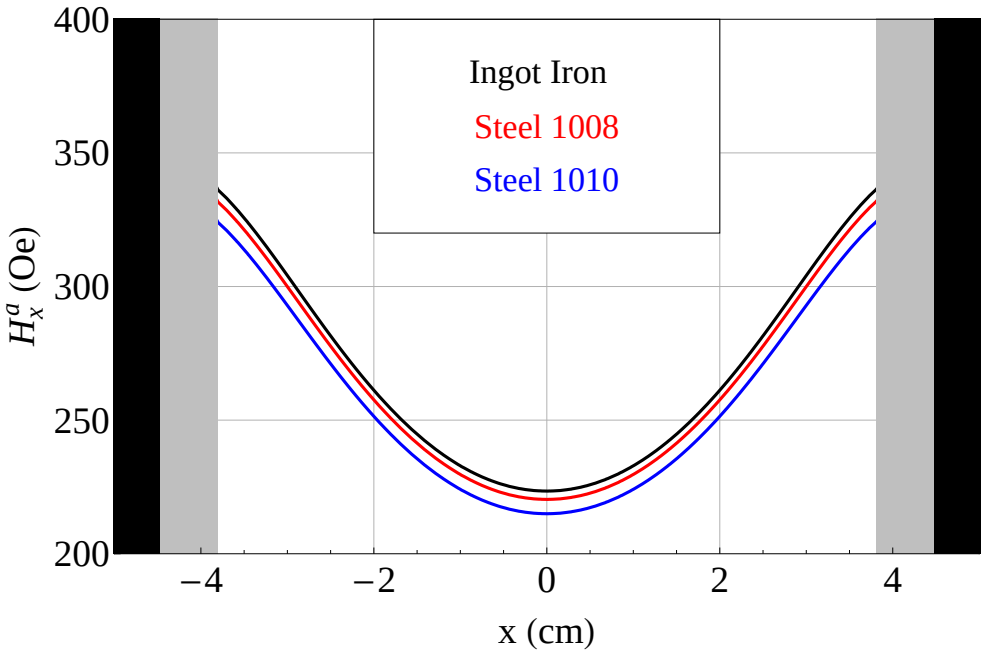

Figure 5.6: Applied magnetic field computed using three different B-H curves to model the iron core of the electromagnet. B-H curves are shown in Figure 5.5.

permeability of the iron depends substantially on the choice of the B-H curve, even for such seemingly similar curves like the ones shown in Figure 5.5.

The analysis above shows that using the 'right' B-H curve is very important for the accurate simulation of the magnetic field inside the iron core. On the other hand, it also indicates that the simulations of the applied magnetic field are quite insensitive to the precise modeling of the field inside the iron. The bulk effect of the iron appears to be more important to the applied field than the precise modeling of the iron. This observation leads to the following idea. If exact modeling of the permeability of iron is not critical for the computation of the applied magnetic field, then modeling iron using its B-H curve is perhaps unnecessary. In other words, instead of modeling the iron as a non-linear material using its B-H curve, it may be sufficient to model it as a linear material using a constant permeability. Figure 5.8 demonstrates this idea. The applied magnetic field was computed for two different

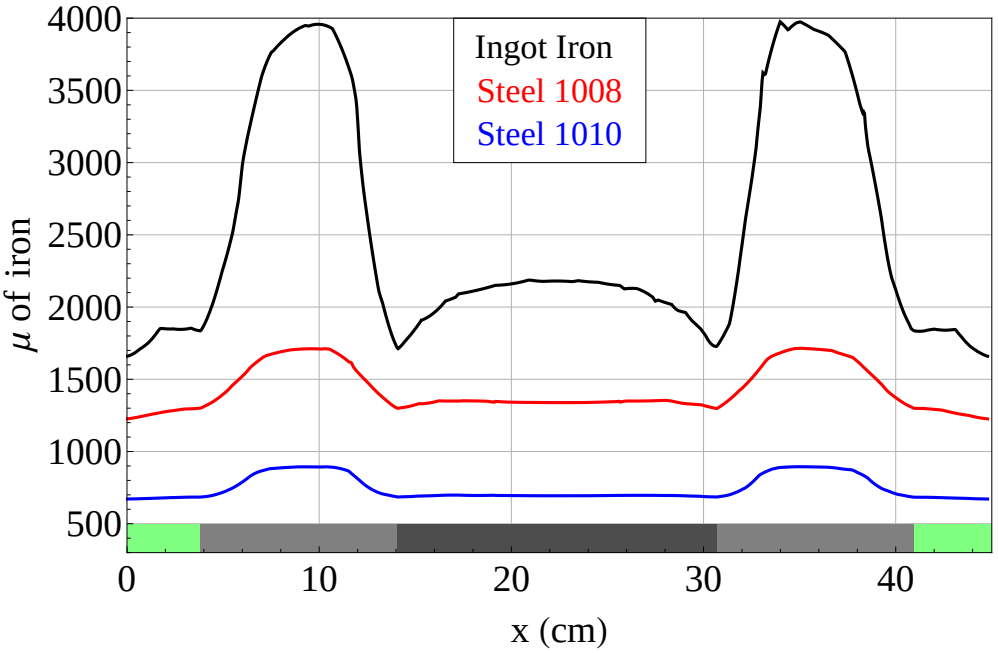

(a) Permeability distribution

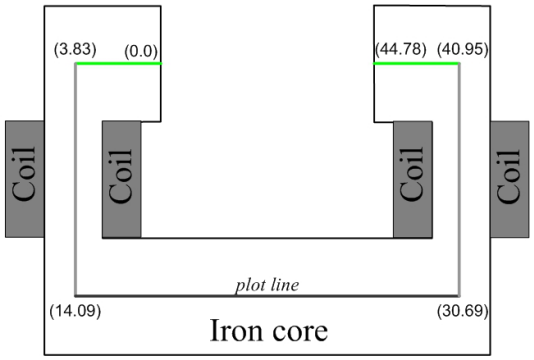

(b) Plot line

Figure 5.7: Permeability distribution in iron for the three B-H curves shown in Figure 5.5.

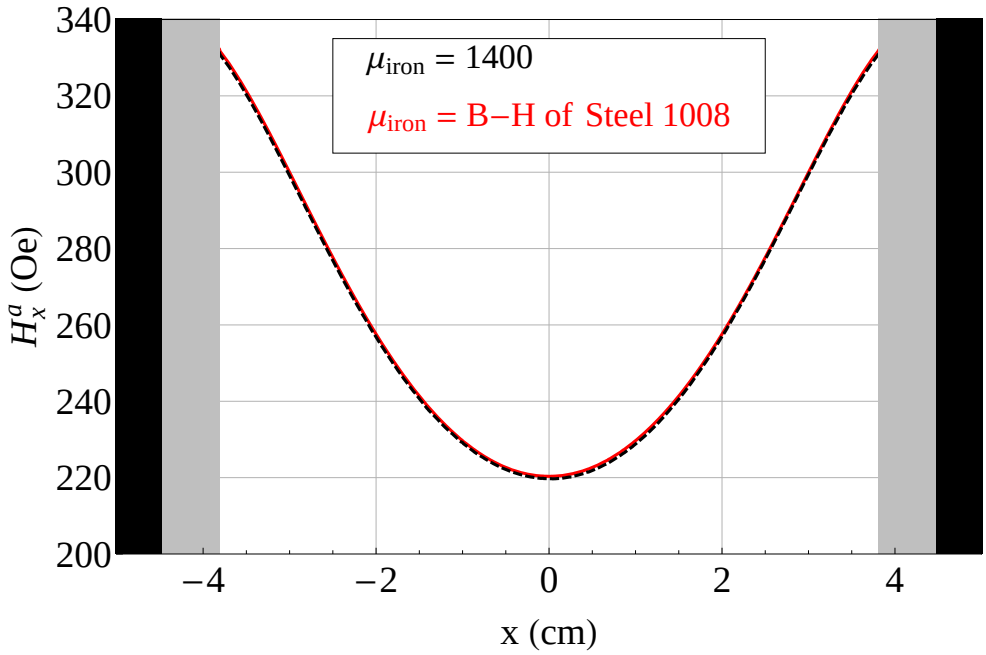

(a) Current excitation 1000 A

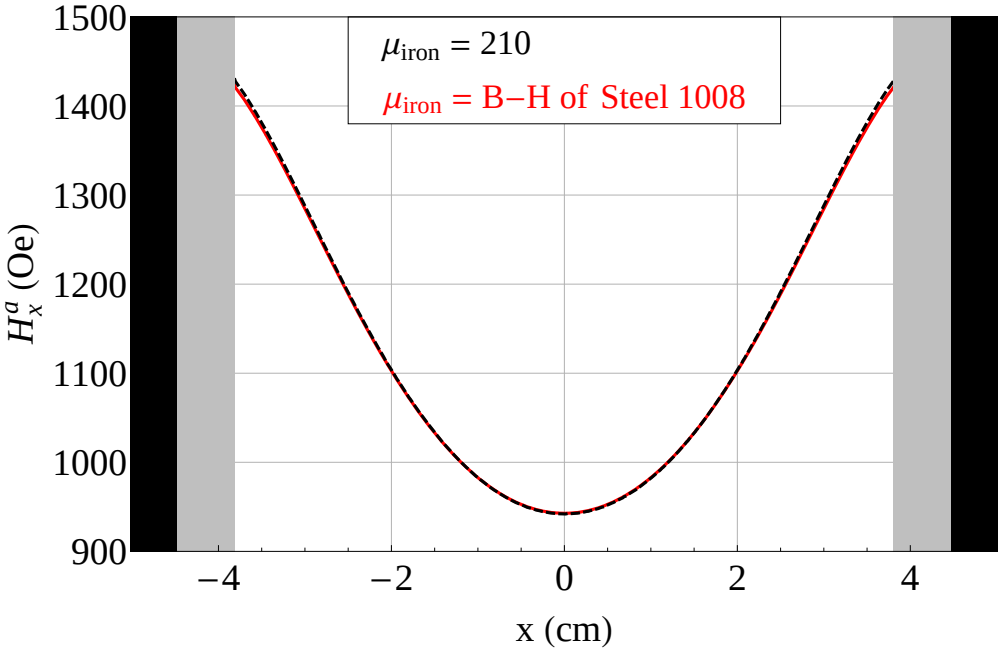

(b) Current excitation 5000 A

Figure 5.8: Applied magnetic field computed using non-linear B-H curve for Steel-1008 (see Figure 5.5) and the constant permeability.

current excitations: 1,000 A, and 5,000 A. The red curves represent the applied magnetic field simulations based on the B-H curve for Steel-1008. The black dashed curves are simulations based on the iron with constant permeability. Clearly, both simulations are in excellent agreement. Thus, it can be concluded that modeling the iron core using its actual B-H curve or approximating it with a constant permeability yields the same applied magnetic field.

This conclusion is important because it means that it may be possible to simplify computations of the applied magnetic field in Approaches 1 and 2 without jeopardizing the accuracy of the results. The simplification is essentially the following. If B-H curve is used, then the magnetostatic problem that needs to be solved to obtain the applied field is a non-linear problem (the iron is modeled as a non-linear material). On the other hand, if constant permeability is used, then the magnetostatic problem is linear. Simply put, solving a liner problem is easier than solving a non-linear problem. This may not be as obvious to the user of a commercial software like Ansys Maxwell 3D, but it can be quite important to someone who is developing their own FEM code. Writing efficient code to solve a non-linear problem may be quite challenging because issues such as convergence, speed, and reliability of the results are much more serious and demanding in the context of solving non-linear problems.

The possibility to simplify the analysis without sacrificing accuracy is very appealing. Then the next obvious question is: "If we decide to replace the B-H curve of iron with a constant permeability, then which constant should be used?" In the literature, the permeability of iron is sometimes listed as a single number which usually represents the maximum permeability [6]. But, it should be remembered that iron is a non-linear material and its permeability is a function of the magnetic field. Therefore, the maximum permeability may not be very representative of the

actual state of the material under study. Figure 5.8 demonstrates this point. As a reminder, the red solid curves are simulations of the applied magnetic field based on the B-H curves and the black dashed ones are simulations based on the constant permeability. Careful examination of the figures shows that as we change the strength of the excitation current, the permeability of the iron also has to change to maintain good agreement between the red and black curves. In Figure 5.8a the excitation current is 1,000 A and the constant permeability of the iron is $\mu_{iron} = 1,400$. When the current is increased to 5,000 A in Figure 5.8b, the permeability of the iron has to be changed to $\mu_{iron} = 210$ to obtain the black curve. This is the consequence of the non-linear nature of iron. Different current excitations imply different magnetization states of iron, and different magnetization states lead to different permeability.

Coil Current and the Number of Turns.

The next two issues on the list are the current in the coil and the number of turns of the coil. The current is usually readily available from the experiment but the number of turns is often not. Together these issues constitute a more general problem, that of specifying the current excitation for the simulation. The difficulty arises because the modeled coil is not the same as the physical coil; the physical coil is a collection of wire windings but the modeled coil is a solid object.

Figure 5.4 shows two coil terminals, they are plane sheets with the same dimensions as the cross-section of the coils. Such terminals are required to specify the current excitation. Figure 5.9 shows the 'Current Excitation' window in Ansys Maxwell 3D v.14. Of interest to us is the number that should be entered in the '*Value*' box. This number represents the total current passing through the cross-sectional area of the coil, $Value = I \times N$, where I is the current in the coil and N is the number of turns. As was mentioned previously, the current I is usually known

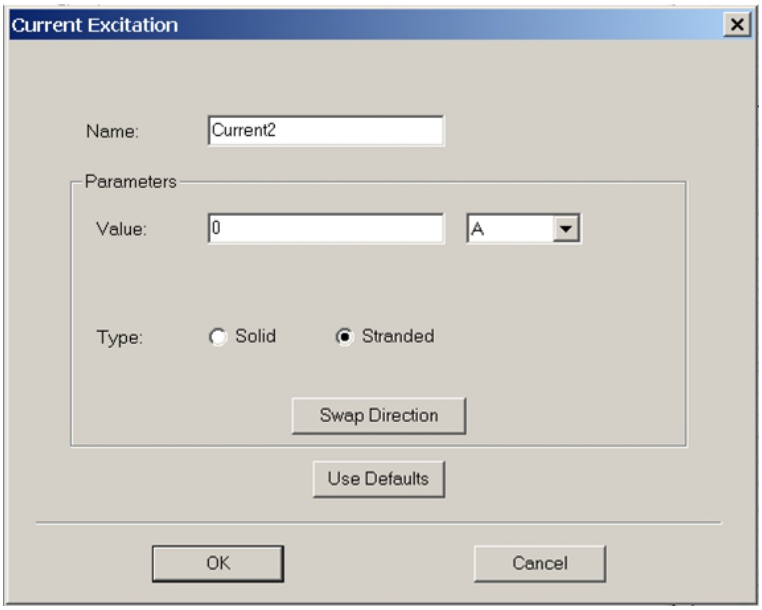

Figure 5.9: Current Excitation window in Ansys Maxwell 3D v.14.0.

but the number of turns is not. In such a case, N can be approximated as $N = \frac{a}{d} \times \frac{b}{d}$, where a and b represent dimensions of the coil terminal and d is the diameter of the coil wire. For example, if the coil current is $I = 4$ amp, the diameter of the wire is 0.077 cm and the dimensions of the coil terminal are (1.50×5.18) cm, then the '*Value*' can be estimated as:

$$Value = I \times N = 4 \times \left(\frac{1.50}{0.077} \times \frac{5.18}{0.077} \right) \simeq 5,242 \tag{5.1}$$

Unfortunately, such a computation is often only an approximation of the actual current due to the following reasons:

- The exact number of turns, N, may not be known.
- The actual dimensions of the coil cross-sectional area may not be known and/or modeled precisely.
- The windings in the coil may not be distributed uniformly.

- When in operation, the coil gets very hot which increases the resistivity of the wires and leads to greater losses in the coil windings, which are difficult to model.

Thus, it is highly possible that the exact number to be entered in the '*Value*' box cannot be determined *a priori*, and it has to be adjusted through simulations. One way to perform such an adjustment is to measure the magnetic field in the empty cavity and then, through trial and error, adjust the '*Value*' until the simulations are in acceptable agreement with measurements.

5.2 Modeling the Permanent Magnets.

Photographs of the biasing configurations using permanent magnets are shown in Figure 5.10. On the left, Figure 5.10a, is the square cavity, $(5.08 \times 5.08 \times 5.08)$ cm, with two permanent magnets attached to the two opposite walls of the cavity. This configuration was used in [10] and [39]. Figure 5.10b shows a similar configuration

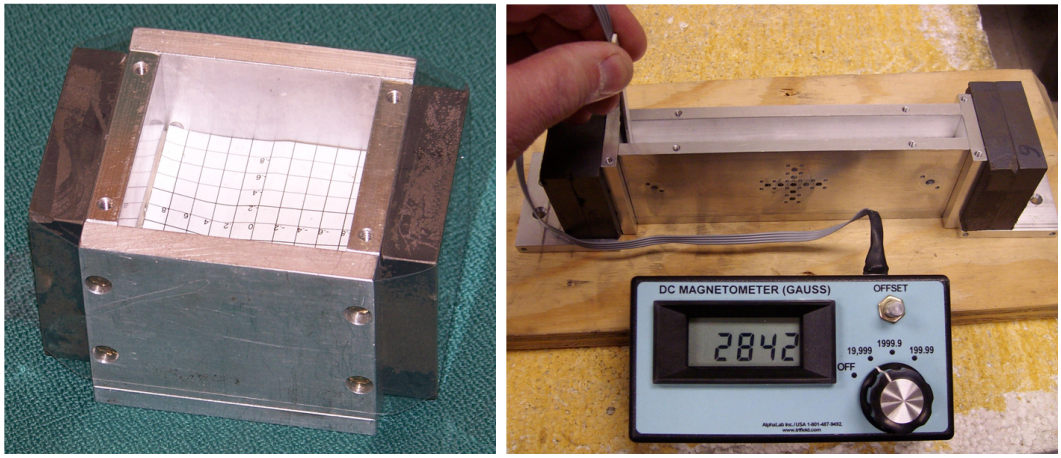

(a) Square cavity with two magnets. (b) Rectangular cavity with four magnets.

Figure 5.10: Biasing configurations using permanent magnets.

but with a long, $(15.24 \times 1.27 \times 5.08)$ cm, cavity and two permanent magnets on each side of the cavity. This figure also demonstrates the measurement of the magnetic field generated by such a biasing configuration. The dimensions of this configuration are shown in Figure 5.11. Examples of the most commonly used commercially available permanent magnets are Neodymium Iron Boron (NdFeB) and Samarium Cobalt (SmCo). To compute the magnetic field produced by such permanent magnets, at least three options are available:

- Computer simulation based on the available magnetic properties of the magnet.
- Computer simulation based on the equivalent representation of the magnet in terms of a shell with uniform surface current density.
- Analytical computation using the Biot-Savart law.

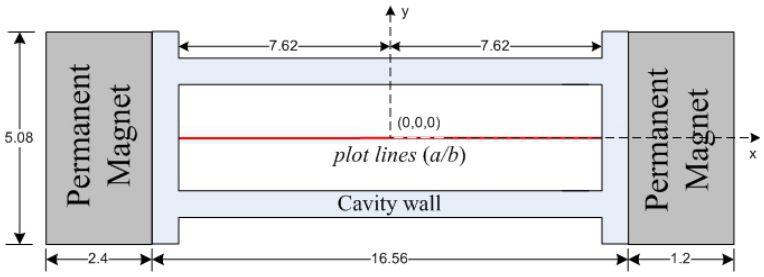

(a) Top view

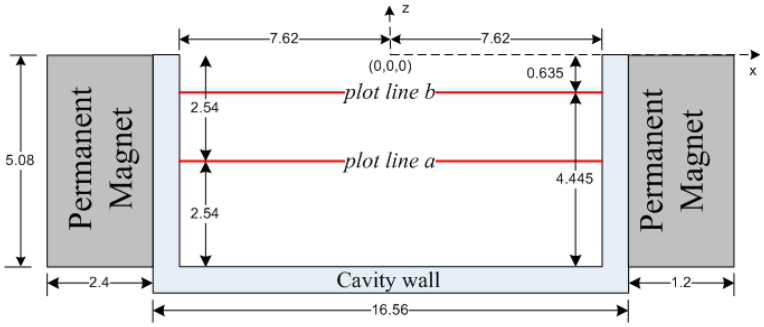

(b) Side view

Figure 5.11: Dimensions of the long cavity and two permanent magnets (units of length: cm).

Modeling Using Magnetic Properties.

Magnetic characteristics of any ferromagnetic material are described by its hysteresis loop, also referred to as the B-H curve. A typical loop is shown in Figure 5.12. The blue curve is known as the *initial magnetization curve* or *initial B-H curve*. It is the curve that the magnetic induction B follows when a completely demagnetized material is subjected to a continuously increasing magnetic field H. The most important part of the hysteresis loop for the description of permanent magnets is the part in the second quadrant represented in red. This part of the loop is known as the *demagnetizing curve*. Two quantities of interest to us on this curve are [26]:

- The residual flux density (or remanent flux density), denoted B_r. This is the value of the magnetic induction when the applied magnetic field is reduced to zero.
- The coercive force (or coercive field intensity), denoted H_c. This is the intensity of the magnetic field necessary to bring the flux density of the magnet to zero.

Good permanent magnets have almost square hysteresis loops; they have high remanent flux density and require large coercive force.

Figure 5.13 illustrates a typical Ansys Maxwell 3D model of the biasing configuration depicted in Figure 5.11. The cavity is not modeled because it is transparent to the static magnetic field. The magnets are represented by two solid bodies. To run the simulation, it is necessary to specify the magnetic properties of these bodies. The most important parameter for our simulations is the magnetic coercivity H_c. When this information is known, modeling does not pose any significant difficulties; one simply needs to specify the parameters and run the simulation.

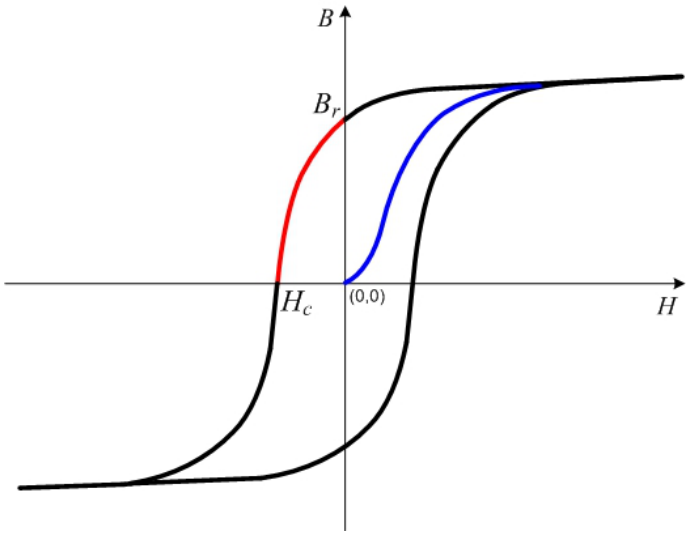

Figure 5.12: General hysteresis loop.

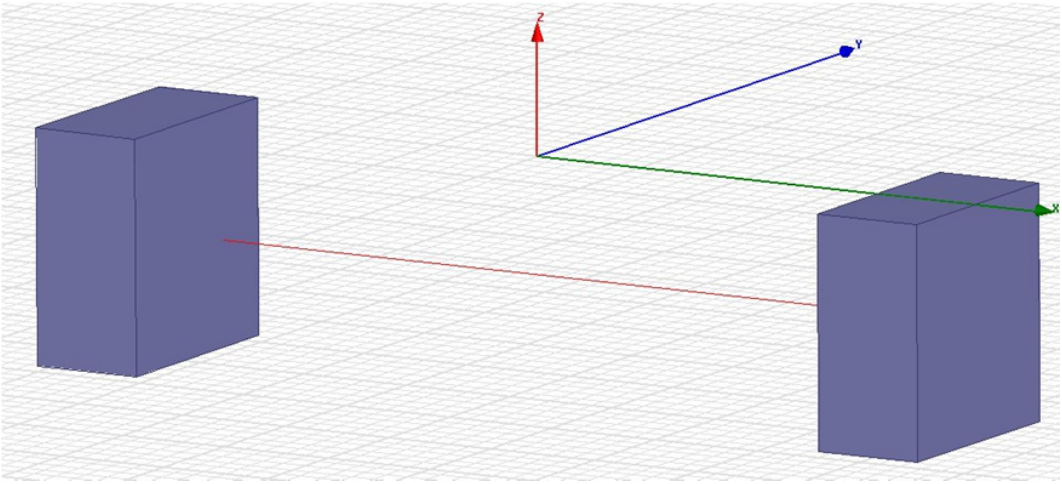

Figure 5.13: Ansys Maxwell 3D model of two permanent magnets.

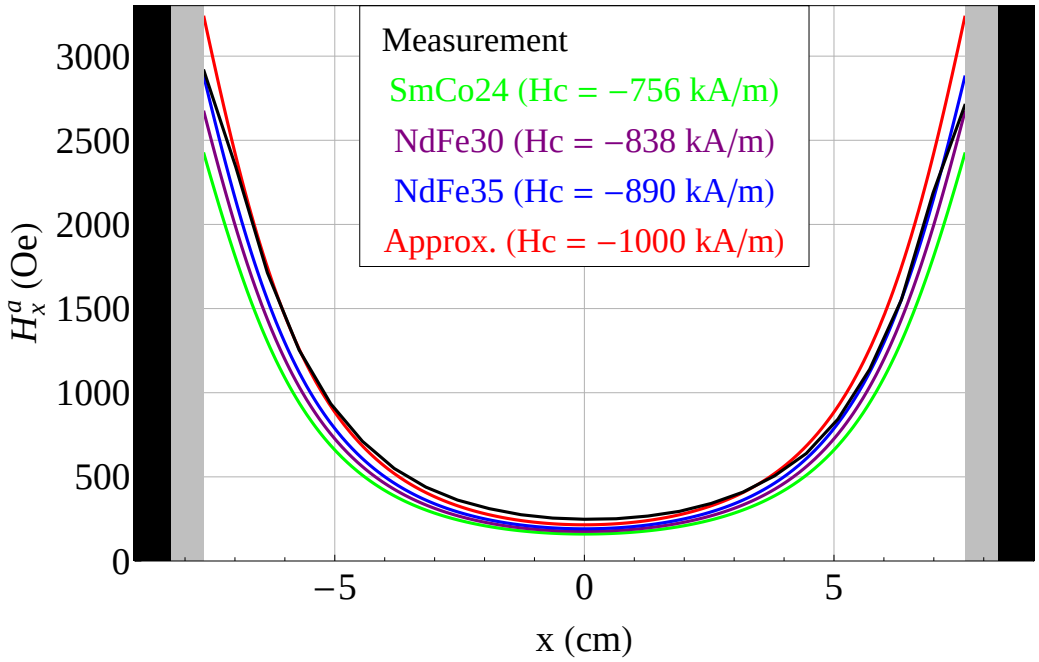

(a) Center (plot line a)

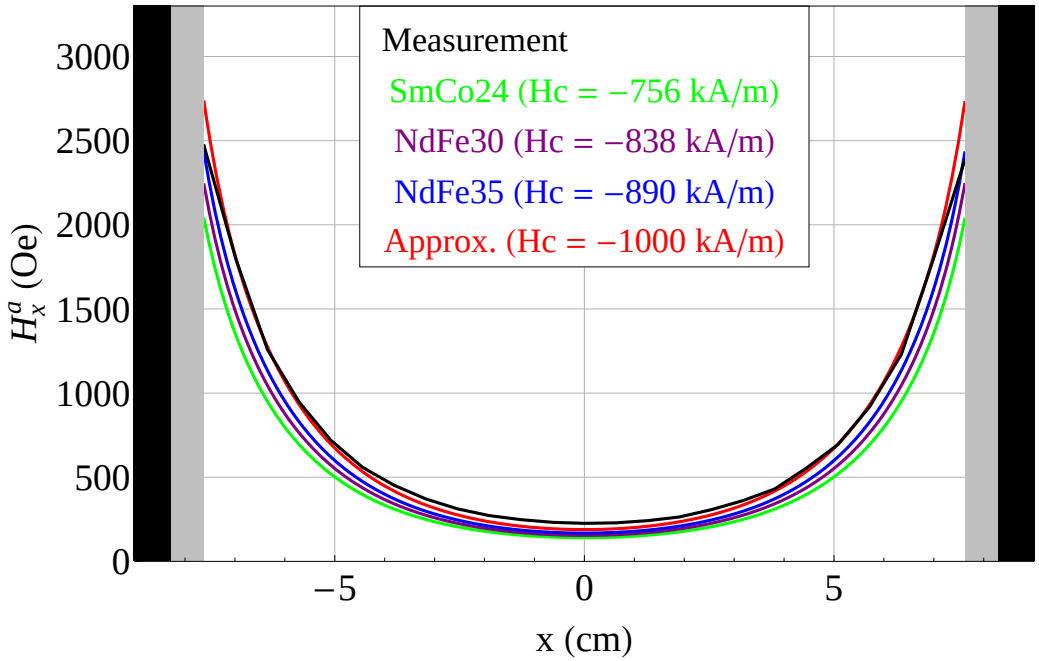

(b) Off center (plot line b)

Figure 5.14: Measured and simulated applied magnetic field. Simulations are based on the permanent magnet models from the Ansys Maxwell 3D materials library.

Unfortunately, magnetic properties of the actual magnet being used in the experiment are not always known. In such a case, we can try using the pre-defined models that come with Ansys Maxwell 3D. In particular, Maxwell 3D v.14.0 comes with a library of materials which includes the following permanent magnets: NdFe30, NdFe35, SmCo24, and SmCo28. The first two are Neodymium and the latter two are Samarium Cobalt magnets (the numbers represent different grading and are not important for our analysis). What we need to do is obtain a set of measurements of the applied magnetic field, simulate this field using these pre-defined models and then compare simulations with measurements.

Figure 5.14 presents such a comparison. The black curves are measurements along the *plot line a* and *b* in Figure 5.11. The green, purple and blue curves represent simulations based on the Ansys Maxwell 3D models for SmCo24, NdFe30, and NdFe35, respectively. The first thing to notice is that all three simulations are very close to the measured distribution. However, simulation based on the NdFe35 is slightly better. The main difference between the considered models is the magnetic coercivity H_c. If we are not satisfied with the accuracy of the pre-defined models, then the parameters of one of them can be adjusted until the simulations are in better agreement with measurements. Such adjustment was performed by changing the magnetic coercivity of NdFe35 to $H_c = -1000$ kA/m. The red curve in Figure 5.14 represents such a simulation. It exhibits a slightly better agreement with the measurements, especially along the *plot line b*, Figure 5.14b.

Modeling Using Equivalent Representation.

If magnetic properties of the permanent magnet are not available, an alternative is to model it as an infinitesimally thin shell with surface current density $\vec{J}$. Such a representation is shown in Figure 5.15, and it depends on the following principles.

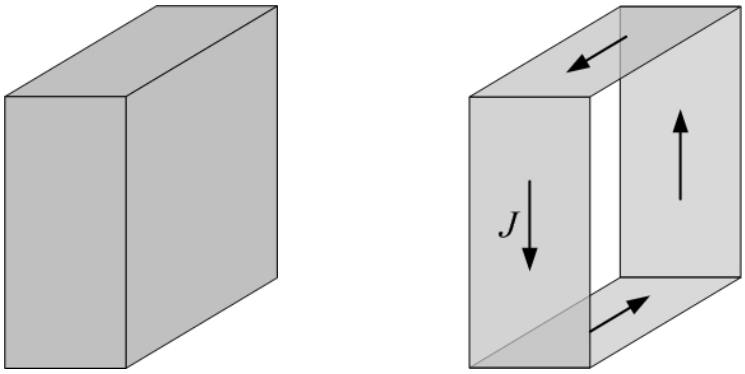

(a) Permanent magnet. (b) Shell of current.

Figure 5.15: Permanent magnet and its equivalent representation as a shell of current.

Mathematically, permanent magnets are described by a magnetization vector $\vec{M}$. The effect of the magnetization vector is equivalent to both a volume current density, $\vec{J}_m$, and a surface current density, $\vec{J}_{ms}$ [26]:

$$\vec{J}_m = \nabla \times \vec{M} \tag{5.2}$$

$$\vec{J}_{ms} = \vec{M} \times \hat{a}_n \tag{5.3}$$

where $\hat{a}_n$ is the unit vector normal to the surface of the magnet. Thus, instead of modeling the magnetic properties of the magnet, we can model its equivalent current densities $\vec{J}_m$ and $\vec{J}_{ms}$. In addition, the magnetization vector $\vec{M}$ of most permanent magnets is nearly uniform. For example, for the magnets in Figure 5.11, it can be written as $\vec{M} = \hat{a}_x M_o$. In such a case, the volume current density, $\vec{J}_m$, vanishes and we only need to determine the surface current density $\vec{J}_{ms}$. This means that the magnetic field produced by a permanent magnet as a solid body is equivalent to the magnetic field produced by a shell of the same dimensions carrying the surface current density $\vec{J}_{ms}$. Obviously, the accuracy of such representation depends on how close the true magnetization $\vec{M}$ is to being uniform.

A typical Ansys Maxwell 3D model for such an equivalent representation is shown in Figure 5.16. The inset shows that in the Maxwell 3D model, the current

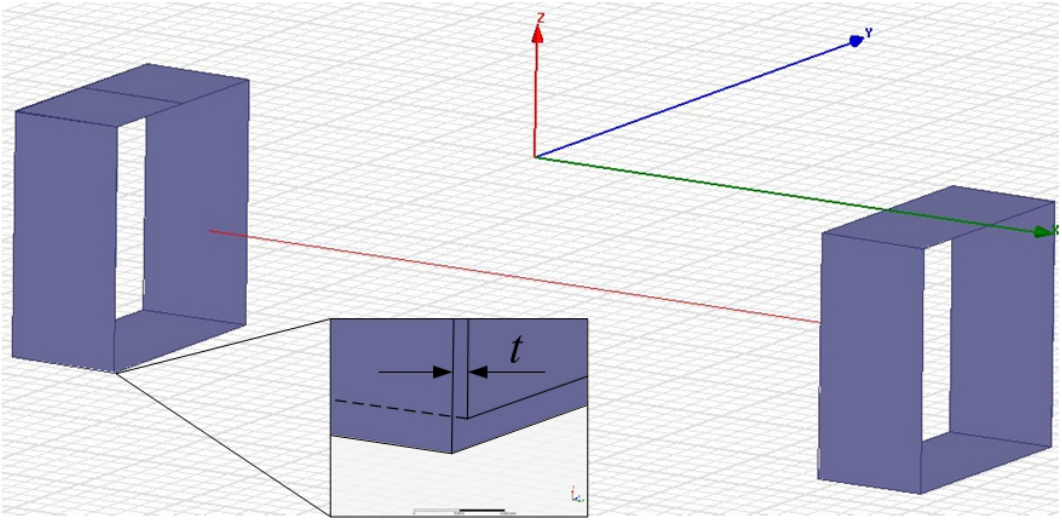

Figure 5.16: Ansys Maxwell 3D model of the permanent magnets using equivalent representation in terms of a shells with surface current density.

shell actually has a finite thickness t as opposed to the theoretical model where the shell has zero thickness. In order to simulate the magnetic field using such a model, it is necessary to specify the current density $\vec{J}$ in the shell. Since no information about the magnets is available, such current density is not known *a priori*. One way to determine it is to follow the same procedure as before; that is, to measure the magnetic field and then adjust the current density in the simulations until a good agreement with measurements is achieved.

Figure 5.17 shows a comparison between the simulated and measured applied magnetic field along the *plot line* a and b in Figure 5.11. As can be seen, the agreement is very good. To achieve such an agreement, the current density had to be set to $Value = 25,000$ A (see Figure 5.9). The effect of the modeled shell thickness is shown in Figure 5.18d. It is obvious that the accuracy of the simulations gets worse as the thickness increases. However, thicker shells may be needed, especially if the magnetization vector of the permanent magnet is not uniform and the volume current density $\vec{J}_m$ does not vanish. But such permanent magnets are not common.

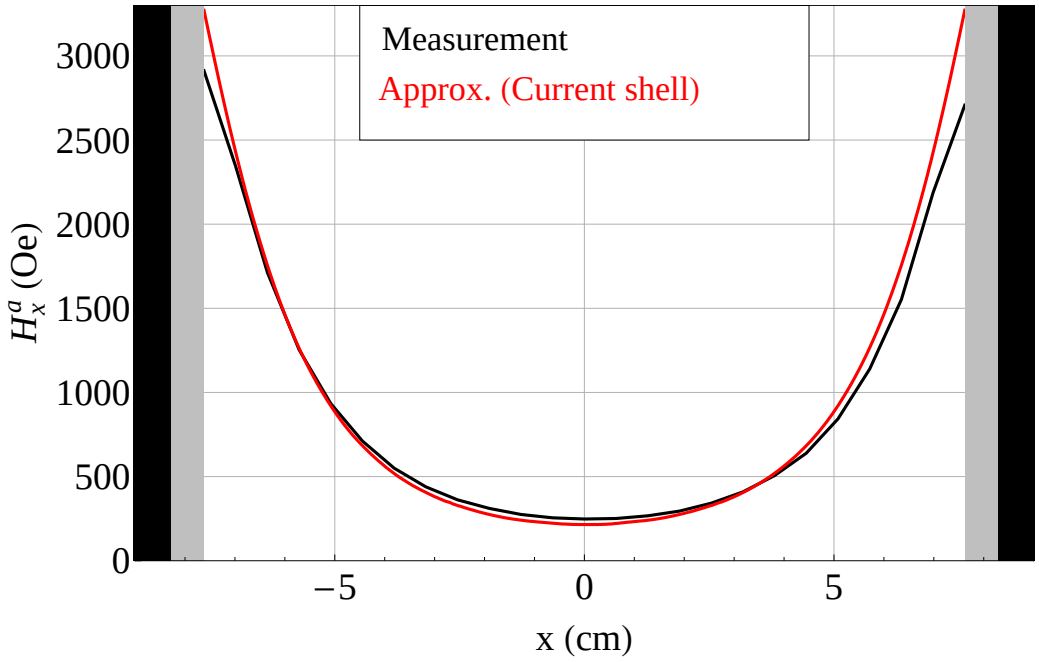

(a) Center (plot line a)

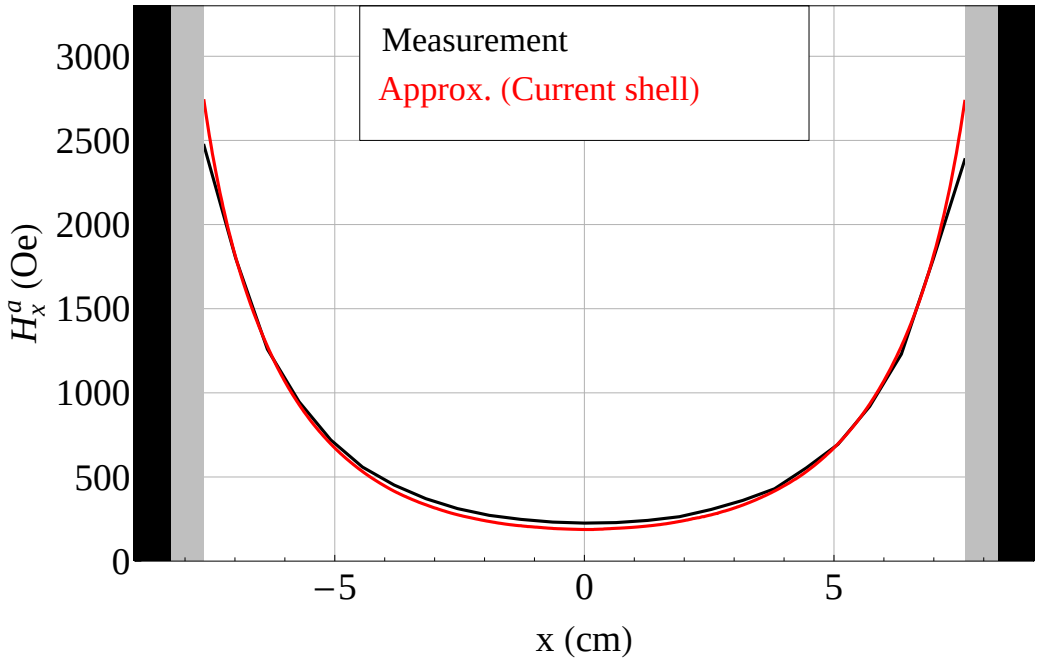

(b) Off center (plot line b)

Figure 5.17: Measured and simulated applied magnetic field. The simulations are based on the equivalent representation of the permanent magnets as shells with surface current density.

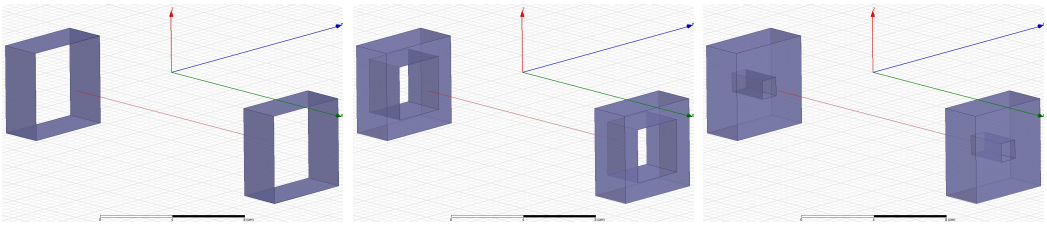

(a) t=0.01 mm (b) t=10.0 mm (c) t=20.0 mm

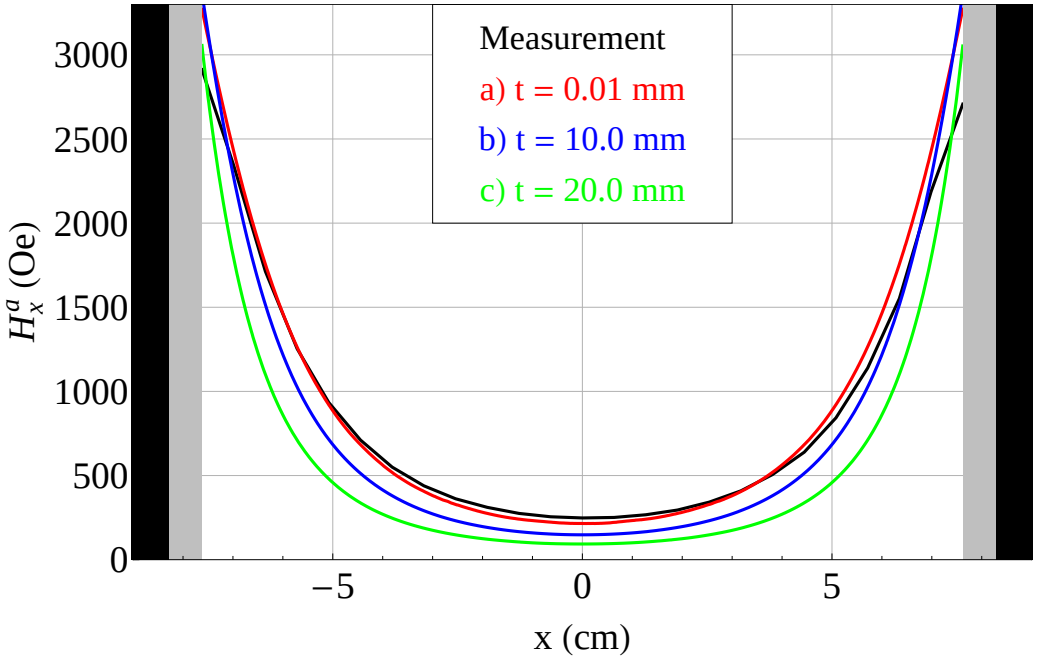

(d)

Figure 5.18: Effect of the modeled shell thickness on the simulated applied magnetic field.

Modeling Using Biot-Savart Law.

Another way to compute the applied magnetic field is to use the Biot-Savart Law [26]. This method is related to the equivalent representation discussed above. After representing the magnet as a shell of current, it is realized that the shell is composed of simpler parts; namely, four rectangular plates: two horizontal and two vertical. Each plate carries a uniform surface current density $\vec{J}$. Thus, if we can compute the magnetic field generated by such a finite plate, then we can combine the contributions from all the plates to find the magnetic field generated by the magnet. The magnetic field $\vec{B}$ generated by a finite plate with uniform current density can be found by evaluating the following integrals:

$$\vec{B}^{hor}_{plate}(x,y,z) = \frac{\mu_0}{4\pi}\int_{x_a}^{x_b}\int_{y_a}^{y_b}\frac{\vec{J}\times\hat{a}_R}{R^2}dx_0dy_0 \tag{5.4}$$

$$\vec{B}^{ver}_{plate}(x,y,z) = \frac{\mu_0}{4\pi}\int_{x_a}^{x_b}\int_{z_a}^{z_b}\frac{\vec{J}\times\hat{a}_R}{R^2}dx_0dz_0 \tag{5.5}$$

where the first integral is for the horizontal plate shown in Figure 5.19a with $\vec{J} = \hat{a}_y I_0$, and the second integral is for the vertical plate shown in Figure 5.19b with $\vec{J} = \hat{a}_z I_0$. In addition, $R = \sqrt{(x-x_0)^2+(y-y_0)^2+(z-z_0)^2}$ and $\hat{a}_R$ is the unit vector directed from the source point (x_0, y_0, z_0) to the field point (x, y, z). These integrals can be evaluated analytically and they are given by (5.6) for the horizontal plate in Figure 5.19a, and by (5.7) for the vertical plate in Figure 5.19b.

Thus, the magnetic field $\vec{B}$ produced by the left and right permanent magnets in Figure 5.11 is given by (5.8) and (5.9), respectively, where each plate is represented by four terms, and x_0, y_0, and z_0 were set to the corresponding x_a, x_b, y_a, y_b, z_a, z_b. The total applied field is the sum of the two, (5.10). Figure 5.20 shows that such analytically computed applied magnetic field is in excellent agreement with measurements. In order to use (5.6) and (5.7), the quantity $(\frac{\mu_0 I}{4\pi})$ has to be specified.

As before, the current I is unknown; therefore, this quantity is fixed through trial and error by comparing computations and measurements. To obtain the red curves in Figure 5.20, it was set to $\frac{\mu_0 I}{4\pi} = 950$.

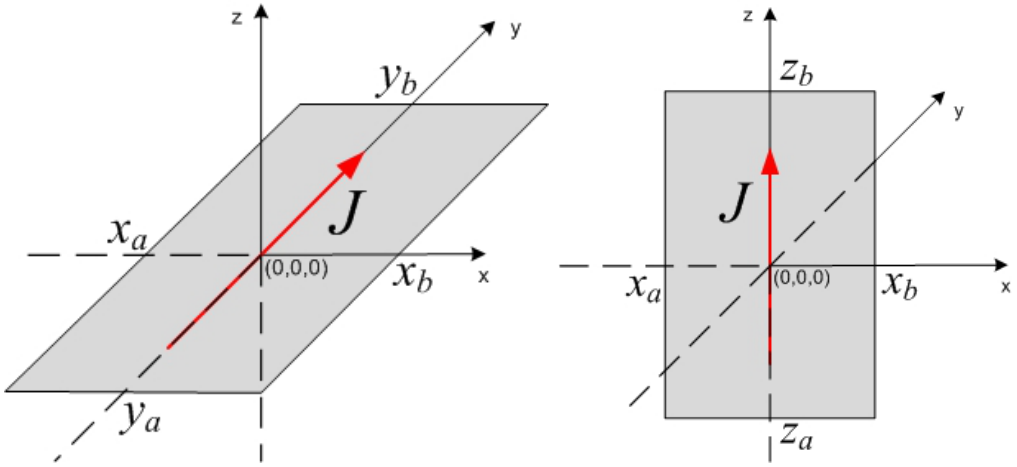

(a) Horizontal, xy-plane (b) Vertical, xz-plane

Figure 5.19: Finite plates with uniform current density J.

$$\begin{aligned}
\vec{B}^{hor}_{plate}(x,y,z,x_0,y_0,z_0) = \quad & \hat{a}_x \frac{\mu_0 I}{4\pi} \tan^{-1}\left[\frac{(x-x_0)(y-y_0)}{(z-z_0)\sqrt{(x-x_0)^2+(y-y_0)^2+(z-z_0)^2}}\right] \\
+ \quad & \hat{a}_y 0 \\
+ \quad & \hat{a}_z \frac{\mu_0 I}{4\pi} \frac{1}{2} \ln\left[\frac{\sqrt{(x-x_0)^2+(y-y_0)^2+(z-z_0)^2}+(y-y_0)}{\sqrt{(x-x_0)^2+(y-y_0)^2+(z-z_0)^2}-(y-y_0)}\right]
\end{aligned} \tag{5.6}$$

$$\begin{aligned}
\vec{B}^{ver}_{plate}(x,y,z,x_0,y_0,z_0) = \quad & \hat{a}_x \frac{\mu_0 I}{4\pi} \tan^{-1}\left[\frac{(x-x_0)(z-z_0)}{(y-y_0)\sqrt{(x-x_0)^2+(y-y_0)^2+(z-z_0)^2}}\right] \\
+ \quad & \hat{a}_y \frac{\mu_0 I}{4\pi} \frac{1}{2} \ln\left[\frac{\sqrt{(x-x_0)^2+(y-y_0)^2+(z-z_0)^2}+(z-z_0)}{\sqrt{(x-x_0)^2+(y-y_0)^2+(z-z_0)^2}-(z-z_0)}\right] \\
+ \quad & \hat{a}_z 0
\end{aligned} \tag{5.7}$$

$$
\begin{aligned}
&\vec{B}_{\text{left magnet}}(x,y,z) = \\
&-\vec{B}^{hor}_{plate}(x,y,z,-10.68,-2.54,0) && +\vec{B}^{hor}_{plate}(x,y,z,-8.28,-2.54,0) \\
&+\vec{B}^{hor}_{plate}(x,y,z,-10.68,2.54,0) && -\vec{B}^{hor}_{plate}(x,y,z,-8.28,2.54,0) \\
&+\vec{B}^{hor}_{plate}(x,y,z,-10.68,-2.54,-5.08) && -\vec{B}^{hor}_{plate}(x,y,z,-8.28,-2.54,-5.08) \\
&-\vec{B}^{hor}_{plate}(x,y,z,-10.68,2.54,-5.08) && +\vec{B}^{hor}_{plate}(x,y,z,-8.28,2.54,-5.08) \\
&-\vec{B}^{ver}_{plate}(x,y,z,-10.68,-2.54,0) && +\vec{B}^{ver}_{plate}(x,y,z,-8.28,-2.54,0) \\
&+\vec{B}^{ver}_{plate}(x,y,z,-10.68,-2.54,-5.08) && -\vec{B}^{ver}_{plate}(x,y,z,-8.28,-2.54,-5.08) \\
&+\vec{B}^{ver}_{plate}(x,y,z,-10.68,2.54,0) && -\vec{B}^{ver}_{plate}(x,y,z,-8.28,2.54,0) \\
&-\vec{B}^{ver}_{plate}(x,y,z,xb,-10.68,-5.08) && +\vec{B}^{ver}_{plate}(x,y,z,-8.28,2.54,-5.08)
\end{aligned} \tag{5.8}
$$

$$
\begin{aligned}
&\vec{B}_{\text{right magnet}}(x,y,z) = \\
&-\vec{B}^{hor}_{plate}(x,y,z,8.28,-2.54,0) && +\vec{B}^{hor}_{plate}(x,y,z,10.68,-2.54,0) \\
&+\vec{B}^{hor}_{plate}(x,y,z,8.28,2.54,0) && -\vec{B}^{hor}_{plate}(x,y,z,10.68,2.54,0) \\
&+\vec{B}^{hor}_{plate}(x,y,z,8.28,-2.54,-5.08) && -\vec{B}^{hor}_{plate}(x,y,z,10.68,-2.54,-5.08) \\
&-\vec{B}^{hor}_{plate}(x,y,z,8.28,2.54,-5.08) && +\vec{B}^{hor}_{plate}(x,y,z,10.68,2.54,-5.08) \\
&-\vec{B}^{ver}_{plate}(x,y,z,8.28,-2.54,0) && +\vec{B}^{ver}_{plate}(x,y,z,10.68,-2.54,0) \\
&+\vec{B}^{ver}_{plate}(x,y,z,8.28,-2.54,-5.08) && -\vec{B}^{ver}_{plate}(x,y,z,10.68,-2.54,-5.08) \\
&+\vec{B}^{ver}_{plate}(x,y,z,8.28,2.54,0) && -\vec{B}^{ver}_{plate}(x,y,z,10.68,2.54,0) \\
&-\vec{B}^{ver}_{plate}(x,y,z,xb,8.28,-5.08) && +\vec{B}^{ver}_{plate}(x,y,z,10.68,2.54,-5.08)
\end{aligned} \tag{5.9}
$$

$$
\vec{B}_{\text{total}}(x,y,z) = \vec{B}_{\text{left magnet}}(x,y,z) + \vec{B}_{\text{right magnet}}(x,y,z) \tag{5.10}
$$

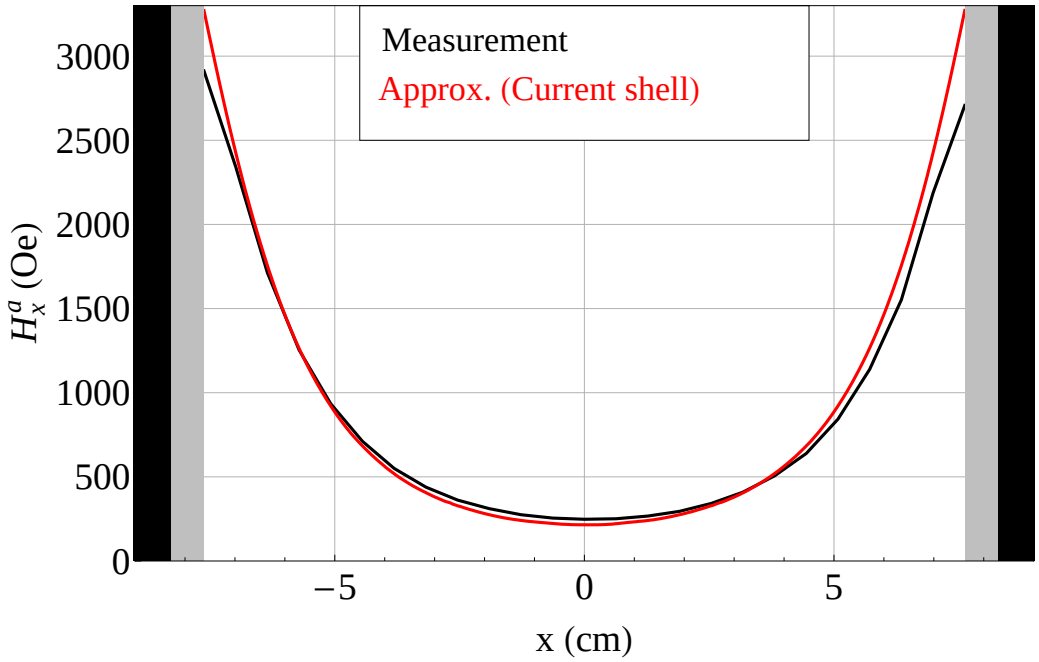

(a) Center (plot line a)

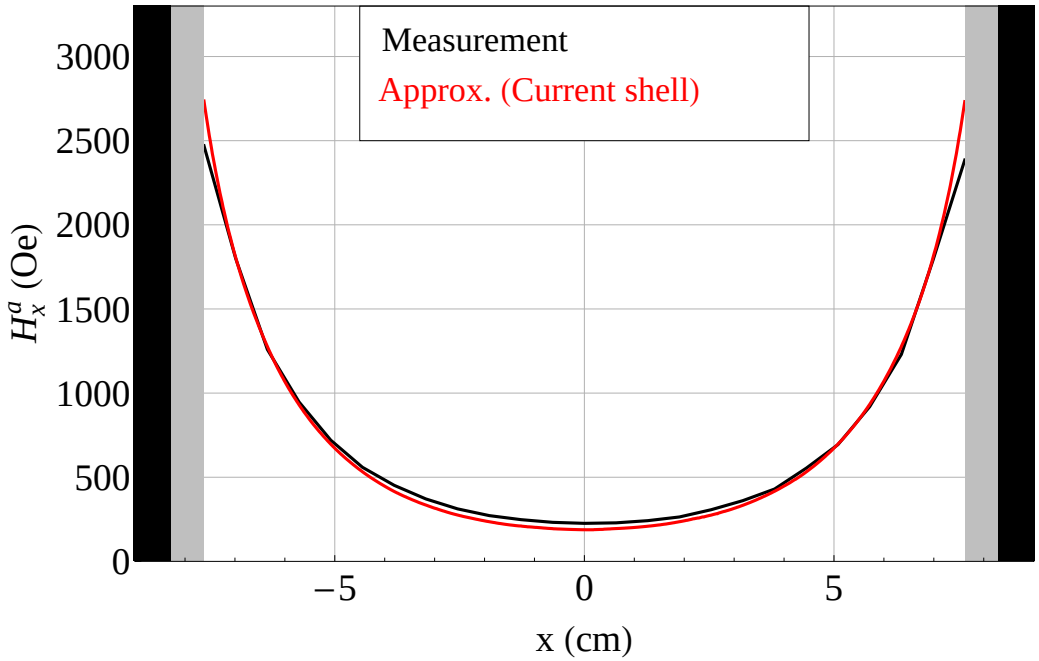

(b) Off center (plot line b)

Figure 5.20: Measured and analytically computed applied magnetic fields. The analytical computation is based on the Biot-Savart Law.

5.3 Permeability of the Ferrite Materials.

The following four ferrite materials were used in this study at one point or another:

- TTVG-800 (Calcium-vanadium doped)
- G-475 (Aluminum doped)
- G-1006 (Gadolinium-aluminum doped)
- TT2-113 (Nickel ferrite)

The first three are garnets and the last one is ferrite (see Chapter 3); we will refer to all of them as ferrites. These ferrites are manufactured by Trans-Tech. Some of their nominal catalog parameters relevant to our magnetostatic as well as the RF analysis are listed in Table 5.1 [21].

Table 5.1: Parameters of the Trans-Tech Ferrite Materials.

Name	$4\pi M_s$ (G)	Landé g-factor	ΔH (Oe)	ε'	B_r (G)	H_c (Oe)	μ_0
TTVG-800	$800 \pm 5\%$	2.00	≤ 15	13.9 $\pm 5\%$	560	0.60	129
G-475	475 ± 25 G	2.01	≤ 45	14.1 $\pm 5\%$	310	0.60	40
G-1006	400 ± 25 G	2.01	≤ 78	14.2 $\pm 5\%$	185	1.00	23
TT2-113	$500 \pm 10\%$	1.54	≤ 190	9.0 $\pm 10\%$	140	2.00	23

In addition to the parameters in Table 5.1, magnetic properties of the ferrite materials are also described by the hysteresis loops, like the one shown in Figure 5.12, Section 5.2. For our magnetostatic analysis, the most important part of the loop is the initial magnetization curve (also called the initial B-H curve) shown in blue in Figure 5.12. Usually, hysteresis loops and, sometimes, initial B-H curves are provided by the manufacturer. But, in the case when no such information is given,

numerous mathematical models/approximations of various complexity and accuracy are available in the literature [27, 31, 32, 33]. For example, the data-sheets for our ferrite materials include hysteresis loops but not the initial magnetization curves. To approximate these curves, we consider the following three mathematical models:

- The first one is described by the following expression [46]:

$$B(H) = H + H\frac{4\pi M_s}{\sqrt{H_1^2 + H^2}} \tag{5.11}$$

  where parameter H_1 is described in [46] as the 'corner' magnetic field where the magnetization reaches 0.707 of its saturation value. Since such a value is usually not known unless the magnetization curve is already available, H_1 is treated as an adjustable parameter in this study. This model was also used in [14] (see Section 4.2).

- The next model is based on the second-order rational fraction of the form [47]:

$$B(H) = H + \frac{a_0 + a_1 H + a_2 H^2}{1 + b_1 H + b_2 H^2} \tag{5.12}$$

  where a_i and b_i are constant coefficients. In [47], the authors express these coefficients in terms of the material susceptibility, saturation magnetization, Rayleigh material constant, and the Néel constant. The latter two are not included in the ferrite material data-sheets available to us. Therefore, to avoid using these constants, it was decided to retain the following definitions for the a_i coefficients:

$$a_0 = 0 \tag{5.13}$$

$$a_1 = \chi = (\mu_0 - 1) \tag{5.14}$$

$$a_2 = b_2 4\pi M_s \tag{5.15}$$

  and treat b_1 and b_2 as adjustable parameters.

- The third model is suggested in this study and makes use of the following asymptotic expressions [28]:

$$B(H \approx 0) = H\mu_o + aH^2 \tag{5.16}$$

$$B(H \gg 0) = H + H\frac{4\pi M_s}{\frac{4\pi M_s}{c} + H} \tag{5.17}$$

where (5.16) is known as the Rayleigh Law for low-field behavior and (5.17) is the Frolich-Kennely expression for the anhysteretic magnetization, also known as the approach to saturation magnetization behavior. These two terms are combined to form the following expression:

$$B(H) = H + (H(\mu_o - 1) + aH^2)e^{-bH} + H\frac{4\pi M_s}{\frac{4\pi M_s}{c} + H}(1 - e^{-dH})^2 \tag{5.18}$$

where a, b, c, d are adjustable parameters. The role of the exponential terms is to diminish the effect of the corresponding term in the equation; they are introduced to control the transition from the low-field behavior to the approach to saturation behavior. For example, for weak fields, $[(1 - e^{-dH})^2 \simeq 0]$ and $[e^{-bH} \simeq 1]$; thus, (5.18) is heavily dependent on the first two terms and exhibits the Rayleigh behavior (5.16). For strong fields, the roles are reversed; the dominant terms are the first and the third, and (5.18) behaves as the approach to saturation (5.17). The aggressiveness of the exponential terms is controlled by the parameters b and d.

In (5.11), (5.12), and (5.18), $H = |\vec{H}^i|$ is the magnitude of the internal magnetic field, $4\pi M_s$ is the saturation magnetization, and μ_o is the initial permeability given in Table 5.1. These models can be categorized as having one, two and four adjustable parameters, respectively. Our goal is to find such a set of these parameters which ensures good approximation of the initial magnetization curve. At this point, it is necessary to define criteria for such a 'good approximation'. Pictorially, it is

represented by the blue curve in Figure 5.12. In words, the following features are desirable:

1. At strong fields, the magnetization curve, ($M = B - H$), should approach saturation magnetization $4\pi M_s$.

2. At low fields, the initial B-H curve should exhibit behavior of a quadratic function.

3. The initial B-H curve should be contained within the hysteresis loop as much as possible.

Parameters which provide reasonably good approximation based on these criteria are listed in Tables 5.2, 5.3, 5.4 for the models (5.11), (5.12), and (5.18), respectively. These parameters were obtained through their methodical adjustment until a satisfactory curve was achieved.

Table 5.2: Parameters for Equation 5.11

Parameter	TTVG-800	G-475	G-1006	TT2-113
$4\pi Ms$ (G)	800	475	400	500
H_1	0.83	2.6	5.3	20.0

Table 5.3: Parameters for Equation 5.12

Parameter	TTVG-800	G-475	G-1006	TT2-113
μ_o	129	40	23	23
$4\pi M_s$ (G)	800	475	400	500
a_0	0	0	0	0
$a_1 = \mu_o - 1$	128	39	22	22
$a_2 = b_2 4\pi M_s$	392000	437000	280000	200000
b_1	150	720	2000	3200
b_2	490	920	700	400

Table 5.4: Parameters for Equation 5.18

Parameter	TTVG-800	G-475	G-1006	TT2-113
μ_o	129	40	23	23
$4\pi M_s$ (G)	800	475	400	500
a	50	475	150	7
b	1.6	1.7	1.0	0.23
c	2000	300	85	40
d	5.5	5.5	5.5	5.5

Figures 5.21a - 5.24a show the hysteresis loops (black) provided by Trans-Tech for the ferrite materials in Table 5.1, and three approximations of the initial B-H curves. Figures 5.21b - 5.24b show the approach to saturation of the magnetization curves, and Figures 5.21c - 5.24c show the corresponding non-linear permeability curves.

These figures clearly demonstrate the ability of the discussed models to satisfy stated criteria. Magnetization curves, $M = B - H$, for example, show that all three models easily satisfy the first criterion. For strong fields, the models are on a par with each other; they obviously converge to the saturation magnetization and they do it in a very similar fashion. That models are nearly identical at high fields can also be inferred from the convergence of the permeability curves.

The deficiency of the first two models becomes evident at low fields. Clearly, the simples model (5.11) is unable to properly approximate the desired low field behavior, with the exception of the TTVG-800 ferrite in Figure fig:TTVG-800. Being dependent only on one adjustable parameter, this model simply does not provide enough flexibility to keep the curves contained within the hysteresis loops, as desired by the third criterion. In addition, mathematically, the quadratic behavior for H field near zero is not included in (5.11), which is also evident in the figures. The second model (5.12) is more accurate; acceptable approximations are seen in Figures 5.21

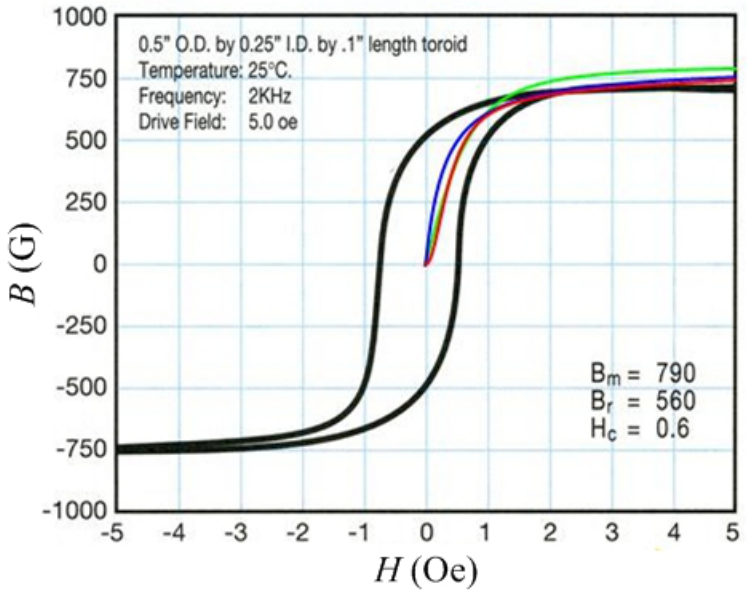

(a) Hysteresis loop

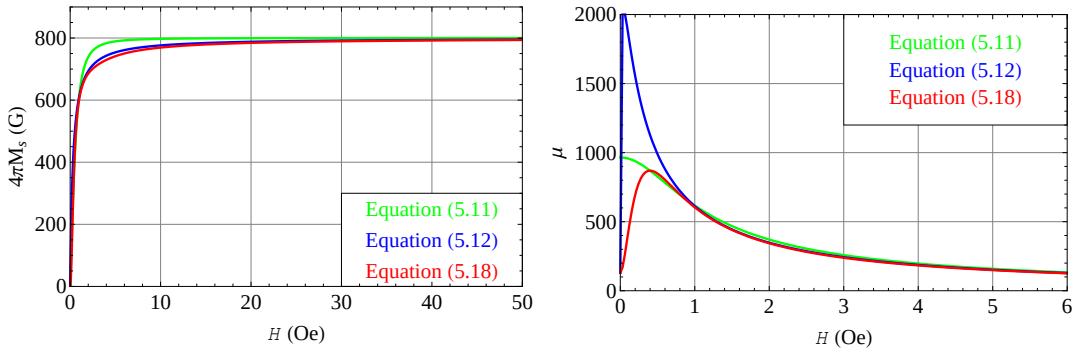

(b) Magnetization (c) Permeability

Figure 5.21: Ferrite TTVG-800. Hysteresis loop and approximate magnetization and permeability curves.

and 5.24. Unlike the (5.11) model, the quadratic behavior at low fields is incorporated in the equation, but it is not obvious from the figures. This model is more flexible but it is still unable to satisfy the third criterion for all considered ferrites.

The main disadvantage of the first two models is that they are not sufficiently robust to satisfy the second and third criteria. Contrary to these models, the approximation (5.18) suggested in this study shows excellent ability to approximate available curves; using this model we were able to satisfy all three criteria. The

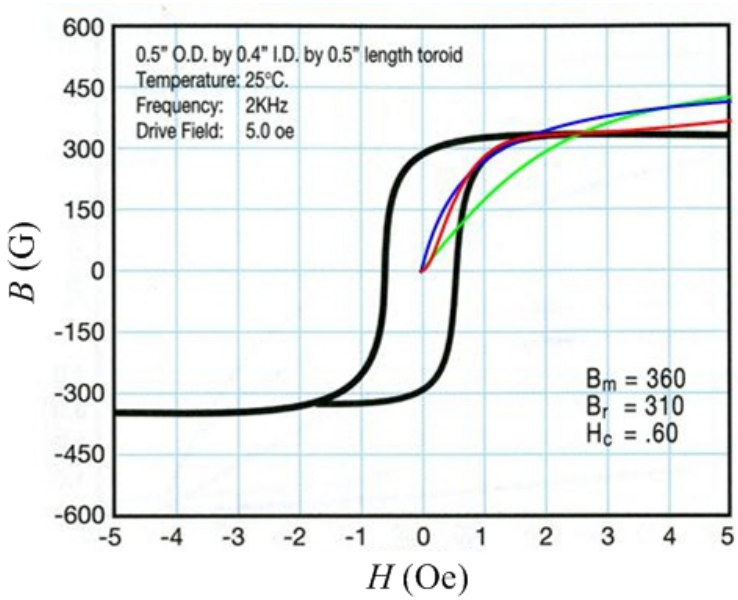

(a) Hysteresis loop

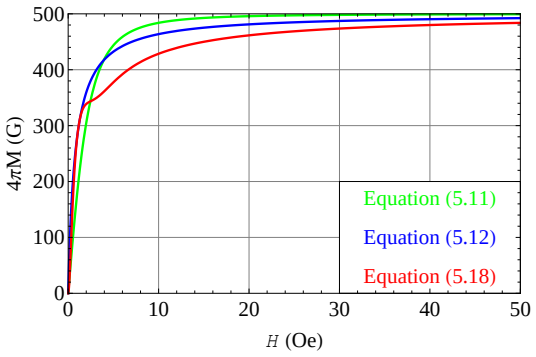

(b) Magnetization

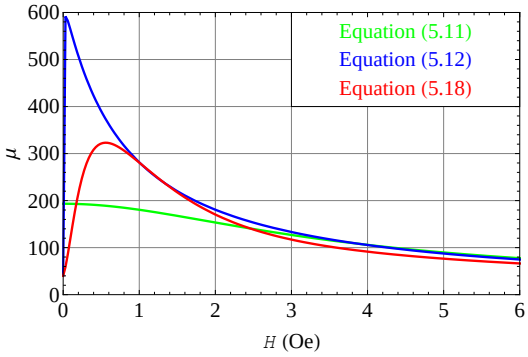

(c) Permeability

Figure 5.22: Ferrite G-475. Hysteresis loop and approximate magnetization and permeability curves.

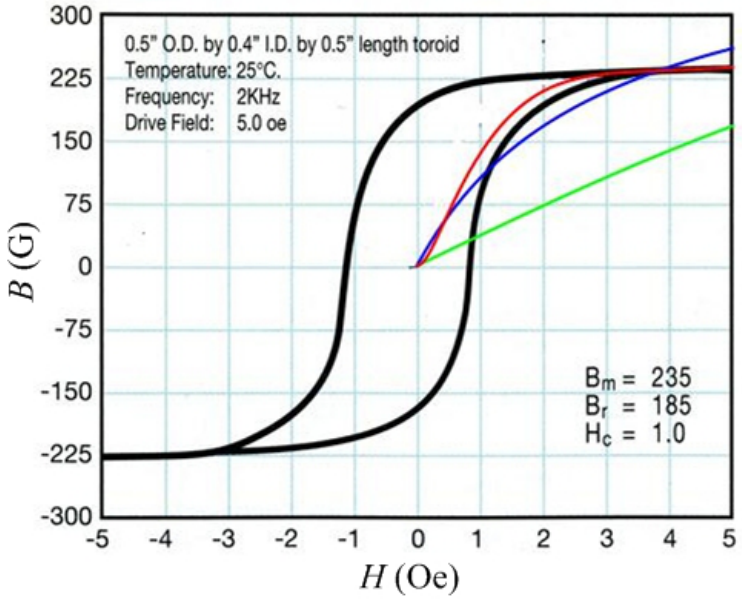

(a) Hysteresis loop

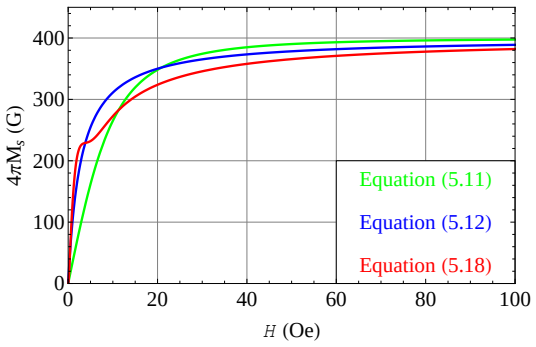

(b) Magnetization

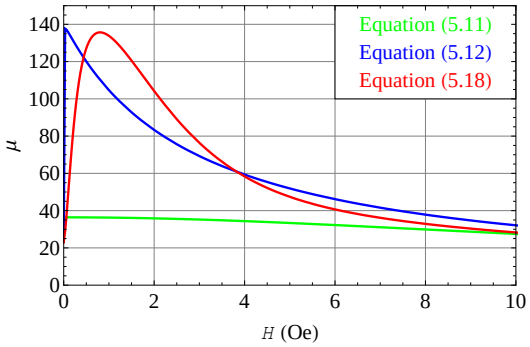

(c) Permeability

Figure 5.23: Ferrite G-1006. Hysteresis loop and approximate magnetization and permeability curves.

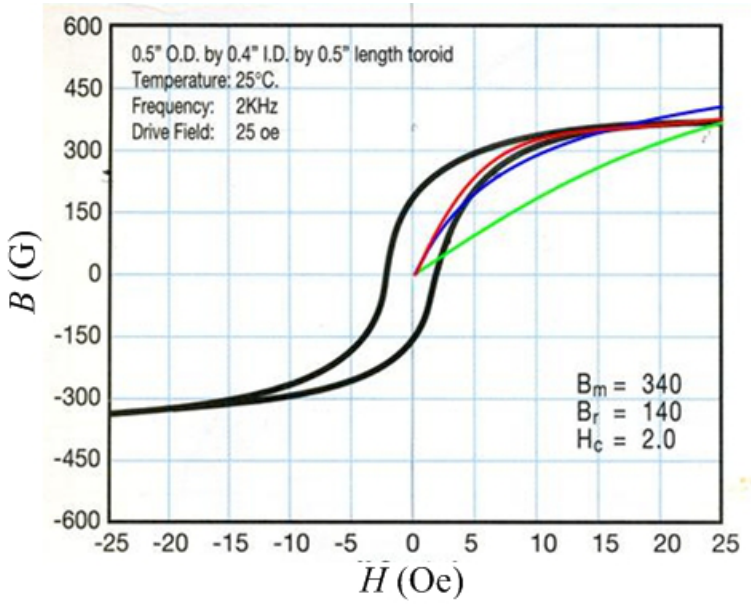

(a) Hysteresis loop

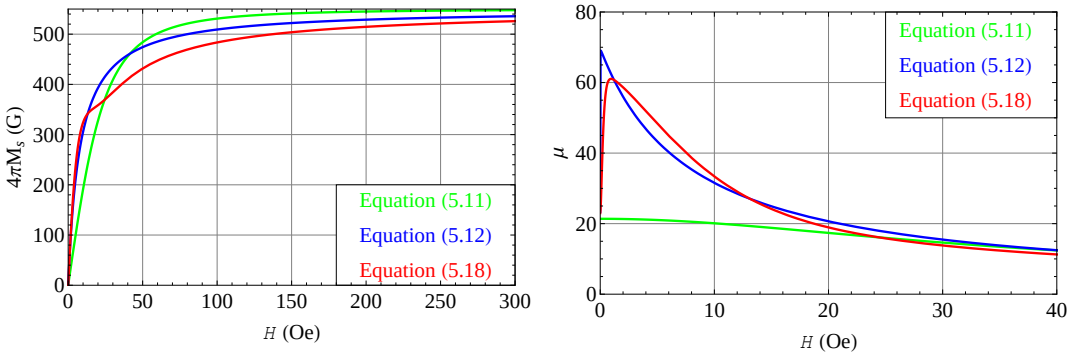

(b) Magnetization

(c) Permeability

Figure 5.24: Ferrite TT2-113. Hysteresis loop and approximate magnetization and permeability curves.

quadratic behavior of (5.18) can be seen in the figures, and it is also explicitly evident from the governing equation which, as was mentioned earlier, reduces to (5.16) at low fields and can be recognized as a quadratic function of H. However, this model has one serious disadvantage; namely, the number of adjustable parameters. To obtain the red curves in Figures 5.21 - 5.24, four parameters had to be determined. Unfortunately, the effect of each parameter cannot be isolated and clearly identified. In addition, the set of parameters giving good approximation is not unique. Thus, the freedom and flexibility provided by the four-parameter adjustment also makes curve-fitting rather difficult, cumbersome and not intuitive.

The applicability of these approximations depends on the range of the argument H in (5.11), (5.12), and (5.18). If very low fields are expected, then it is better to use a more complex model like (5.18). On the other hand, if the magnetic field is expected to be sufficiently strong to ensure saturation of the ferrite material, simpler models are also adequate. In our analysis, all three models were tested and found to produce identical results. It is concluded that for the designs examined in this study the magnetic field inside the ferrite material rarely reduces to very low values; therefore, the simpler model (5.11) can be used with confidence.

Chapter 6

MODELING USING ANSYS HFSS

Analysis of the ferrite-loaded CBS antennas in this study is primarily based on a narrow rectangular ($7.62 \times 1.27 \times 5.08$) cm cavity. Two photographs of such a partially assembled CBS antenna are shown in Figure 6.1. The cavity is aluminum with the open top side to allow radiation of the electromagnetic waves. The cavity is excited with a triangular brass probe which is soldered to the inner conductor of the 50-Ω coaxial transmission line. The coax cable is attached to the cavity at the center of the wall, 2.54 cm from the bottom, via the sma or ssma connector. Although not shown in the photographs, the cavity is flush-mounted on the (30×30) cm steel ground plane.

The cavity is partially loaded with one of the ferrite materials discussed in Section 5.3. Several loading configurations are presented in Chapter 7 along with the corresponding measurements and simulations of the input impedance and radiatin patterns. The ferrite materials are biased using the permanent magnets or an electromagnet arranged in a symmetric or asymmetric configuration as discussed in Section 5.1. Several of such biasing configurations, along with the corresponding measurements and simulations, are presented in Chapter 7.

The analysis of the radiation characteristics (also referred to as the radio frequency or RF analysis) of the ferrite-loaded CBS antenna shown in Figure 6.1, was performed using commercial software Ansys HFSS v.13.0, as well as our own FEM computer code written in Fortran 90. Simulations in HFSS are based on the pure Finite Element Method whereas simulations using our Fortran code are based on the hybrid FEM/MoM technique. To perform the modeling and simulations using either of these tools, the following information is necessary:

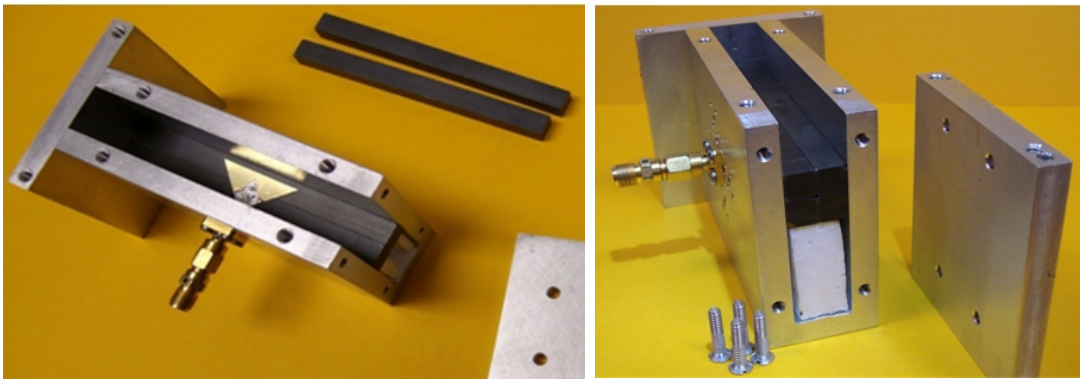

(a) Top view. (b) Side view.

Figure 6.1: A partially assembled ferrite-loaded CBS antenna.

- Computer-aided design (CAD) and discretization of the geometry.
- Boundary conditions and excitation.
- Material properties.

In addition, when the Fortran code is used, a very important issue needs to be addressed; namely, solution of the global finite element matrix. This issue is discussed at the end of this chapter.

Computer-Aided Design.

The first step in the numerical RF analysis is the modeling of the geometry of the antenna on a computer, and its discretization into finite elements. When using the Fortran code, the geometry is created and discretized using CAD software package I-Deas NX. A typical design is shown in Figure 6.2. The physical cavity is flush-mounted on the finite ground plane; however, in the hybrid FEM/MoM formulation, infinite ground plane has to be assumed.

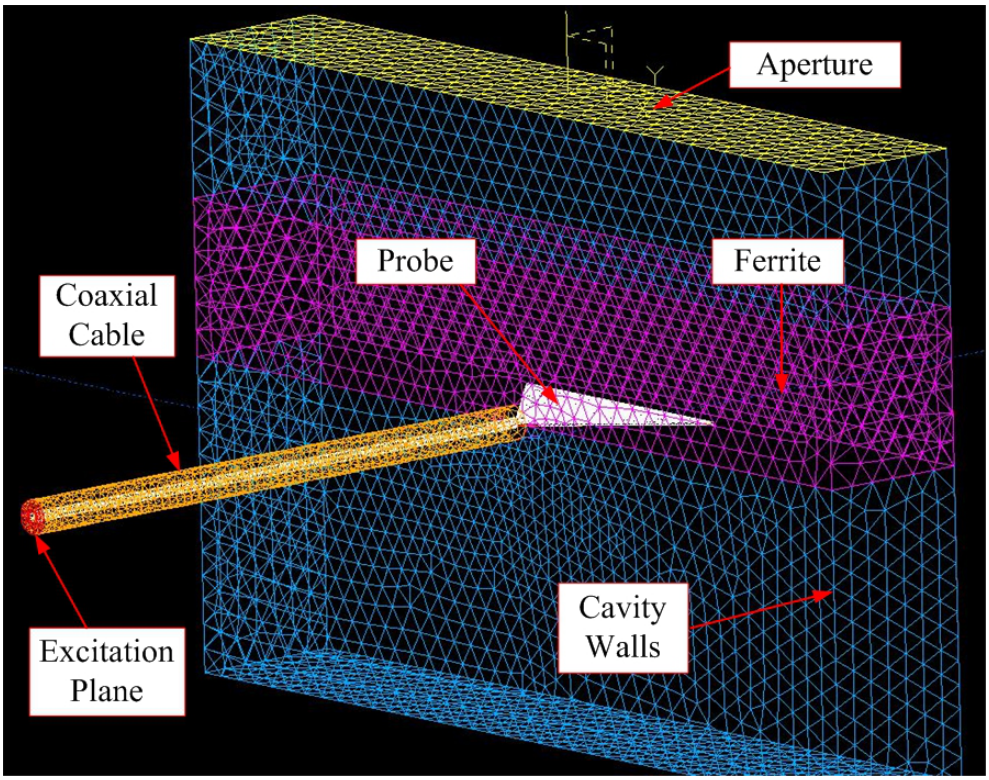

(a) CAD model and typical mesh.

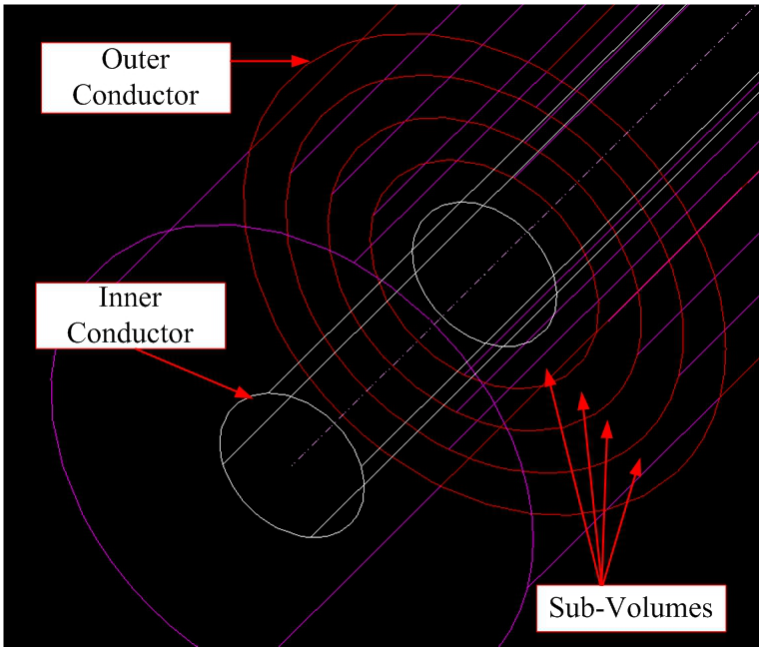

(b) Partitioning of the coaxial cable into four sub-volumes.

Figure 6.2: Computer-aided design of a ferrite-loaded CBS antenna in I-Deas NX.

The interior of the problem, which consists of the cavity and the coaxial cable, constitutes the FEM part of the formulation. This part is discretized (meshed) using linear tetrahedral elements [7] (one possible mesh can be seen in Figure 6.2a). The size of the elements, also referred to as the *mesh size*, is very important and can be detrimental to the numerical simulations. Usually, the finer mesh (smaller elements) provides more accurate results. However, the finer mesh also results in many unknowns, which leads to inefficient analysis and long computational time. The primary factor determining the size of the mesh is the frequency. As a rule of thumb, it is recommended that the electrical size of the elements is at most $\lambda/10$ [48, 18]. However, many other factors can influence the mesh size as well, to name just a few:

- Geometry. Irregular geometries may require finer mesh to accurately represent the EM field distribution. For example, curved surfaces usually require smaller elements than planar surfaces to properly represent the effect of the curvature on the EM field. Also, smaller elements may be required to model geometrical features with the physical size less than $\lambda/10$. For instance, the distance between the inner and outer conductors of a typical coaxial cable is approximately 1.0 mm, which is $\lambda/300$ at $f = 1.0$ GHz.

- Materials. Boundaries of the materials constitute transition between two different media. In the vicinity of such interfaces, electromagnetic field often exhibits rapid spacial variations; therefore, smaller elements may be needed to capture these variations.

- Type of the finite elements. Two main types of the elements used in the finite element analysis are the nodal and edge elements. The nodal finite elements are the elements for which the degrees of freedom (unknown quantity such

as the potential or the electric/magnetic field) are assigned to certain fixed nodes in the element. In a linear tetrahedral element, for instance, these are the vertices of the tetrahedra. Such elements are most suitable for the FEM analysis formulated in terms of the scalar potentials like the total and reduced scalar potentials in Chapter 4. The edge elements, also called the vector elements, are the elements for which the degrees of freedom are assigned to the edges; like the edges of a tetrahedra. In formulations involving the electric or magnetic fields as unknown quantities, these elements are preferred because they are more convenient in imposing the boundary conditions at the material interfaces [7]. Using the 'right' type of elements facilitates the analysis and can ensure the accuracy which would otherwise be only possible through mesh refinement. For instance, conducting edges and corners are problematic for the nodal elements because of the associated field singularities. Using smaller mesh near such corners and edges can partially alleviate this problem, but often leads to a large number of unknowns. Edge elements, on other hand, treat them naturally because the degrees of freedom are associated with the edges rather than nodes.

- Interpolating functions. The interpolating functions, also known as the basis functions, are used to approximate the unknown solution within a finite element. For the edge elements, the most common interpolating functions are the zeroth-order and the first-order vector basis functions; essentially, they imply linear and quadratic approximation of the solution inside the element, respectively. The advantage of using zeroth-order interpolating functions, is that the integrals such as (2.16, 2.18, 2.19) can be solved analytically, which leads to simpler formulation. However, the analysis based on such basis functions exhibits poor convergence; the approximate solution approaches the exact one

very slowly as the mesh is refined [7]. This means that many more zeroth-order elements are usually required to achieve the accuracy which is comparable with the accuracy obtained using the higher-order elements. As a result, the size of the elements may have to be smaller than $\lambda/10$.

The discretization of the geometry into finite elements can be controlled, to some extent, by partitioning the total computational domain into several sub-volumes with different meshes. For example, three natural sub-volumes of the antenna in Figure 6.1 are the coaxial cable, the ferrite material, and the air-filled space in the cavity. Sometimes, these sub-volumes may need to be further partitioned into smaller volumes. In the I-Deas NX design, for instance, the coaxial cable is radially partitioned into four additional sub-volumes as shown in Figure 6.2b.

Despite the desire to improve the accuracy of the results by using a finer mesh, in the numerical modeling and simulations a tradeoff between good accuracy and reasonable computational time should often be considered. The analysis usually starts with a coarse mesh which is then refined until the accuracy of the results is no longer significantly affected by further refinement. The notion of 'significantly affected' depends on the engineering judgement and the problem under consideration. For instance, if the radiation pattern of the antenna is of primary interest, then closer attention should be paid to the mesh in the aperture. On the other hand, if accurate computation of the input impedance is required, then finer mesh at the coax-cavity interface and near the feed may be necessary. Through such gradual mesh refinement/analysis, it was determined that at the frequencies around 1.0 GHz, the acceptable results are obtained if the geometry in Figure 6.2 is discretized using the mesh size of 0.05 cm, 0.2 cm, and 0.2 cm for the coax cable, ferrite material, and the air in the cavity, respectively. In I-Deas NX, such a mesh yields $100,000 - 120,000$ zeroth-order vector elements and $120,000 - 150,000$ degrees of freedom, edges.

When Ansys HFSS is used for the numerical RF analysis, a typical model is shown in Figure 6.3. This model is identical to the I-Deas NX model in Figure 6.2a, except for the following two differences:

- The size of the ground plane.
- The presence of the enclosing boundary.

These differences are due to the fact that the hybrid FEM/MoM and the pure FEM techniques account differently for the infinite space around the antenna. The Hybrid FEM/MoM does not require an enclosing boundary because the EM field in the free space is governed by the half-space Green's function through the MoM part of the formulation [7]. However, this formulation requires that the ground plane is infinite in extent. The pure FEM, on the other hand, requires that the unbounded domain is truncated and it utilizes special boundary conditions to account for the fact that such a truncation is artificial and should not affect the propagation of the electromagnetic waves.

The meshing in Ansys HFSS is simpler and more automated than in I-Deas NX; HFSS performs adoptive meshing until the specified criterion of 'Maximum Delta S' is satisfied. However, the mesh obtained in such a way is not always sufficient to ensure good results. To demonstrate it, Figures 6.4a and 6.4b show the following two meshes:

a) Mesh 01. Mesh inside the ferrite material obtained through adaptive meshing with the convergence criterion of Maximum Delta S = 0.01.

b) Mesh 02. Mesh inside the ferrite material assigned by the user by setting the Maximum Length of Elements = 0.3 cm.

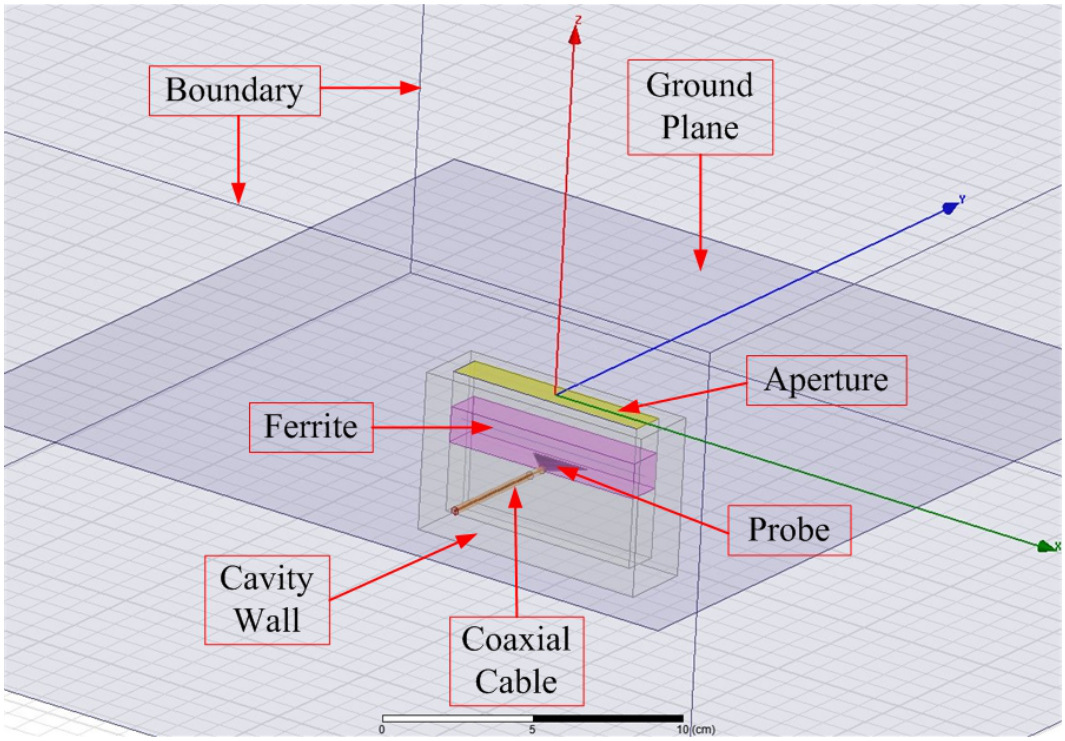

Figure 6.3: Computer-aided design of a ferrite-loaded CBS antenna in Ansys HFSS.

Figure 6.4c shows the simulations of the input impedance using these meshes; the measured input impedance is also included in the figure, black curve. It is obvious that the adaptive mesh, Mesh01, resulted in the less accurate simulation than the user-defined mesh, Mesh02. The conclusion is that the adaptive mesh generated in Ansys HFSS does not always guarantee accurate results and should always be checked against a finer user-defined mesh.

Unlike our Fortran hybrid FEM/MoM code, which utilizes only the zeroth-order vector elements, Ansys HFSS has an option to use elements of up to the second-order, including the possibility to use the mixed-order elements. The default choice is the first-order vector elements. When the Mesh02 is used to discretize the ferrite material, the total number of such elements in our Ansys HFSS simulations is about $40,000 - 70,000$.

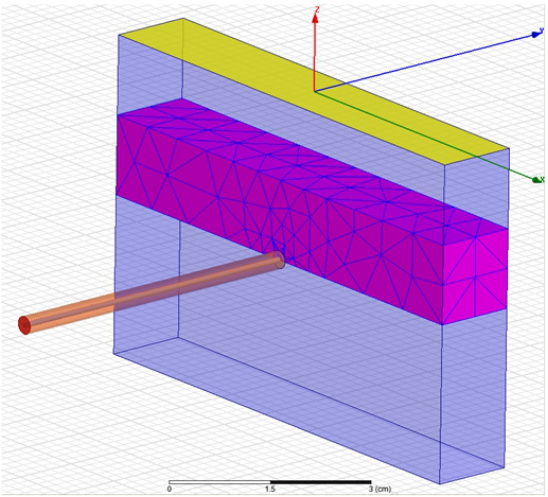

(a) Mesh 01.

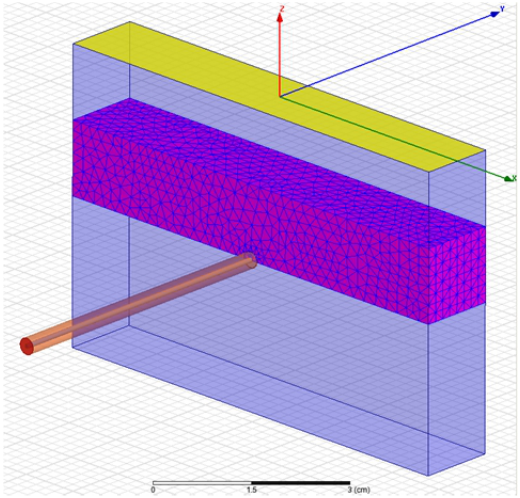

(b) Mesh 02.

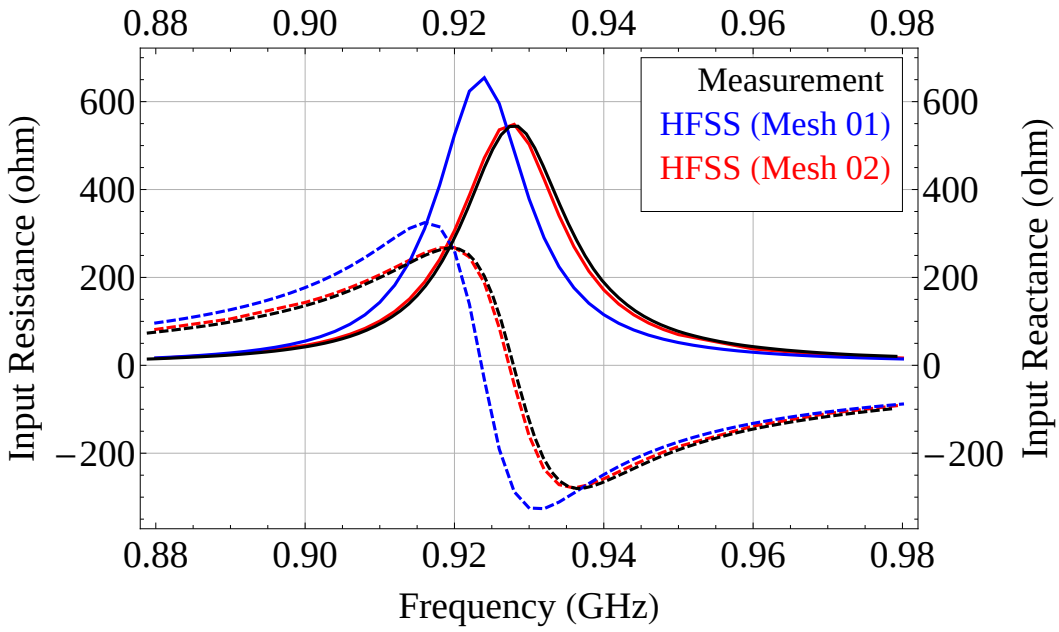

(c) Input impedance.

Figure 6.4: Comparison of the input impedance simulations using two different meshes inside the ferrite material.

Boundary Conditions and Excitation.

Having created and discretized the computer-aided design of the ferrite-loaded CBS antenna, the next step is to assign the boundary conditions and excitation. Depending on the technique, hybrid FEM/MoM or pure FEM, several of the following surfaces/interfaces may require such attention:

- Metallic surfaces.
- Aperture.
- Closing boundary.
- Excitation plane.

Metallic surfaces such as the aluminum walls of the cavity, copper inner and outer conductors of the coaxial cable, brass probe, and the steel ground plane are assumed to be perfect electric conductors (PEC). In Ansys HFSS, such surfaces are designated as the 'Perfect E' boundary. In I-Deas NX, they are marked accordingly and later recognized by the Fortran code as the boundaries where the Dirichlet boundary condition should be imposed by setting the tangential electric field to zero, $E_{tan} = 0$.

In the hybrid FEM/MoM formulation, the aperture requires special treatment because it represents the interface between the FEM and MoM domains (see Chapter 2). The continuity of the tangential electric and magnetic fields is imposed at this interface during the formulation stage by applying the boundary conditions (2.1). When modeling in I-Deas NX, the aperture should be uniquely marked to help the Fortran code identify it as the FEM/MoM interface. Since simulations in Ansys

HFSS are based on the pure FEM, no such subdivision into domains is made and no special treatment of the fields in the aperture is required.

Unlike the hybrid FEM/MoM, the pure FEM requires that the infinite domains are truncated and closed using appropriate boundary conditions. The rectangular box enclosing the antenna in Figure 6.3 represents such a truncation of the infinite free space into a bounded domain. For such a truncation to work, the walls of the box should be 'transparent' to the electromagnetic waves and do not induce artificial reflections. Such an ideal boundary is imitated in Ansys HFSS by specifying the radiation boundary condition on the sides of the enclosing box. The following two choices are available:

- First-order absorbing boundary condition (ABC).
- Perfectly Matched Layer (PML).

The choice of the closing boundary condition is mainly up to the user but it should be applied correctly to ensure that the final results are not affected by such artificial boundary. When ABC is used to truncate the domain, it is recommended that the radiation boundary is placed at least $\lambda/4$ away from the radiators and scatterers. Sometimes, satisfying this requirement can lead to very big computational domains and many unknowns. PML, on the other hand, can be placed much closer to the antenna, which results in a smaller domain and, possibly, less number of unknowns. However, PML is essentially a layer (or layers) of artificial material with non-zero thickness, which means that this material becomes part of the computational domain and has to be discretized as well. Moreover, relative permittivity and permeability as well as the dielectric and magnetic loss tangents of the PML are anisotropic quantities. In general, presence of such PML materials makes it more difficult for the iterative solver to reach convergence compared to the ABC.

Figure 6.5 shows simulations of the input impedance when the top side of the closing boundary (side above the aperture) is $\lambda/10 = 3.0$ cm and $\lambda/4 = 8.0$ cm away from the aperture at $f = 0.95$ GHz. The red and green curves represent the simulations with the ABC 8.0 cm and 3.0 cm away, respectively. The blue curve is the simulation with the PML 3.0 cm away from the aperture. The red and blue curves are identical and the green one indicates that this simulation is inaccurate because the ABC is too close to the aperture.

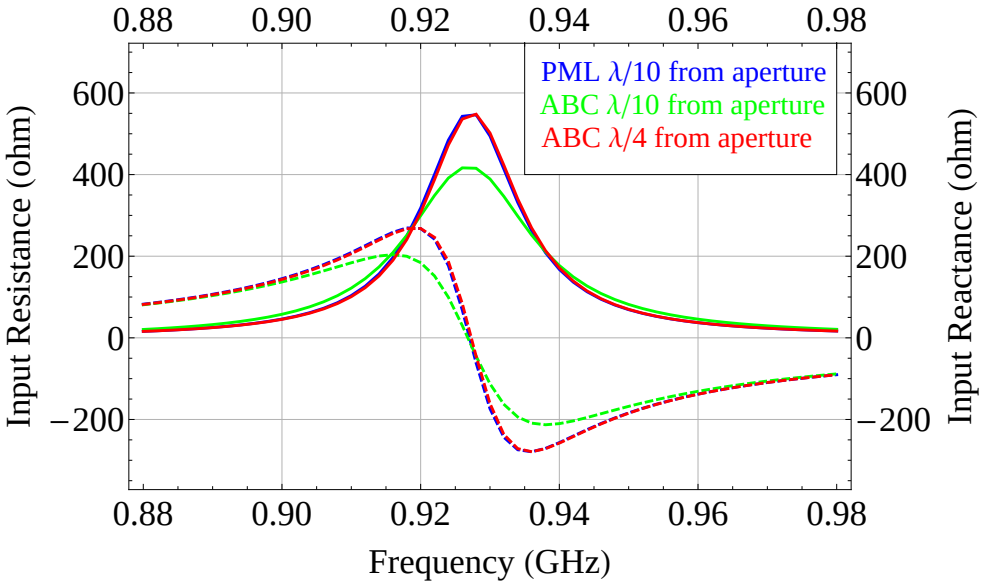

Figure 6.5: Simulation of the input impedance in Ansys HFSS using the first-order absorbing boundary condition (ABC) and the perfectly matched layer (PML) to truncate the infinite free space around the antenna.

The last issue is the excitation that needs to be specified at the plane marked 'Excitation Plane' in Figures 6.2 and 6.3. The excitation is the dominant propagating mode in the coaxial cable, TEM. In Ansys HFSS, it is specified by assigning the wave port to the plane and drawing the integration line as shown in Figure 6.6. In the Fortran code, it is represented by the TEM field distribution imposed at the excitation plane.

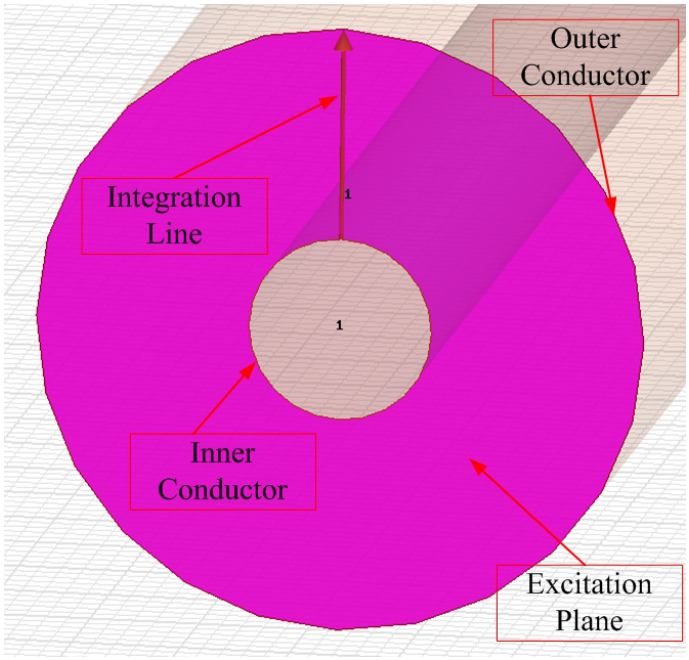

Figure 6.6: Wave port excitation in Ansys HFSS showing the integration line for the dominant TEM mode.

$$\vec{E}^{inc} = \hat{a}_\rho \frac{E_o}{\rho} e^{-\gamma z} \tag{6.1}$$

where, E_o is the amplitude of the electric field, $\gamma = \alpha + j\beta_z$, α is the attenuation constant, $\beta_z = \beta_o\sqrt{\epsilon_r \mu_r}$ is the coax wave number, and (ϵ_r, μ_r) are the relative permittivity and permeability of the coaxial cable, respectively.

The physical coaxial cable is rather long and modeling its entire length is unnecessary. Therefore, the excitation plane also serves as the truncation plane of the coaxial cable a distance L from the coax-cavity interface (see Figure A.1). The dominant mode propagates towards the coax-cavity interface where it is partially reflected back towards the excitation plane. Since such truncation is artificial, the reflected mode should pass through this plane unaffected. In the Fortran code, this is taken care of by applying the first-order absorbing boundary condition at the truncation plane.

In addition, the coax-cavity interface represents a discontinuity where multiple higher-order modes can be created. However, these modes are non-propagating and exhibit fast attenuation. This, of course, depends on the dimensions of the coaxial line and the frequency of operation. For our coaxial cable, the approximate cut-off frequency of the next propagating higher-order mode is [49]:

$$f_c \simeq \frac{1}{\pi(a+b)\sqrt{\mu\varepsilon}} = \frac{c}{\pi(0.4191+1.341)\times 10^{-3}\sqrt{2.085}} = 37.5 \text{ GHz} \tag{6.2}$$

where c is the speed of light, a and b are the radii of the inner and outer conductors of the coaxial cable, and 2.085 is the dielectric constant of Teflon. Since the first-order ABC imposed at the excitation plane can only handle the dominant TEM mode, the modeled length L should be long enough to ensure sufficient attenuation of the higher-order modes. On the other hand, the coaxial cable region may introduce many unknowns and therefore is desired to be as short as possible. It was found that the distance L should be at least $\lambda/6$.

Material Properties.

The main concern here is the frequency-dependent permeability tensor (3.2) which describes the response of the ferrite material to the time-harmonic electromagnetic field, subject to a given magnetization state of the material. Besides frequency, this tensor also depends on the saturation magnetization $4\pi M_s$, and the linewidth ΔH. Their nominal values are listed in Table 5.1 for the ferrite materials used in this study. However, these values are subject to tolerances, as indicated in the table, and should not be treated as fixed inflexible constants. In addition, some of them, linewidth for instance, depend on frequency [25]

$$\Delta H = \frac{2\alpha}{\gamma}\omega \tag{6.3}$$

where α is a dimensionless, positive, phenomenological parameter which describes the magnitude of the loss, and γ is the gyromagnetic ratio. ΔH given in Table 5.1 is usually measured at 9.4 GHz [21]; therefore, at frequencies much lower than 9.4 GHz, ΔH can be quite different from its nominal value. Moreover, these numbers represent properties of a saturated, uniformly magnetized ferrite material. When material is not saturated or non-uniformly magnetized, some of them loose meaning. Saturation magnetization, for instance, may not be a valid representation of a partially saturated material, and linewidth may be broader (greater) to reflect greater losses associated with such a state [23]. Thus, reasonable adjustment of the values in Table 5.1 should be permitted.

Another very important quantity in (3.2) is the magnitude of the internal magnetic field, $H = |\vec{H}^i|$. Three approaches to compute this field are discussed in Chapter 4 which, in general, give three different internal magnetic field distributions. Therefore, based on these approaches, three different permeability tensors can be obtained. When the permeability tensor is computed in Approach 1, it is found to be constant throughout the ferrite material i.e., (3.2) is the same everywhere in the material. In contrast, in Approaches 2 and 3, (3.2) is position dependent; it is different at every point in the ferrite because the magnitude of the internal field, $|\vec{H}^i|$, is varying with position. Thus, as far as the FEM part of the analysis is concerned, in Approach 1, (3.2) is computed only once at each frequency and then assigned to all the elements in the ferrite domain; whereas, in Approaches 2 and 3, each element is assigned individual and, in general, unique permeability tensor.

The effective permeability can be defined as [9]

$$\mu_{eff} = \frac{\mu^2 - \kappa^2}{\mu} \tag{6.4}$$

where $\mu = (1 + \chi)$, and χ and κ are given by (3.3). When the real part of (6.4) is

plotted versus the internal field $|\vec{H}^i|$, it can be seen that in Approach 1 it is constant and positive throughout the ferrite material. On the other hand, in Approaches 2 and 3, it is non-uniform and can even become negative, indicating cut-off regions. Such regions may have significant impact on the distribution of the time-dependent EM fields and, as a result, radiation characteristics of the antenna.

Solving the Global Finite Element Matrix.

The last issue is the solution of the linear system of equations resulting from the discretization of the original partial differential equation 2.10

$$[A]\{x\} = \{b\} \tag{6.5}$$

where $[A]$ is the global FEM matrix, $\{x\}$ is the unknown vector, and $\{b\}$ is the known excitation vector. When the hybrid FEM/MoM method is used, matrix $[A]$ is sparse, complex, and non-symmetric (non-symmetry is due to the presence of the anisotropic materials, such as ferrites). Conjugate gradient methods are widely used iterative techniques to solve such a system. In [10], Conjugate Gradient Squared (CGS), BiConjugate Gradient (BiCG) and Quasi Minimum Residual (QMR) have been used and found adequate to solve (6.5). The preference was given to the variant of the CGS method known as the Conjugate Gradient Squared 2 (CGS2) with Jacobi Preconditioning.

Performance of the iterative solvers is often evaluated in terms of the number of iterations or the computational time required to satisfy a specified convergence criterion. Iterations usually terminate when the residual $r = b - Ax$ is sufficiently small. The *relative tolerance* termination criterion is [50]

$$\frac{\|r\|}{\|b\|} < \tau \tag{6.6}$$

Unfortunately, it was often observed in this study that the CGS2 solver exhibits very poor convergence whenever the permeability tensor is computed using the non-uniform internal magnetic field in Approaches 2 and 3. Table 6.1 shows typical performance of the Jacobi Preconditioned CGS2 solver on a laptop computer with Intel(R) Core(TM) i7-2860QM CPU @ 2.50 GHz. The matrix $[A]$ is $(120,000 \times 120,000)$, sparse, complex, and non-symmetric. The convergence criterion is $\tau < 1.0e^{-5}$. The table shows two sets of solutions: one at the resonant frequency 0.91 GHz and the other at the lower, off-resonance frequency 0.8 GHz. Each set has three solutions corresponding to the three approaches. The numbers shown are the number of iterations and the elapsed time.

Table 6.1: Performance of the CGS2 iterative solver.

Frequency (GHz)	Approach 1	Approach 2	Approach 3
0.85	41053 0:15:24 Converged	99996 1:13:17 Converged	68301 0:49:59 Converged
0.93	102012 0:51:09 Converged	1,500,000 $\approx$ 7 hours Not Converged	1,500,000 $\approx$ 7 hours Not Converged

The results in Table 6.1 demonstrate that the convergence of the CGS2 solver depends on the frequency; the number of iterations and the convergence time are greater for frequencies near resonance. Moreover, the performance of the solver also depends on the uniformity of the global matrix [A]. Whenever the non-uniform permeability tensor is used (Approaches 2 and 3), the performance of the iterative solver deteriorates substantially and it often fails to converge even after 7 hours and 1,500,000 iterations.

Such poor performance was not uncommon and it was greatly slowing down the analysis. In an attempt to fix this problem, several other variants of the conjugate

gradient and minimum residual methods were considered in this study [51, 52, 53]. In very rare cases, generalized Biconjugate Gradient Stabilized method, Bi-CGstab(l) [54], outperformed CGS2 but none of these methods really resolved the issue. Thus, it was decided to abandon the iterative solver and switch to the direct solver known as the Frontal solver [55]. This solver is based on the Gaussian Elimination and utilizes sparsity of the FEM matrix to avoid unnecessary operations involving zeros. Using this solver, it takes approximately 2 hours to solve the above-mentioned matrix on the same machine. Obviously this is still not a fast solver, but the improvement is substantial considering that

a) The direct solver guarantees the solution.

b) It has stable performance which is independent of frequency.

Moreover, significant improvement in speed can be achieved by implementing basic parallelization using the OpenMP directives. The above-mentioned laptop has four cores and eight threads. When all eight threads are utilized, it takes only 26 minutes to solve the matrix at one frequency.

It should be mentioned that Ansys HFSS is using the iterative solver whenever possible and, in the case of an ill-conditioned matrix, switches to the direct Multi-Frontal solver. This is the the improved version of the Frontal solver that uses several independent fronts at the same time [56]. Ansys HFSS significantly outperforms our Fortran code in terms of the computational speed.

Chapter 7

SIMULATIONS AND MEASUREMENTS

The main goal of this chapter is the demonstration of the effects of the non-uniformly biased ferrite material on the radiation characteristics of the ferrite-loaded cavity-backed slot antennas. This demonstration serves to support the following premise:

> *Severely non-uniform magnetic bias field distribution has to be included in the numerical analysis, if accurate results are to be attained.*

Since the biasing magnetic field (internal field) depends on the applied and demagnetizing magnetic fields (see Chapter 4), this premise implies that if these fields are very non-uniform, then averaging their actual distributions to simplify the analysis is unacceptable because it will most likely lead to inaccurate magnetic bias field and, consequently, inaccurate predictions. The primary observable is the input impedance of the antenna simulated/measured at the coax-cavity interface. The premise is verified by comparing simulations of the input impedance with measurements. The three main steps of the numerical analysis are

1. Compute magnetic field inside the ferrite material.
2. Compute frequency dependent permeability tensor.
3. Solve antenna radiation problem.

The first step is the computation of the internal magnetic field inside the ferrite material. Three approaches to compute this field are discussed in Chapter 4 and the computer-aided modeling using Ansys Maxwell 3D is discussed in Chapter 5. The second step is the computation of the frequency dependent permeability tensor (3.2). This tensor depends on the internal magnetic field computed in the

first step. Since there are three ways to compute the internal field, there are three different permeability tensors that can be obtained in step two. In the third step, the permeability tensor is used to obtain predictions of the input impedance and the radiation patterns using the commercial software Ansys HFSS or our personal 'home-built' Fortran FEM code as described in Chapter 6. The accuracy of these predictions depends on the accuracy of the permeability tensor computed in step two.

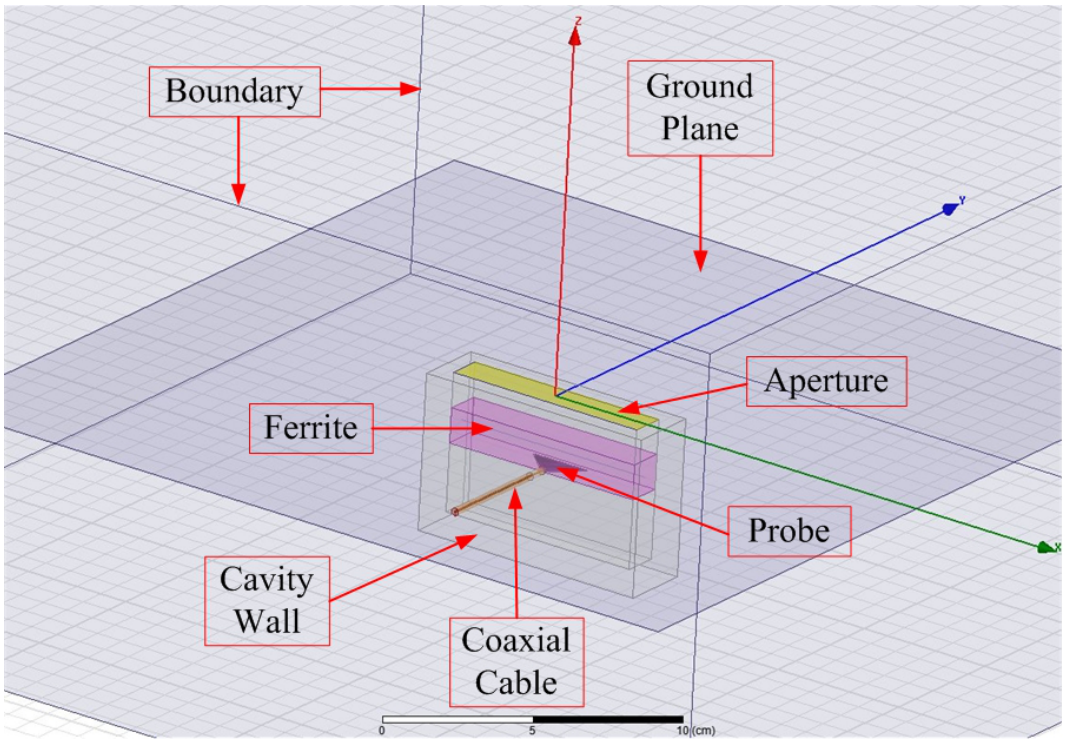

Figure 7.1: Computer-aided design in Ansys HFSS.

The analysis is mainly based on a narrow rectangular CBS antenna. The Ansys HSFF model of this antenna is shown in Figure 7.1. The inner dimensions of the cavity are $(7.62 \times 1.27 \times 5.08)$ cm and the thickness of the walls is 0.66 cm. The walls of the actual physical cavity are made of aluminum, but in the Ansys HFSS model they are modeled as PEC objects. The majority of the simulations and measurements were performed on the cavity loaded with one layer of the ferrite

material on top of the probe as shown in the figure. The thickness of the ferrite layer is 1.27 cm. Besides this loading configuration, one other configuration is presented in Section 7.4 with the ferrite moved all the way to the aperture.

The cavity is excited with a triangular probe which is soldered to the inner conductor of the coaxial cable. The probe and the inner conductor are modeled as copper materials, but can be equivalently modeled as PEC. The dielectric of the coaxial cable is Teflon ($\varepsilon_r = 2.0854$) with the inner and outer radii of 0.04191 cm and 0.1397 cm, respectively. The length of the modeled coaxial cable is $L = 5.0$ cm which is $\simeq 0.16\lambda$ at $f = 0.95$ GHz (typical resonant frequency in the analysis).

The cavity is flush-mounted on the square (30×30) cm ground plane which is modeled as a sheet with zero thickness and the 'Perfect E' boundary condition. The entire structure, including the ground plane, is enclosed by the ($40 \times 40 \times 20$) cm box, truncating an infinite space around the antenna into a bounded domain. All sides of the box are assigned the first-order absorbing boundary condition. The top side of this boundary is 13.0 cm above the aperture.

To show consistency of the results, the analysis is performed using various ferrite materials and biasing configurations. Based on these configurations, the chapter is organized into four sections:

- Measurement Setup. Section 7.1 presents description of the procedures for the measurement of the S-parameters and the radiation patterns.
- Previous Geometries. Section 7.2 includes simulations and measurements of the input impedance of two ferrite-loaded CBS antennas used in the previous studies.
- Ferrite-Loaded CBS Antennas with Symmetric X-Biasing. Section 7.3 includes

simulations and measurement of the input impedance and radiation patterns of the CBS antennas loaded with the ferrite material which is biased in the x-direction using permanent magnets or electromagnet arranged in a symmetric configuration.

- Ferrite-Loaded CBS Antennas with Asymmetric X-Biasing. Section 7.4 includes CBS antennas loaded with the ferrite material biased in the x-direction using permanent magnets or electromagnet arranged in an asymmetric configuration.

- Ferrite-Loaded CBS Antennas with Asymmetric Z-Biasing. Section 7.5 includes CBS antennas loaded with the ferrite material biased in the z-direction using permanent magnets or electromagnet arranged in an asymmetric configuration.

Details of the biasing configurations, as well as the dimensions and computer-aided models are presented individually for each design in the corresponding sections.

7.1 Measurement Setup.

As was mentioned above, the main observable in the analysis is the input impedance of the CBS antennna. In addition to the input impedance, radiation pattern is another very important radiation characteristic of any antenna. Measurements of the input impedance and radiation patterns were performed at the electromagnetic anechoic chamber (EMAC) facility at the Arizona State University. Setups for the measurement of these radiation characteristics are discussed in the following subsections.

Measurement of the S-parameters.

A photo of the setup for performing S-parameter measurements is depicted in Figure 7.2. The instrumentation is an HP8510C Vector Network Analyzer configured with an S-parameter test set, and a synthesized source. The CBS antenna is located between the poles of a hand-wound electromagnet, shown in the lower left corner of the photograph. The magnet is placed on a non-ferrous platform. To its right is a DC power supply.

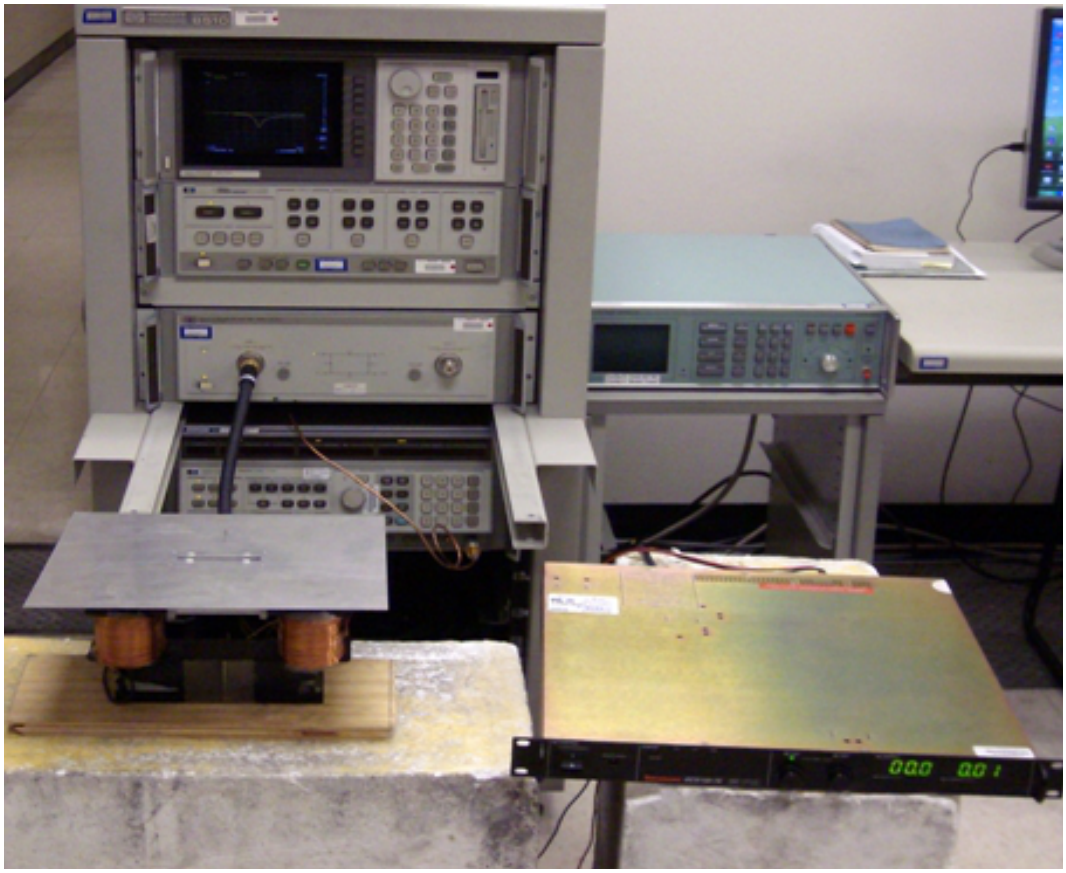

Figure 7.2: A typical setup for performing S-parameter measurements of a ferrite-loaded CBS antenna.

The first step is to determine the current required to produce the desired applied magnetic bias field in the antenna cavity. With the empty cavity between

the poles of the magnet, the probe of a Gauss meter is lowered into the center of the cavity. The applied magnetic field is monitored while the power supply current is increased. The power supply should be operated in constant current mode. Otherwise, as the electromagnet's coils heat up, their resistance increases and the current will change, thus changing the magnetic field magnitude.

After determining the current needed to produce the desired magnetic field, the network analyzer is calibrated at the end of the instrument cable. The standard open/short/load calibration is used. The microwave source is operated in 'Step Frequency' mode in which each frequency is phase locked. An IF averaging factor of 128 or more is used.

After calibration, the measurement phase reference plane is co-located with the calibration plane at the mating surface of the APC-3.5 connector of the instrument cable. To correspond with simulations, the reference plane needs to be shifted to the inside surface of the cavity.

Finally, the antenna is loaded with ferrite material, the ground plane is attached, and the antenna is placed between the poles of the electromagnet. It is a good idea to hold down the upper pieces of ferrite by inserting a piece of expanded polystyrene into the aperture and applying transparent adhesive tape across it and to the ground plane on either side. Otherwise, it is possible for the ferrite to "float" upward when the magnetic bias is applied.

Measurement of the Radiation Patterns.

A complete description of the measurement process would begin with "trueing up" the expanded polystyrene column. When the column is bolted to the positioner turntable, it is not necessarily aligned correctly. Without adjustment, the cut of

the pattern may not be the great circle azimuthal or elevation axis that is intended. Three of the six bolts which attach the column to the turntable have been modified to adjust up and down relative to the turntable surface. As the column rotates, the top of the column is observed relative to a stationary reference. The three bolts are adjusted up or down until the distance between the column and the stationary point is constant as a function of rotation.

Next, the measuring system is calibrated via the gain-transfer method. A horn antenna for which the gain versus frequency is known (either by calculation or by measurement) is the gain standard. The standard is placed on the column and it is adjusted in polarization and elevation using a spirit level. Its azimuthal orientation is adjusted for bore-site alignment, and the radiated power is measured as a function of frequency. In a compact range, that includes the application of a range gate to filter out the unwanted spillover from the feed antenna. For the stepped CW instrumentation available at the EMAC facility, the range gate is a software "time-domain" gate. With a time-domain system, the frequency-domain measurement is inverse Fourier transformed into the time domain. A band-pass filter is placed around the desired response thus filtering out all (ideally) extraneous responses that arise from the feed spillover and residual reflections from the anechoic chamber. After filtering, the response is Fourier transformed back into the frequency domain. Calibration coefficients are formed by taking the ratio of the known gain of the horn to its measured response. By applying the calibration coefficients to subsequent measurements, all of the amplitude effects (power of the microwave source, cable losses, impedance mismatches, propagation losses, etc.) are corrected for.

Now the gain standard is removed and replaced with the antenna under test. In many cases, this involves creating some sort of fixture or adapter out of expanded polystyrene such that the antenna will rest on the flat top of the support column at

the orientation needed to achieve a particular pattern cut. Also, the orientation of the test antenna is finely adjusted in polarization and elevation using a spirit level.

At this point, the acquisition software does the rest, according to the parameters specified. Typically, the antenna is sent to a particular azimuthal orientation by way of the positioning system. For a full 360 degree pattern, the starting point is designated as -179 degrees. There may be a short delay after each positioning before the measurement begins to ensure that any oscillatory motion has stopped. Then the gain measurement for that observation angle begins. This can take an appreciable amount of time for two reasons. First, in order to perform the time-domain processing, numerous points must be measured over a band of frequencies. Typically 401 or 801 frequency points are measured. Secondly, a significant advantage is obtained over the measurement noise by averaging. Each time that the number of averages is doubled, the noise floor of the system is lowered by 3 dB. The standard number of averages used at the electromagnetic anechoic chamber is 128, but the instrumentation is capable of performing 4096 averages. So, for each observation point there may be 401 frequencies that are measured 128 or more times each, which usually results in measurement times of between one and four hours for the entire 360 degrees in one degree increments.

Unfortunately, when ferrite-loaded CBS antenna was biased using the electromagnet, measurements of the radiation patterns were only partially successful. The reason is the following. As explained above, such measurements can take one to four hours. Over such period of time, coils of the electromagnet get very hot which may burn the wire isolation and destroy the magnet. Therefore, in order to avoid damaging the electromagnet, the process had to be stopped several times and resumed again after the coils have cooled down. Figure 7.3 shows one measurement obtained in such a way. As can be seen, the radiation pattern is discontinuous in

several places which is the result of such a stop-resume process. To avoid problems with coil overheating, the electromagnet can be replaced by the permanent magnets. Several measurements of the radiation patterns of the ferrite-loaded CBS antennas with the permanent magnets are presented in Sections 7.3, 7.4, and 7.5.

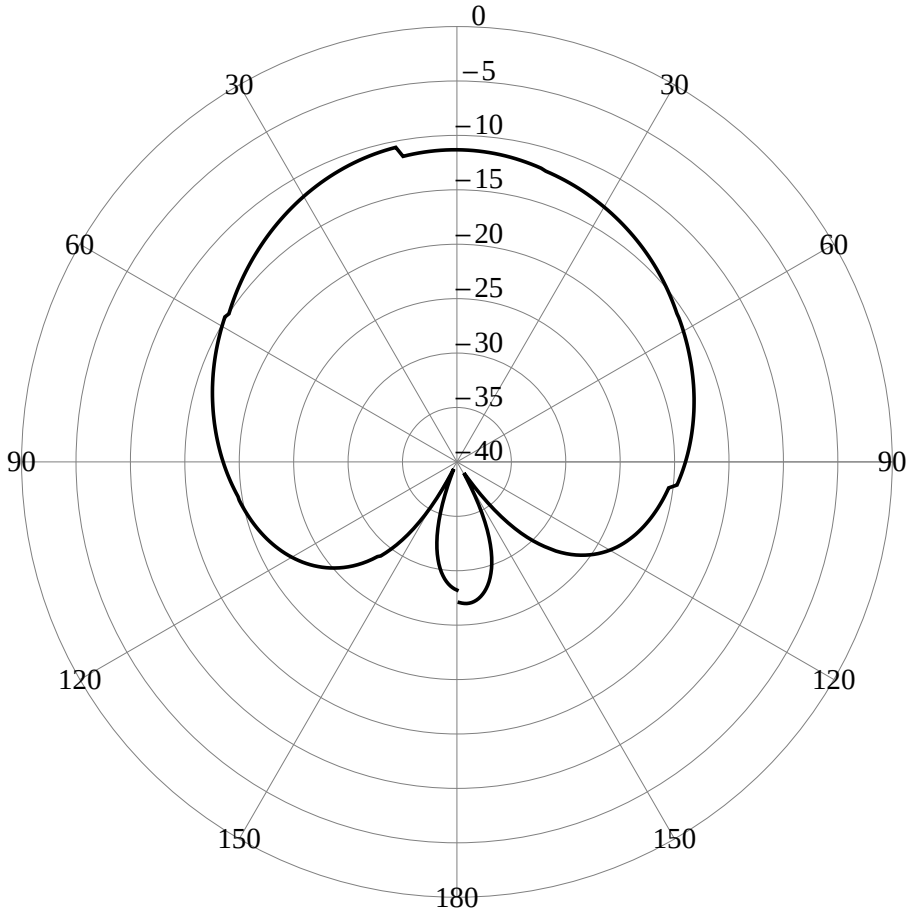

Figure 7.3: Measured E-plane radiation pattern of a ferrite-loaded CBS antenna biased by the electromagnet.

7.2 Previous Geometries.

This section re-introduces two ferrite-loaded CBS antennas which were used in the previous studies. The first design is based on the square cavity [12], and the second on the narrow rectangular cavity [14]. In the first design, the ferrite material is biased using the permanent magnets and in the second an electromagnet.

Simulations in [12] were based on the unform internal magnetic field found using Approach 1 and the predicted input impedance was shown to be in good agreement with measurements. In [14], an example was presented where Approach 1 was not sufficiently accurate and better predictions were attained using Approach 2. The purpose of this section is to re-simulate these results using Ansys HFSS and to examine how simulations based on Approach 3 compare with these simulations and measurements. It will be shown that whenever Approaches 1 and 2 provide adequate accuracy, Approach 3 also provides results which are as accurate or better. The simulations and measurements of the input impedances are organized into two sub-sections:

- Square cavity [12].
  - Weak magnetization.
  - Strong magnetization.
- Rectangular cavity [14].

Square Cavity.

The ferrite-loaded CBS antenna considered in this section is shown in Figure 7.4; this is the same antenna as in [12]. The square aluminum cavity, $(5.08 \times 5.08 \times 5.08)$ cm, is loaded with one layer of the dielectric material and two layers of the ferrite material, as shown in the figure. The permanent magnets are used to bias the ferrite materials in the x-direction, parallel to the length of the probe. For such biasing configuration, the coaxial cable prevents placement of the magnets right next to the walls of the cavity. Therefore, to accommodate the coaxial cable, a U-shaped piece of steel is inserted between the magnet and the cavity wall, as shown in the figure. The dimensions of the U-shaped piece are shown in Figure 7.4c.

The non-linear magnetostatic problem in Approach 3 is solved using Ansys Maxwell 3D model shown in Figure 7.5. The probe, coaxial cable, and the dielectric material are not modeled because they are non-ferrous objects with permeability $\mu = 1$ and, therefore, transparent to the static magnetic field. The U-shaped steel is modeled as the non-linear material, Steel-1008, from the Ansys Maxwell 3D library of materials. The ferrite material is TTVG-800, its initial magnetization curve is modeled using approximation (5.11) with the adjustable parameter H_1 given in Table 5.2. The permanent magnets are represented by another material from the Ansys Maxwell 3D library, NdFe35, but with slightly different magnetic coercivity. Two magnetization states of the ferrite material were simulated:

- Weak magnetization. One magnet on the left and one magnet on the right side of the cavity; the total width of the magnets on each side is 1.2 cm.
- Strong magnetization. Two magnets on the left and two magnets on the right side of the cavity; the total width of the magnets on each side is 2.4 cm.

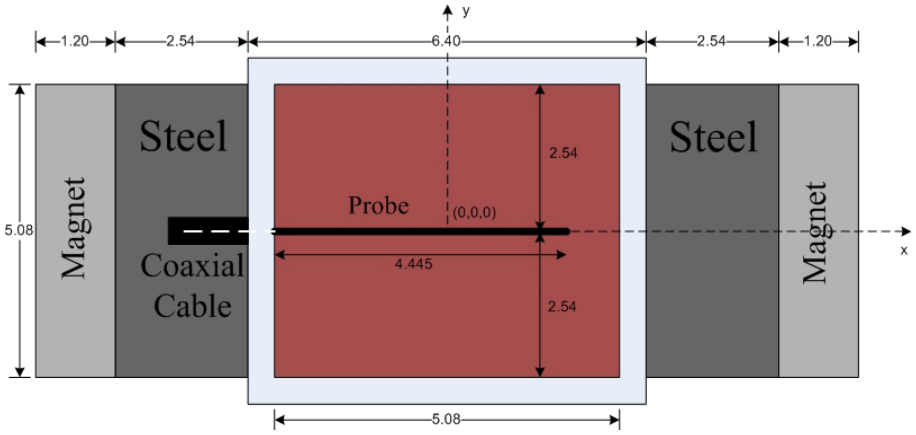

(a) Top view.

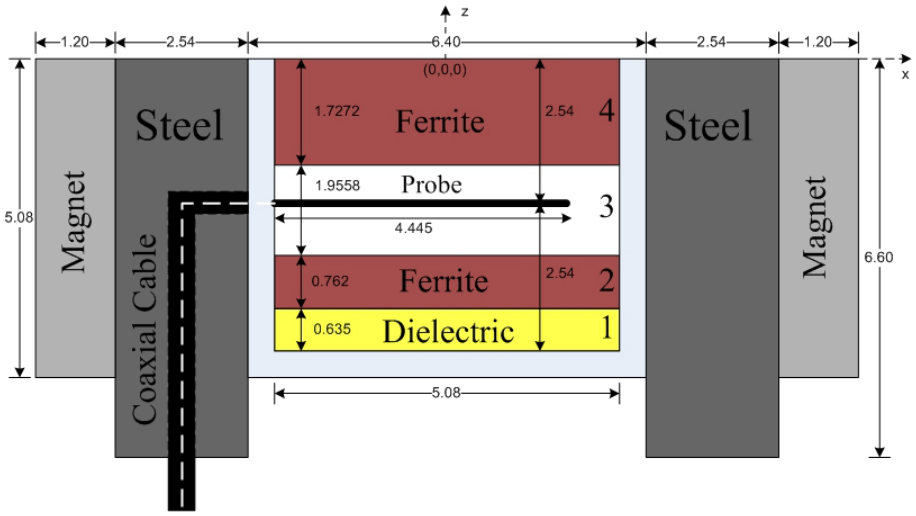

(b) Side view.

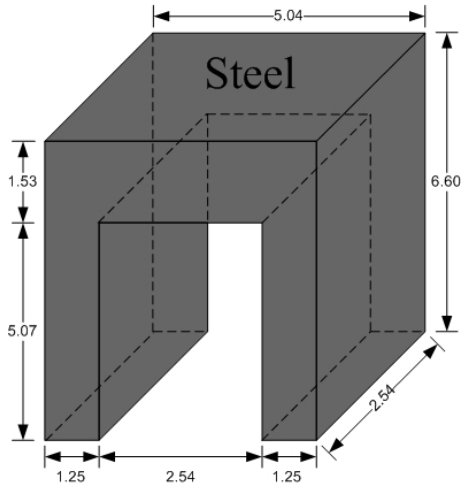

(c) U-shaped steel piece.

Figure 7.4: Square cavity loaded with two layers of TTVG-800 ferrite material biased in the x-direction using permanent magnets in symmetric configuration.

The internal magnetic field H^i for Approach 1 and the applied magnetic field H^a for Approach 2 are taken directly from [12]. The coercivity H_c for the permanent magnets in Approach 3 was adjusted until a good agreement between simulations and measurement was achieved. The values of the magnetic fields H^i, H^a, and H_c for the weak and strong magnetization states are listed in Table 7.1.

Table 7.1: Magnetic Fields in Ansys Maxwell 3D Simulations.

Magnetization	Approach 1 Internal field H^i (Oe)	Approach 2 Applied field H^a (Oe)	Approach 3 Coercivity H_c (kA/m)
Weak	238	384	-983
Strong	445	596	-920

The RF simulations were performed using the Ansys HFSS model shown in Figure 7.6. The magnets and the U-shaped steel are removed, but the probe, coaxial cable, dielectric material and the ground plane are added. The ground plane is (30×30) cm. The probe is a 4.445 cm long wire with the radius of 0.079248 cm. It is soldered directly to the inner conductor of the coaxial cable. The coax is modeled as a 50-Ω coaxial transmission line with Teflon ($\varepsilon_r = 2.085$) inside, and the inner and outer radii of 0.079248 cm and 0.26416 cm, respectively. Parameters of the dielectric and ferrite materials used in the RF simulations are shown in Table 7.2.

Table 7.2: Material Parameters in Figure 7.4.

Material	#	Thickness	Parameters
Dielectric	1	0.635	$\varepsilon_r = 2.2$
Ferrite: TTVG-800	2	0.762	$\varepsilon_r = 13.9$, $g = 2.00$
	4	1.7272	$4\pi Ms = 800$ G, $\Delta H = 10$ Oe
Air	3	1.9558	$\varepsilon_r = 1$

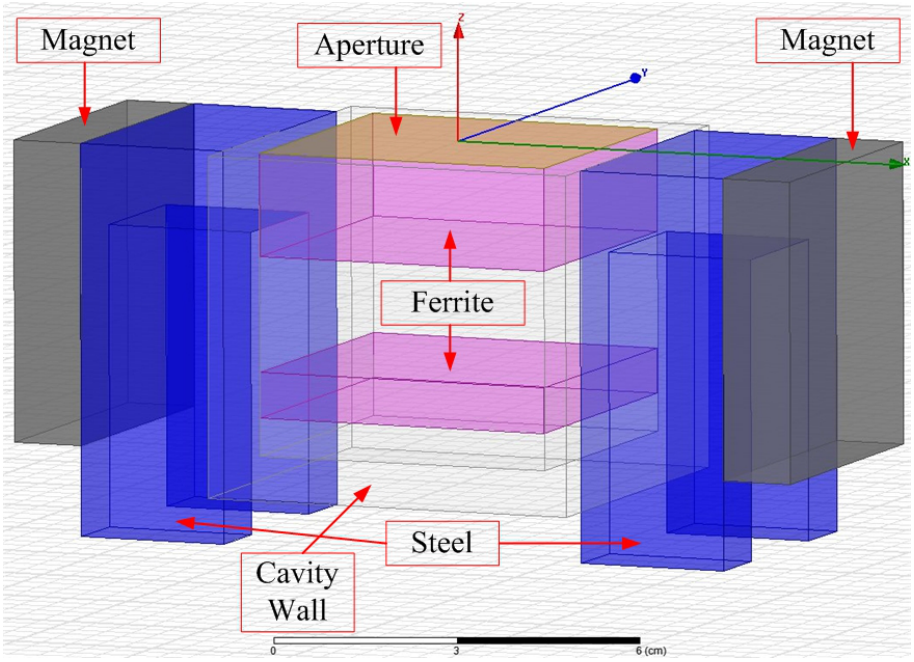

Figure 7.5: Computer-aided design in Ansys Maxwell 3D.

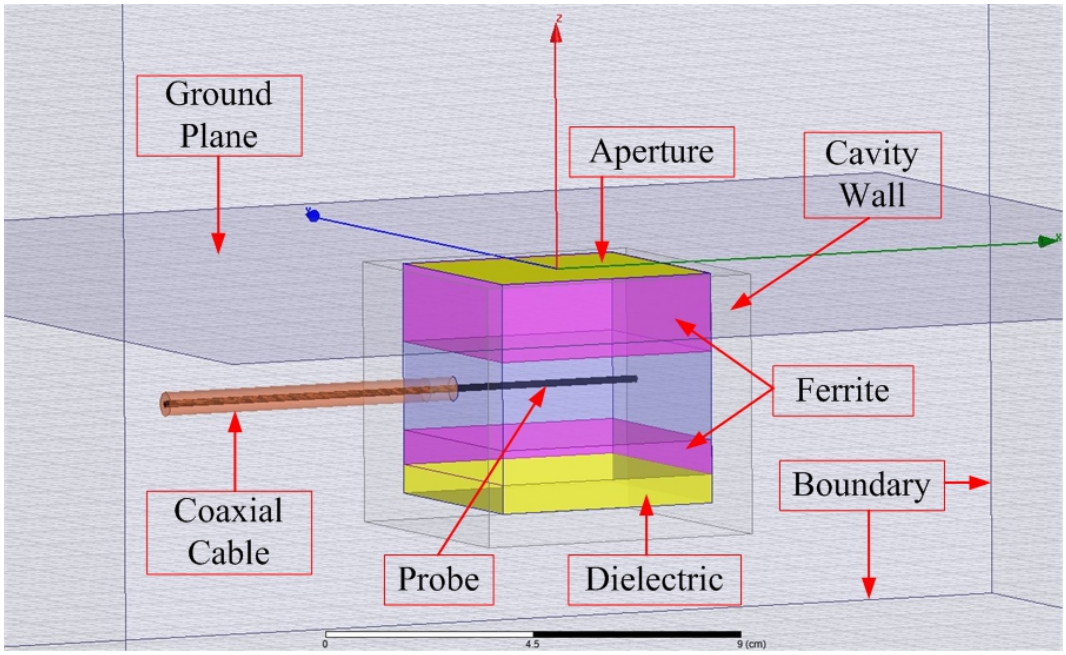

Figure 7.6: Computer-aided design in Ansys HFSS.

Figures 7.7a and 7.7b present the comparison between the measured and simulated input impedances for the weak and strong magnetization states, respectively. As can be seen, the blue and red curves, corresponding to Approaches 1 and 3, respectively, are in good agreement with measurements, black curve.

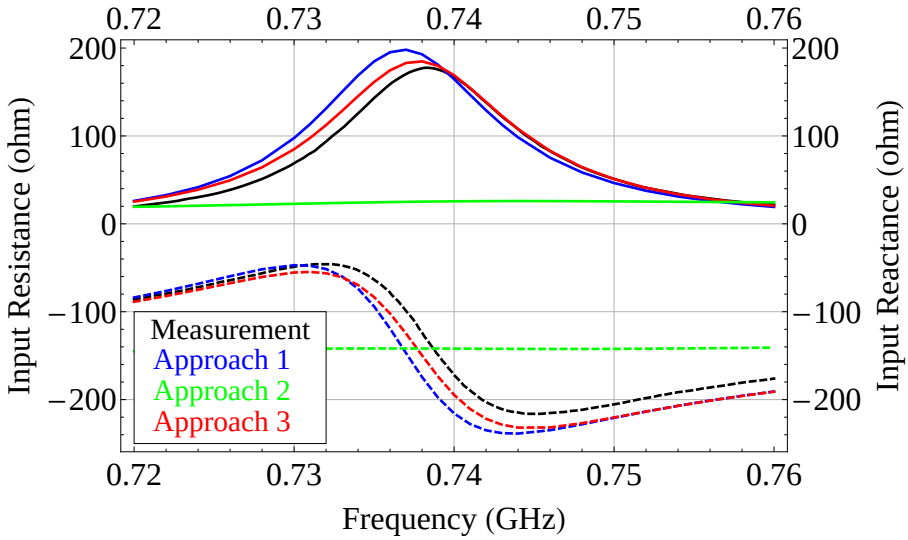

(a) Weak magnetization.

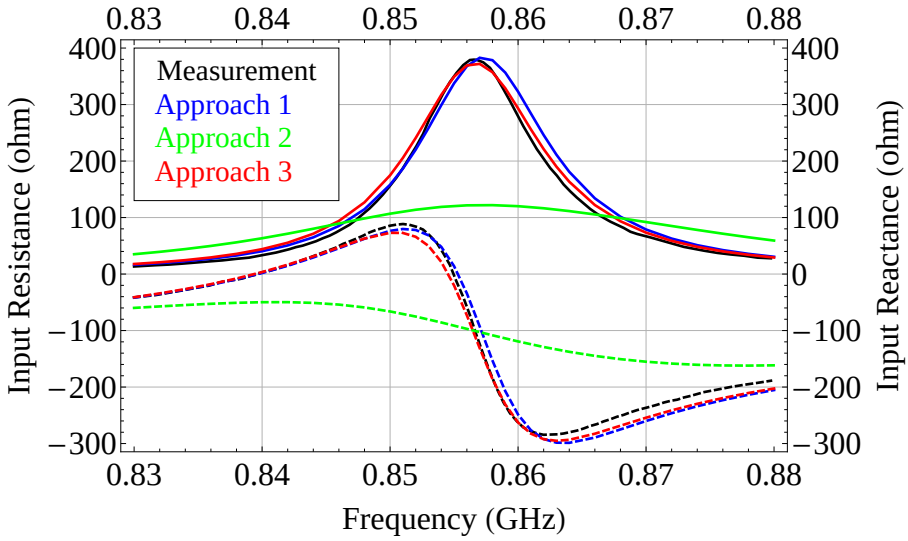

(b) Strong magnetization.

Figure 7.7: Real (solid) and imaginary (dashed) parts of the predicted and measured input impedance of the CBS antenna loaded with ferrite TTVG-800 as shown in Figure 7.4.

Rectangular Cavity.

The ferrite-loaded CBS antenna considered in this section is shown in Figure 7.8; this is the same antenna as in [14]. Narrow rectangular aluminum cavity, ($7.62 \times 1.27 \times 5.08$) cm, is loaded with two layers of the dielectric material and two layers of the ferrite material as shown in the figure. The electromagnet is used to bias the ferrite materials in the x-direction, perpendicular to the probe.

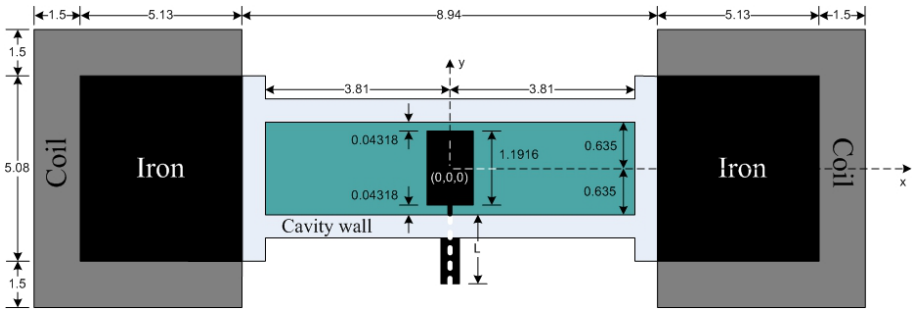

(a) Top view.

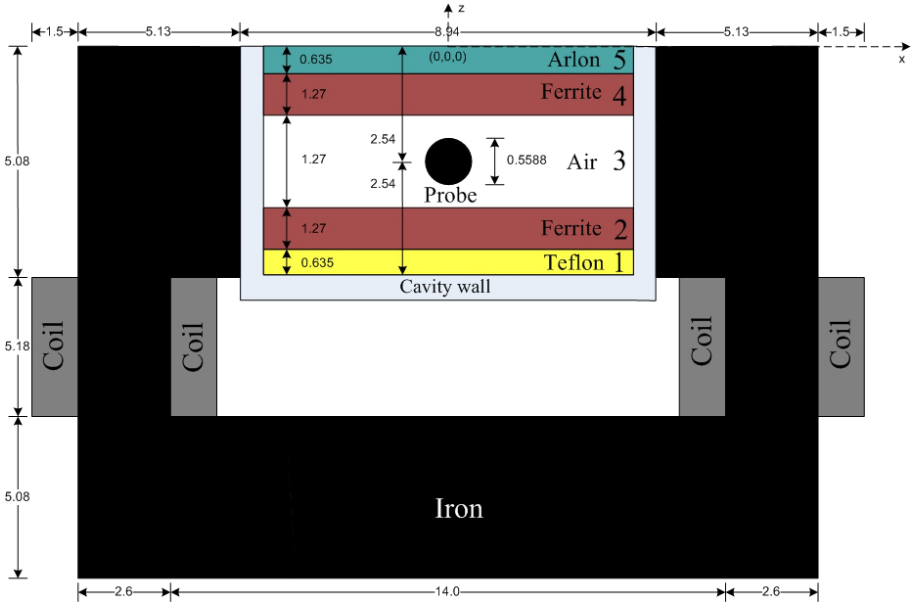

(b) Side view.

Figure 7.8: Rectangular cavity loaded with two layers of ferrite G-475 biased in the x-direction using the electromagnet in symmetric configuration.

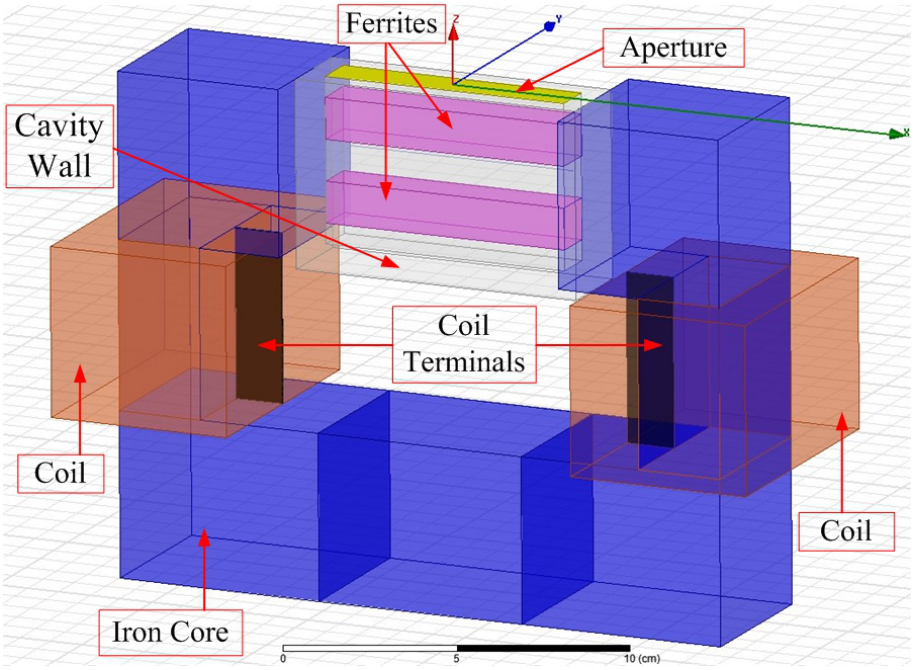

Figure 7.9: Computer-aided design in Ansys Maxwell 3D.

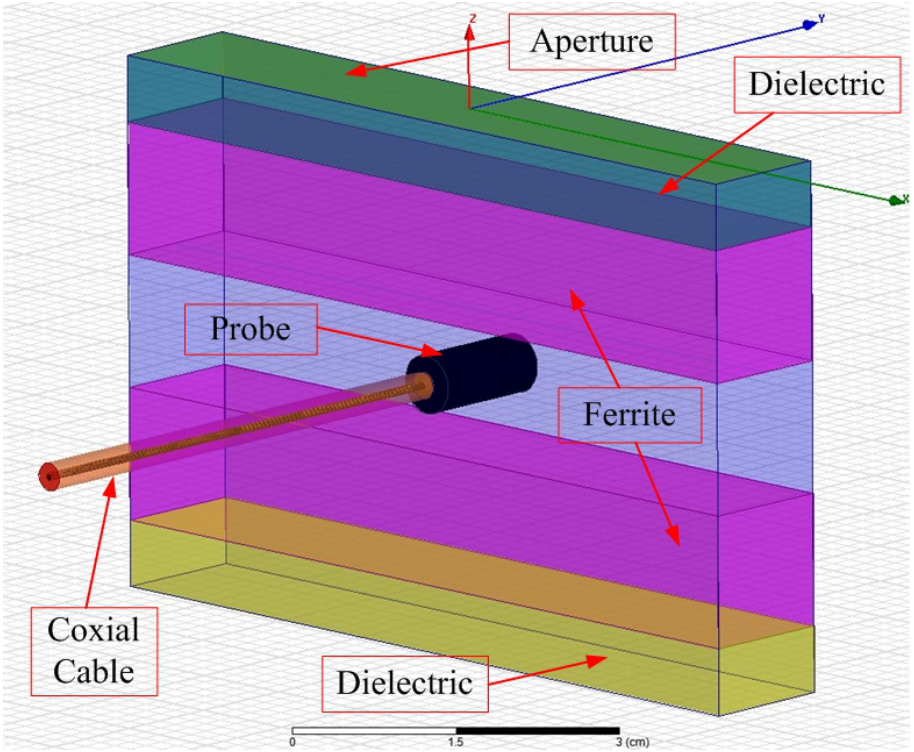

Figure 7.10: Computer-aided design in Ansys HFSS.

The non-linear magnetostatic problem in Approach 3 is solved using Ansys Maxwell 3D model shown in Figure 7.9. The iron core of the electromagnet is modeled as Steel-1008, non-linear material from the library of materials in Ansys Maxwell 3D. The coils are modeled as solid copper objects and the current excitation in the coil terminals is $Value = I \times N = 1.2 \times 850 = 1,020$. The ferrite material is G-475 with its initial magnetization curve approximated using (5.11). The internal magnetic field in Approach 1 is $H_x^i = 256$ (Oe), and the applied magnetic field in Approach 2 is $H_x^a = 310$ (Oe).

The RF simulations were performed using Ansys HFSS model shown in Figure 7.10. The probe is a 1.1916 cm long cylinder with the radius of 0.2794 cm. It is soldered to the inner conductor of the coaxial cable. The coax is modeled as a 50-Ω coaxial transmission line with Teflon ($\varepsilon_r = 2.0854$) inside, and the inner and outer radii of 0.04191 cm and 0.1397 cm, respectively. Parameters of the dielectric and ferrite materials used in the Ansys HFSS simulations are shown in Table 7.3.

Table 7.3: Material Parameters in Figure 7.8.

Material	#	Thickness	Parameters
Teflon	1	0.635	$\varepsilon_r = 2.2$
Ferrite: G-475	2	1.27	$\varepsilon_r = 13.3$, $g = 2.00$
	4	1.27	$4\pi Ms = 500$ G, $\Delta H = 40$ Oe
Air	3	1.27	$\varepsilon_r = 1$
Arlon	5	0.635	$\varepsilon_r = 9.8$

Measured and simulated input impedances are shown in Figure 7.11. The blue, green, and red curves correspond to Approaches 1, 2, and 3, respectively. As can be seen, the red curve is in excellent agreement with measurements. The other two simulations are not great, but they are not that bad either; comparing to the simulations in Sections 7.4 and 7.5, their agreement with measurements can be considered satisfactory.

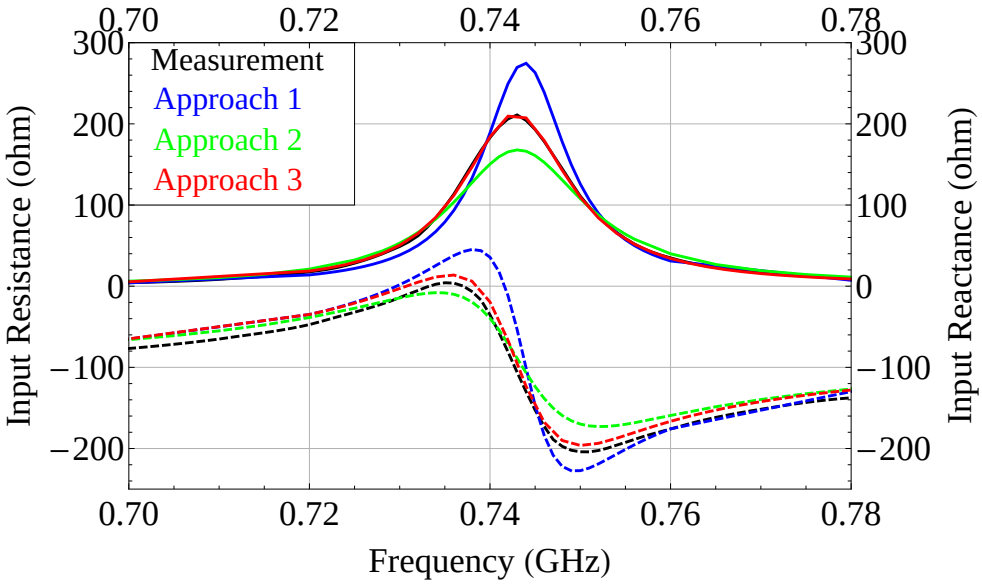

Figure 7.11: Real (solid) and imaginary (dashed) parts of the predicted and measured input impedance of the CBS antenna loaded with ferrite G-475 as shown in Figure 7.8.

7.3 Ferrite-Loaded CBS Antennas with Symmetric X-Biasing.

This section presents simulations and measurements of the input impedance and radiation patterns of the rectangular CBS antenna loaded with one layer of the ferrite material as shown in Figure 7.1. The ferrite is biased along its longest dimension (x-dimension) using permanent magnets or an electromagnet. The magnets are placed symmetrically about the yz-plane. This biasing configuration is referred to as the *symmetric x-biasing configuration*. The dominant component of the applied magnetic field generated by such biasing is H_x^a.

In the previous section, Approach 3 was tested against some of the simulations from the previous studies and was found to provide results of similar or better accuracy. The simulations and measurements in this section present further evaluation of Approach 3 and comparison of its performance with Approaches 1 and 2. The designs presented here can be treated using either of the three approaches with sufficient accuracy. The purpose of the section is to confirm that Approach 3 can ensure predictions which are at least as accurate as the predictions based on the other two approaches.

This section consists of three sub-sections presenting comparison of the simulations and measurements for three designs with different biasing configurations, plus one sub-section presenting the discussion of the results.

- Symmetric x-biasing using two permanent magnets. Ferrite G-475.
- Symmetric x-biasing using four permanent magnets. Ferrite G-475.
- Symmetric x-biasing using electromagnet.
  - Ferrite G-475

  - Ferrite G-1006
  - Ferrite TT2-113

- Discussion.

Symmetric placement of the magnets suggests that the distribution of the magnitude of the applied magnetic field should also be symmetric about the yz-plane. In general, however, this is not true because the magnets on the opposite sides of the symmetry plane are not necessarily identical This will most likely lead to asymmetric distribution of the total applied magnetic field and, consequently, asymmetric internal magnetic field. The computer-aided designs used to simulate the internal magnetic field are presented and discussed for each design individually.

Symmetric X-Biasing Using Two Permanent Magnets.

The dimensions of the geometry and the biasing configuration are shown in Figure 7.12. The ferrite material is biased by two permanent magnets placed symmetrically about the yz-plane; one magnet is placed next to the left wall of the cavity, $x = -4.47$ cm, and the other one next to the right (opposite) wall, $x = 4.47$ cm, as shown in the figure.

Figure 7.13 shows the computer-aided design in Ansys Maxwell 3D. The ferrite material used in this design is G-475. The initial magnetization curve of this ferrite is approximated using (5.11). The permanent magnets are modeled as NdFe35 with the non-uniform coercivity H_c; each permanent magnet is divided into three parts with coercivities $H_{c(T)}$, $H_{c(M)}$, and $H_{c(B)}$ as shown in Figure 7.13. The numerical values of these coercivities are given in Table 7.4. Such non-uniform modeling is necessary to properly represent the asymmetry of the applied field.

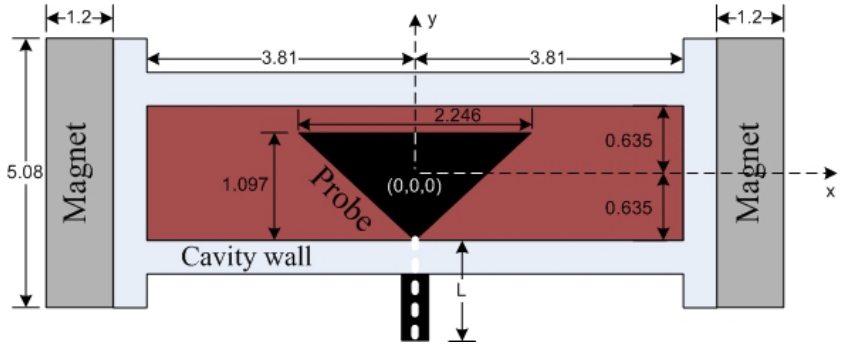

(a) Top view

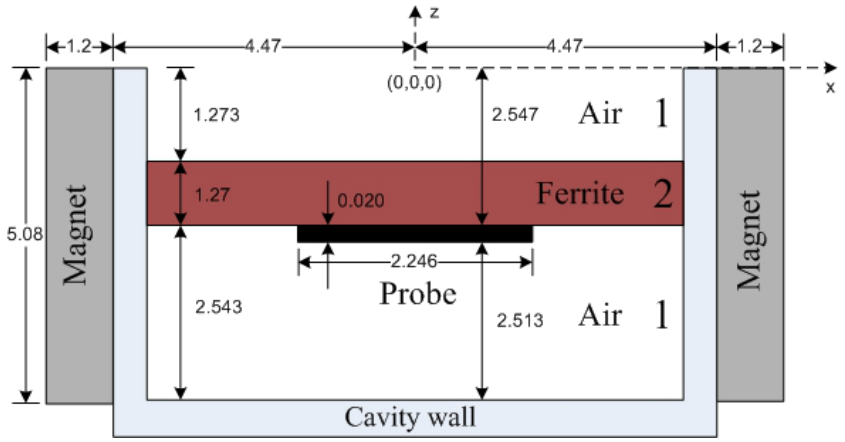

(b) Side view

Figure 7.12: Rectangular cavity loaded with one layer of ferrite material biased in the x-direction using permanent magnets in symmetric configuration (units of length: cm).

Table 7.4: Coercivity H_c of the Permanent Magnets in Figure 7.13.

Magnet	$H_{c(T)}$ (kA/m)	$H_{c(M)}$ (kA/m)	$H_{c(B)}$ (kA/m)
Left ($x = -4.47$) cm	-1030	-790	-890
Right ($x = 4.47$) cm	-1190	-950	-890

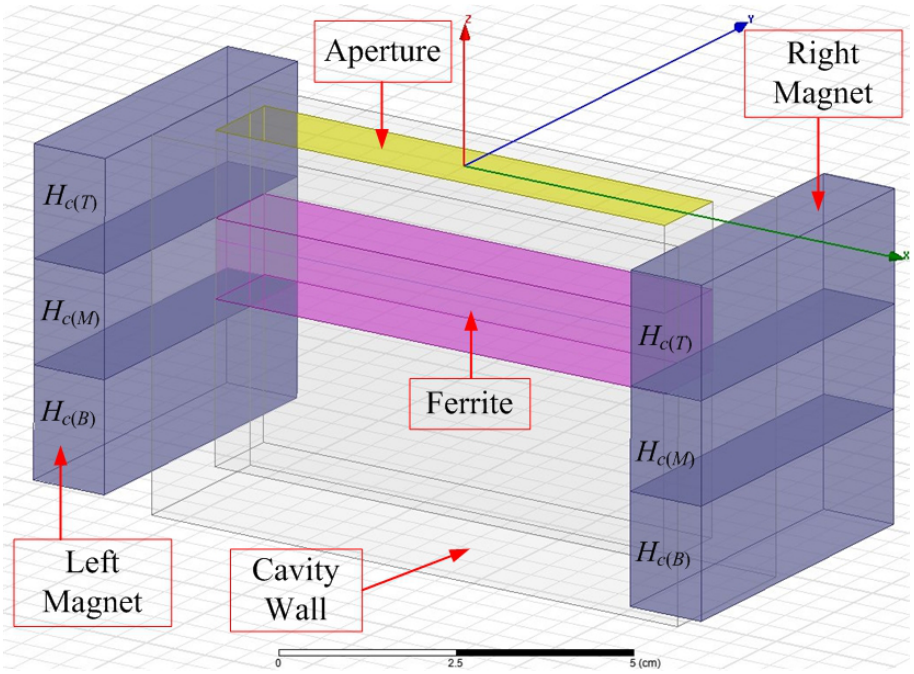

Figure 7.13: Computer-aided design in Ansys Maxwell 3D.

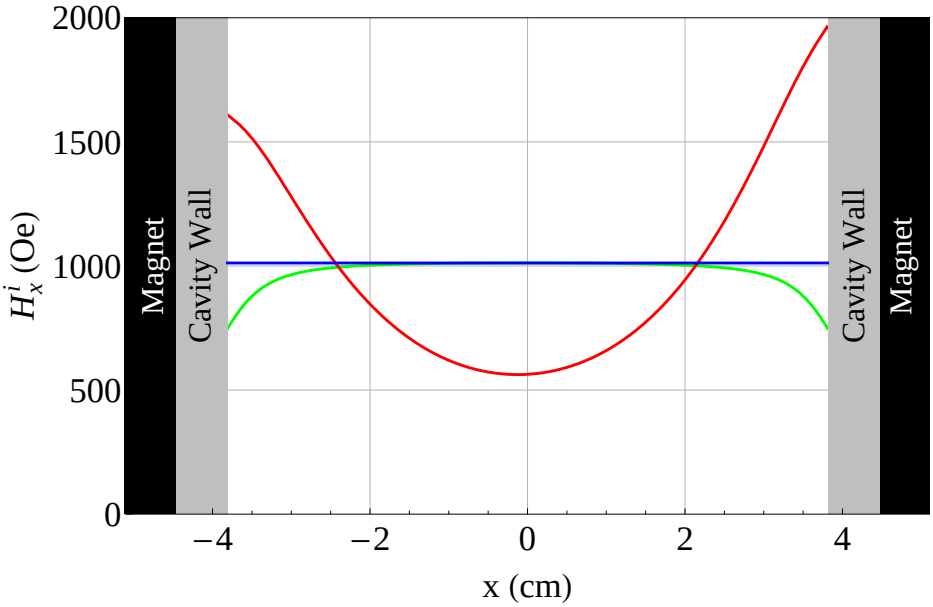

Figure 7.14: H_x^i component of the magnetic field inside the ferrite material along the ferrite center-line $(x, 0, -1.912)$ cm.

The walls of the cavity are made of aluminum with permeability $\mu_r \simeq 1.0$; therefore, they are transparent to the static magnetic field and play no role in the computation of the internal magnetic field. Their modeling is unnecessary and they are shown in Figure 7.13 only for the demonstration purposes.

The magnetic field inside the ferrite material, $\vec{H}^i$, is computed using three approaches discussed in Chapter 4. The distributions of the H_x^i component are shown in Figure 7.14. These distributions are plotted along the center-line of the ferrite material (x, 0, -1.912) cm. The blue, green, and red curves represent distributions computed using Approaches 1, 2, and 3, respectively. The red curve in Figure 7.14 was obtained using Ansys Maxwell 3D model shown in Figure 7.13. As can be seen, the distribution is asymmetric due to the fact that the permanent magnets on the left and right sides of the cavity are not identical (see Table 7.4); the magnet on the right side is stronger. To obtain the green curve using Approach 2, the uniform applied field $H_x^a = 1,020$ (Oe) was used. This is the volumetric average of the applied magnetic field generated by the permanent magnets in the absence of any materials in the cavity. The average is taken over the volume which will be occupied by the ferrite material. The uniform blue distribution based on Approach 1 is computed as follows

$$H_x^i = H_x^a - N4\pi M_s = 1,020 - 0.0168 \times 500 = 1,012 \text{ Oe} \tag{7.1}$$

where the ballistic demagnetizing factor, $N = 0.0168$, was computed using (4.5).

As can be seen in Figure 7.14, the distribution based on Approach 1 is uniform and the distribution based on Approach 2 is somewhat non-uniform. Approach 3, on the other hand, predicts internal magnetic field which is significantly more non-uniform than the other two predictions. The reason for such different predictions is the non-uniform applied magnetic field. Approaches 1 and 2 ignore non-uniformities of this field by averaging them. Since Approach 3 does not involve such averaging,

the predictions based on this approach are considered to be more representative of the true internal magnetic field.

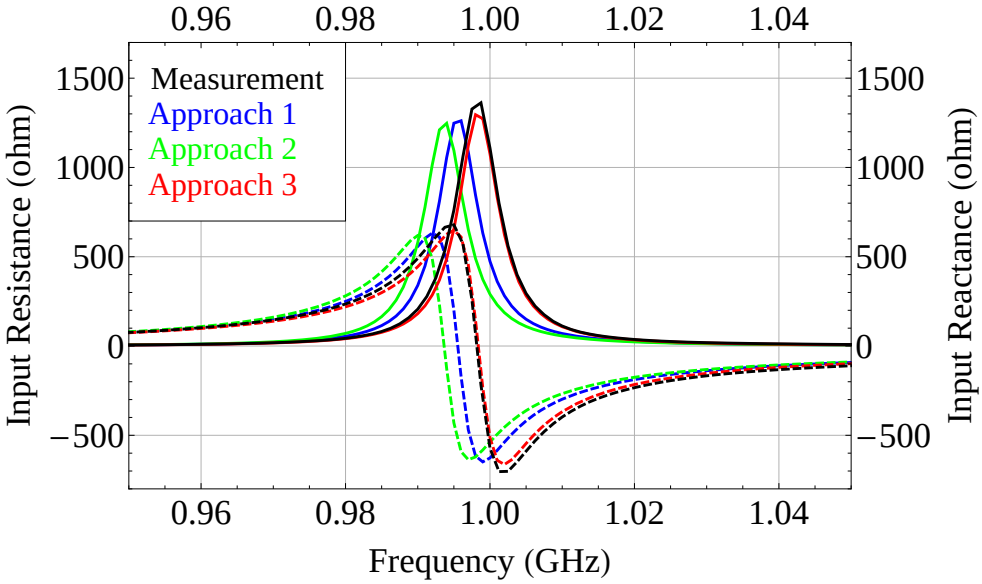

Figure 7.15: Real (solid) and imaginary (dashed) parts of the predicted and measured input impedance of the CBS antenna loaded with ferrite G-475 as shown in Figure 7.12. The three simulations correspond to the three internal field distributions in Figure 7.14.

Table 7.5: Material Parameters in Figure 7.12

Material	#	Thickness	Parameters
Air (top)	1	1.273	$\varepsilon_r = 1$
Air (bottom)	1	2.543	$\varepsilon_r = 1$
Ferrite: G-475	2	1.27	$\varepsilon_r = 13.20$, $g = 2.01$ $4\pi Ms = 475$ G, $\Delta H = 40$ Oe

Using the internal field distributions in Figure 7.14 and the material parameters in Table 7.5, the input impedance and radiation patterns were simulated using the Ansys HFSS model shown in Figure 7.1. Measurements and simulations of the input impedance are shown in Figure 7.15. Figure 7.16 shows the E- and H-plane radiation patterns measured and simulated at $f = 1.0$ GHz. The color coding of these figures is the same as in Figure 7.14; the red input impedance and radiation

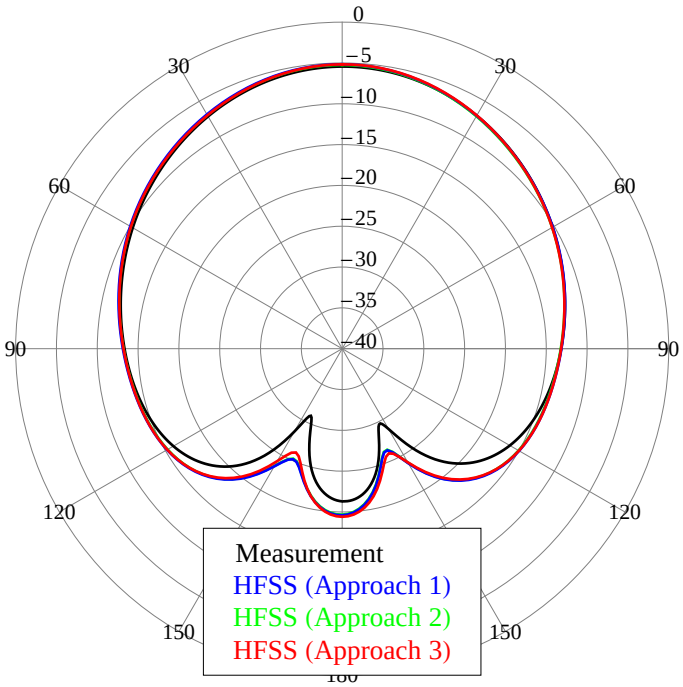

(a) E-plane.

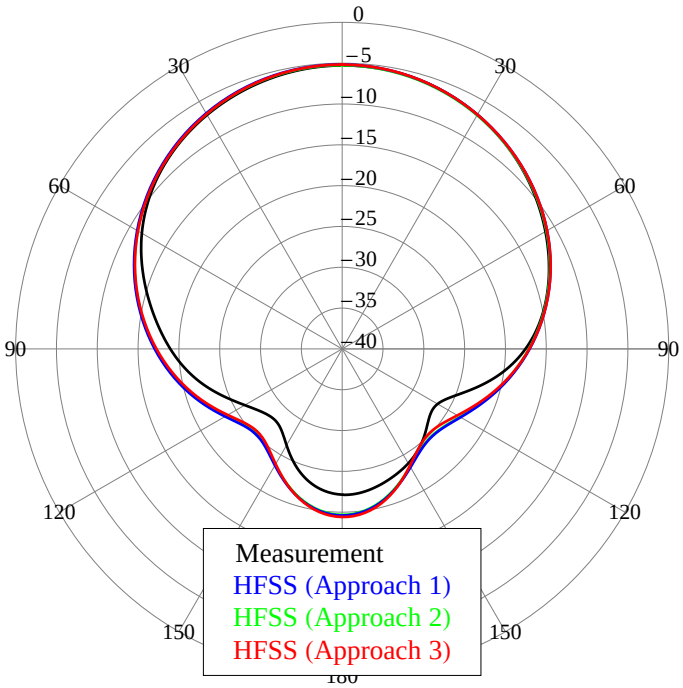

(b) H-plane.

Figure 7.16: E- and H-plane radiation patterns.

patterns were simulated using the red internal field distribution. These figures clearly show that the three approaches yield results of similar accuracy despite the fact that the internal field distributions are quite different. The input impedance predictions based on Approach 1 and 2 have approximately the same peak amplitude, but deviate from the measured resonant frequency by about 5-10 MHz, which constitutes a negligible $0.5 - 1$ percent error at $f = 1.0$ GHz. The predictions and measurements of the radiation patterns are also in very good agreement with each other, especially above the ground plane.

Symmetric X-Biasing Using Four Permanent Magnets.

Figure 7.17 shows the geometry and the biasing configuration which are essentially the same as in the previous sub-section. The difference of this design from the one in Figure 7.12 is the stronger applied magnetic field, which is achieved by using four permanent magnets instead of two. As can be seen in the figure, two stacked permanent magnets are placed on each side of the cavity, as opposed to only one in the previous design.

The computer-aided design in Ansys Maxwell 3D is shown in Figure 7.18. As before, the ferrite is G-475 with the initial magnetization curve approximated by (5.11). The permanent magnets are NdFe35 with the non-uniform coercivity of each magnet divided into three parts, $H_{c(T)}$, $H_{c(M)}$, and $H_{c(B)}$ as shown in the figure. The numerical values of these coercivities are given in Table 7.6.

The distributions of the H_x^i component along the center-line of the ferrite material, (x, 0, -1.912) cm, are shown in Figure 7.19. The blue, green, and red curves represent distributions computed using Approaches 1, 2, and 3, respectively. These distributions are very similar to the distributions in Figure 7.14, but they

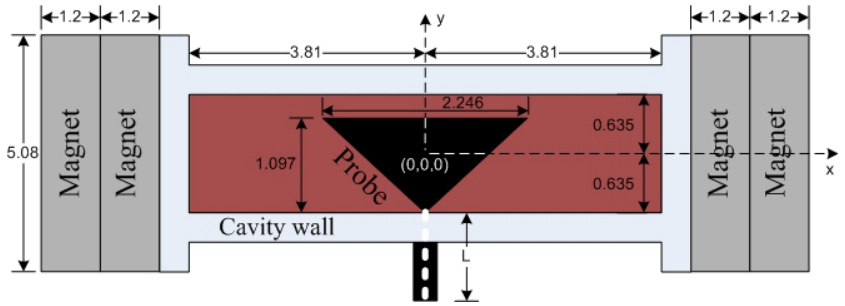

(a) Top view

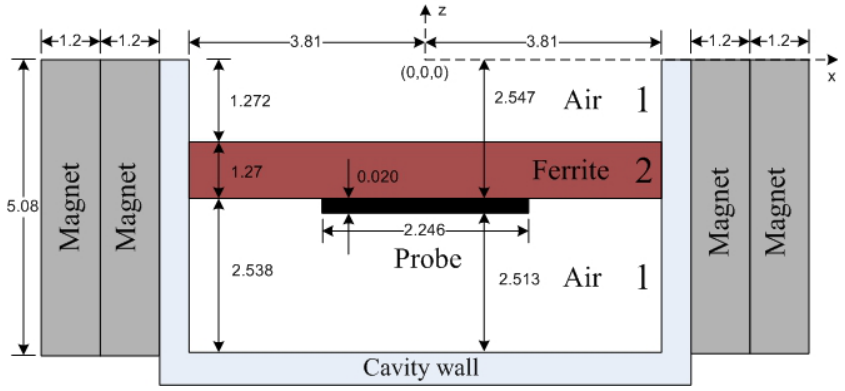

(b) Side view

Figure 7.17: Rectangular cavity loaded with one layers of ferrite material biased in the x-direction using permanent magnets in symmetric configuration (units of length: cm).

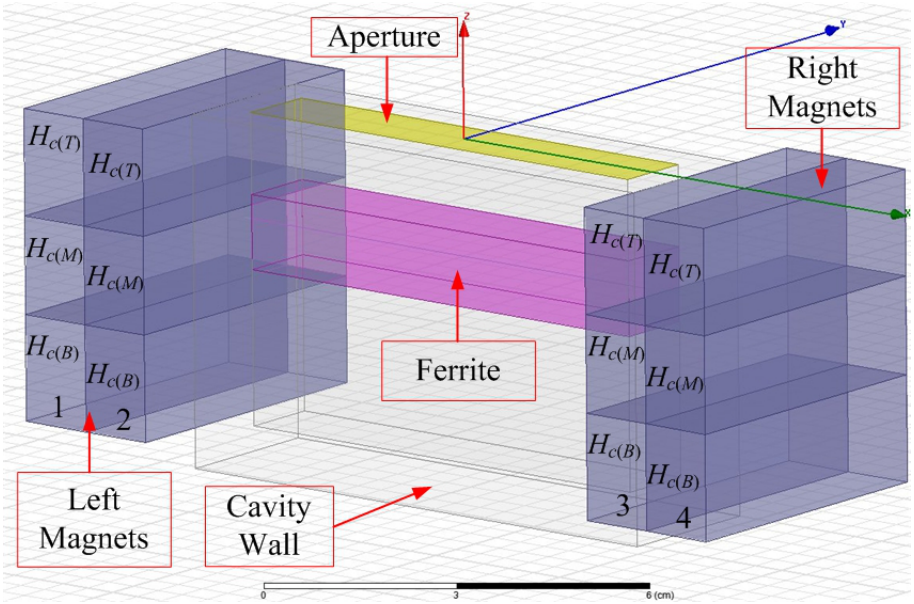

Figure 7.18: Computer-aided design in Ansys Maxwell 3D.

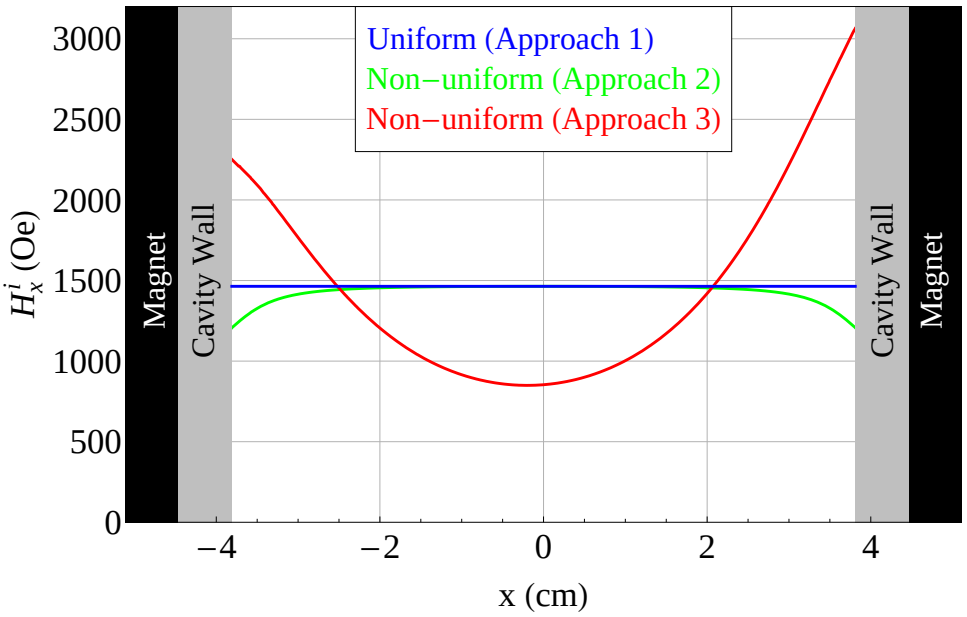

Figure 7.19: H_x^i component of the magnetic field inside the ferrite material along the ferrite center-line $(x, 0, -1.912)$ cm.

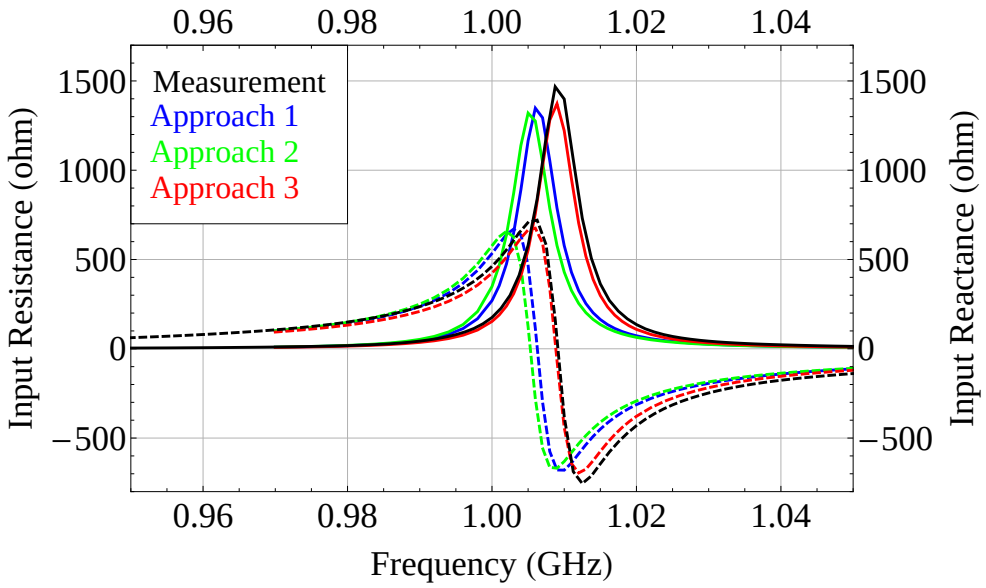

Figure 7.20: Real (solid) and imaginary (dashed) parts of the predicted and measured input impedance of the CBS antenna loaded with ferrite G-475 as shown in Figure 7.17. The three simulations correspond to the three internal field distributions in Figure 7.19.

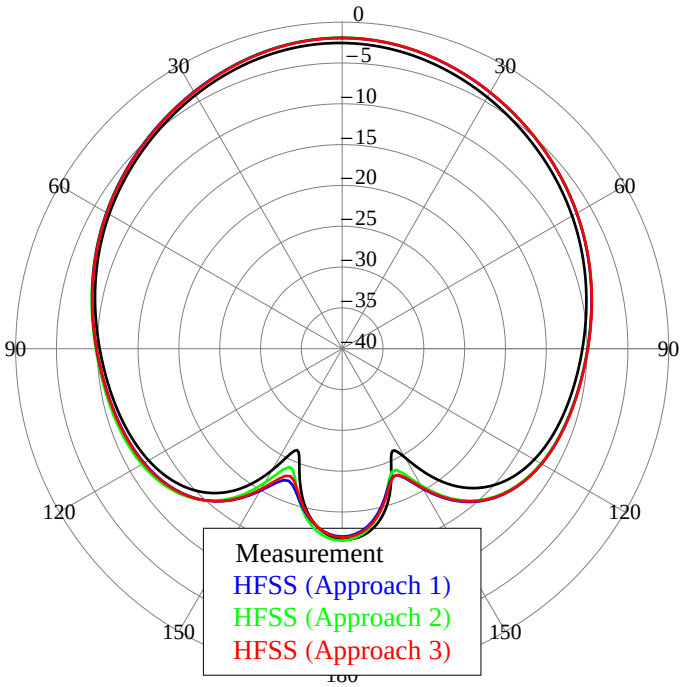

(a) E-plane

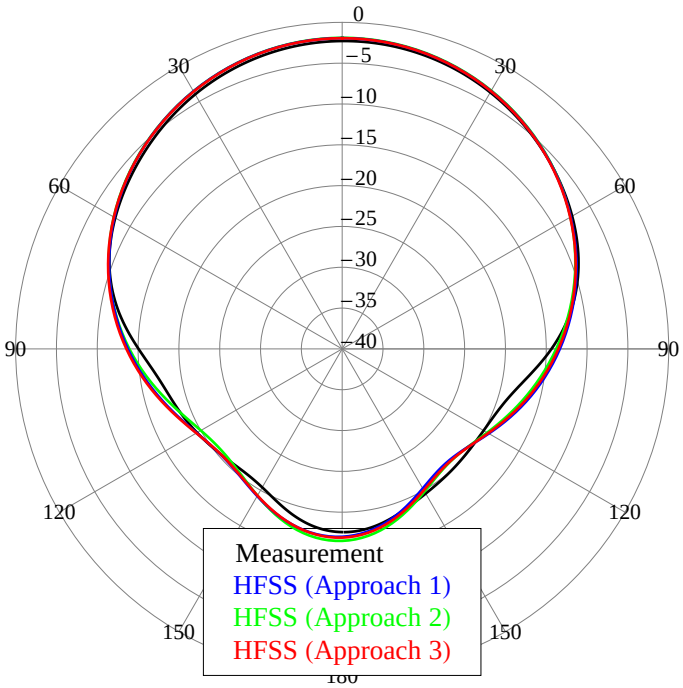

(b) H-plane

Figure 7.21: E- and H-plane radiation patterns.

Table 7.6: Coercivity H_c of the Permanent Magnets in Figure 7.18.

Magnet #	$H_{c(T)}$ (kA/m)	$H_{c(M)}$ (kA/m)	$H_{c(B)}$ (kA/m)
1, Left ($x = -5.67$) cm	-1000	-585	-870
2, Left ($x = -4.47$) cm	-1000	-585	-870
3, Right ($x = 4.47$) cm	-1160	-890	-870
4, Right ($x = 5.67$) cm	-1160	-890	-870

exhibit stronger internal fields, which is the consequence of the stronger applied magnetic field. The red curve was simulated using Ansys Maxwell 3D model shown in Figure 7.18. To obtain the green curve using Approach 2, the uniform applied field $H_x^a = 1,472$ (Oe) was used. (This is the volumetric average of the applied magnetic field generated by the permanent magnets in the absence of any materials in the cavity.) The uniform blue distribution based on Approach 1 is computed as follows

$$H_x^i = H_x^a - N4\pi M_s = 1,472 - 0.0168 \times 500 \simeq 1,464 \text{ Oe} \tag{7.2}$$

Parameters of the ferrite material used in the Ansys HFSS simulations are given in Table 7.18. Simulations and measurements of the input impedance and the radiation patterns are compared in Figure 7.20 and Figure 7.21, respectively. The patterns are shown at frequency $f = 1.01$ GHz. These results are very similar to the results of the previous section, Figures 7.15 and 7.16. All three approaches provided very accurate predictions. The resonant frequency predicted by Approaches 1 and 2 is off by $\simeq 5$ MHz, which corresponds to 0.5% error at $f = 1.01$ GHz and can be considered negligible.

Table 7.7: Material Parameters in Figure 7.17

Material	#	Thickness	Parameters
Air (top)	1	1.272	$\varepsilon_r = 1$
Air (bottom)	1	2.538	$\varepsilon_r = 1$
Ferrite: G-475	2	1.27	$\varepsilon_r = 13.23$, $g = 2.01$ $4\pi M_s = 475$ G, $\Delta H = 40$ Oe

Symmetric X-Biasing Using Electromagnet.

The design presented in this section utilizes an electromagnet to bias the ferrite material. The geometry and the biasing configuration are shown in Figure 7.22. The electromagnet is symmetric with respect to the yz-plane; its south and north poles are at $x = -4.47$ cm and $x = 4.47$ cm, respectively. When the current in the two coils of such an electromagnet is the same, the magnitude distribution of the generated applied magnetic field is also symmetric about the yz-plane. The biasing of the ferrite material is achieved by placing the cavity between the poles of the electromagnet as shown in Figure 7.22.

The computer-aided design in Ansys Maxwell 3D is shown in Figure 7.23. The iron core of the electromagnet is modeled as a non-linear material Steel-1008 from the Ansys Maxwell 3D library of materials. The coils are modeled as solid copper objects. The current in the coils is $I = 1.47$ amp. Thus, the current excitation in the coil terminals is

$$Value = I \times N = 1.47 \times 850 \simeq 1,250 \tag{7.3}$$

This biasing configuration was tested with three ferrite materials: G-475, G-1006, and TT2-113. Their initial magnetization curves are approximated using (5.11) with the corresponding values of the adjustable parameter, H_1, given in Table 5.2.

Typical distributions of the H_x^i component of the internal magnetic field obtained using the three approaches discussed in Chapter 4 are shown in Figure 7.24. These particular distributions are for the magnetic field inside the G-475 ferrite. The distributions are plotted along the center-line of the ferrite material, (x, 0, -1.912) cm. The blue, green, and red curves represent Approaches 1, 2, and 3, respectively. Similar distributions were obtained for the ferrites G-1006 and TT2-113.

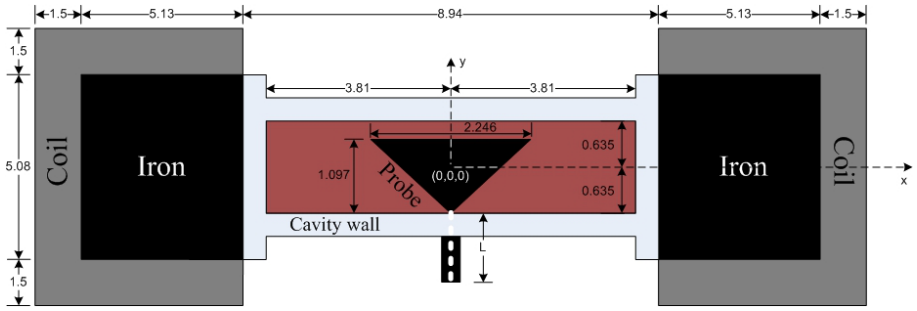

(a) Top view

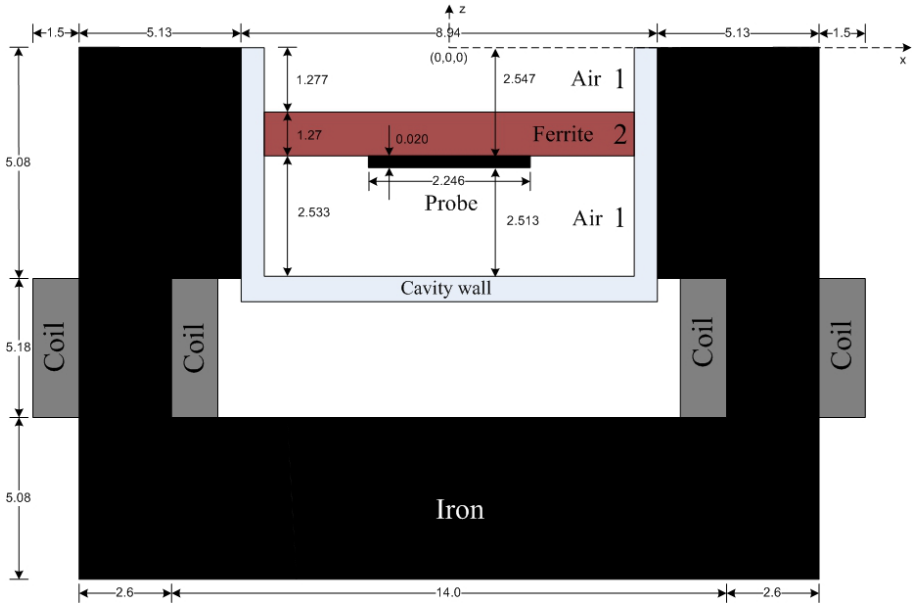

(b) Side view

Figure 7.22: Rectangular cavity loaded with one layers of ferrite material biased in the x-direction using electromagnet in symmetric configuration (units of length: cm).

The red curve was simulated using Ansys Maxwell 3D model shown in Figure 7.23. To obtain the green curve using Approach 2, the uniform applied field, H_x^a, for the three ferrite materials is given in Table 7.8. This table also includes the uniform internal magnetic field, H_x^i, in Approach 1, blue curve. It is important to notice that the non-uniformities of the internal field distributions are not very severe, which implies that it may be possible to average these distributions and still expect sufficient accuracy in the RF simulations.

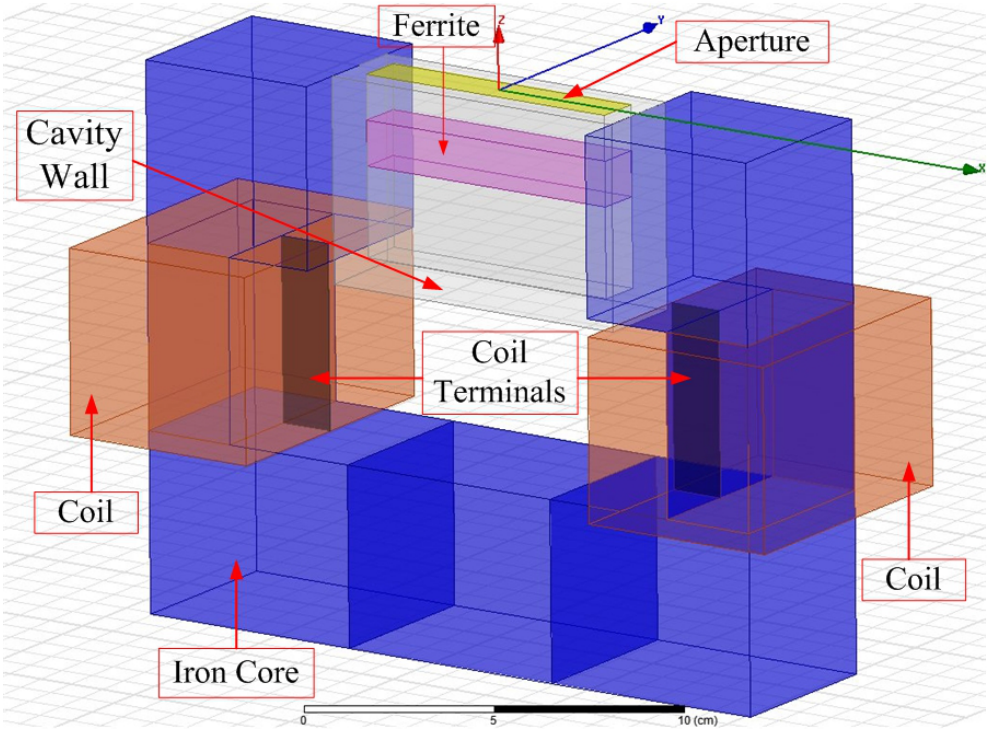

Figure 7.23: Computer-aided design in Ansys Maxwell 3D.

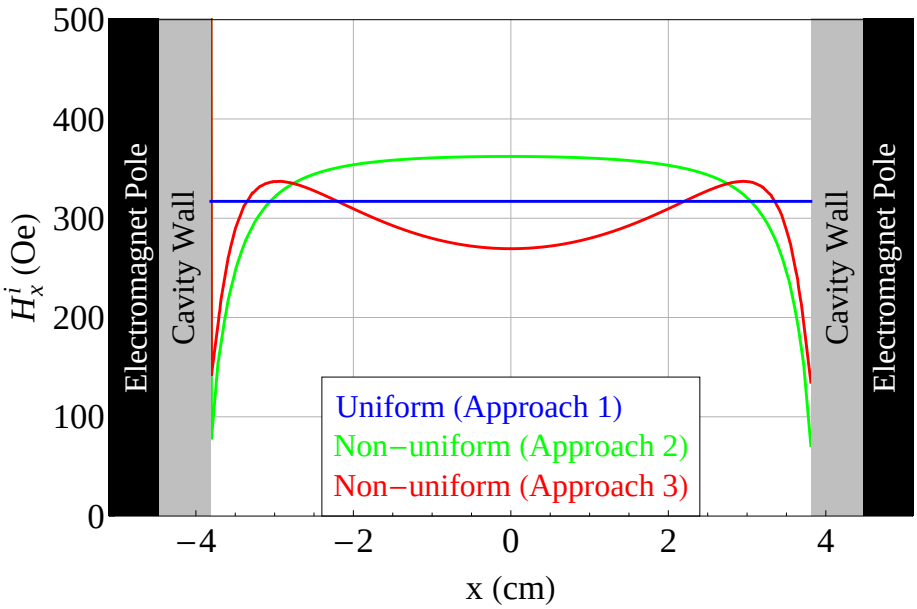

Figure 7.24: H_x^i component of the magnetic field inside the G-475 ferrite material along the ferrite center-line $(x, 0, -1.912)$ cm.

Table 7.8: Internal Field for Approach 1 and Applied Field for Approach 2.

Magnetic field	G-475	G-1006	TT2-113
Approach 1, H_x^i (Oe)	317	321	318
Approach 2, H_x^a (Oe)	370	360	350

Table 7.9: Material Parameters in Figure 7.22.

Material	#	Thickness	Parameters
Air (top)	1	1.277	$\varepsilon_r = 1$
Air (bottom)	1	2.533	$\varepsilon_r = 1$
Ferrite: G-475	2	1.27	$\varepsilon_r = 13.35$, $g = 2.01$ $4\pi Ms = 500$ G, $\Delta H = 48$ Oe
Ferrite: G-1006	2	1.27	$\varepsilon_r = 13.5$, $g = 2.01$ $4\pi Ms = 400$ G, $\Delta H = 78$ Oe
Ferrite: TT2-113	2	1.27	$\varepsilon_r = 8.2$, $g = 1.54$ $4\pi Ms = 550$ G, $\Delta H = 100$ Oe

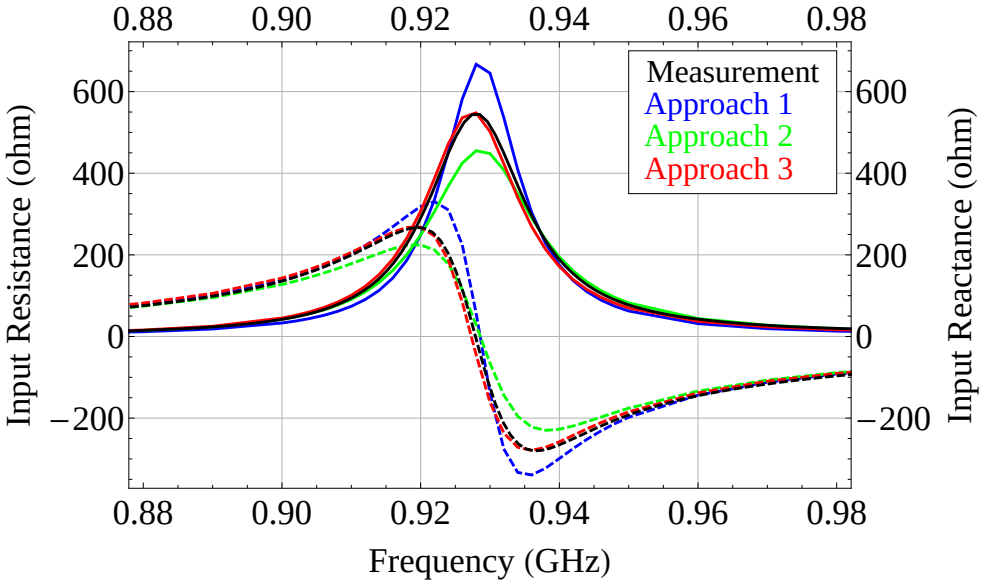

Figure 7.25: Real (solid) and imaginary (dashed) parts of the predicted and measured input impedance of the CBS antenna loaded with ferrite G-475 as shown in Figure 7.22.

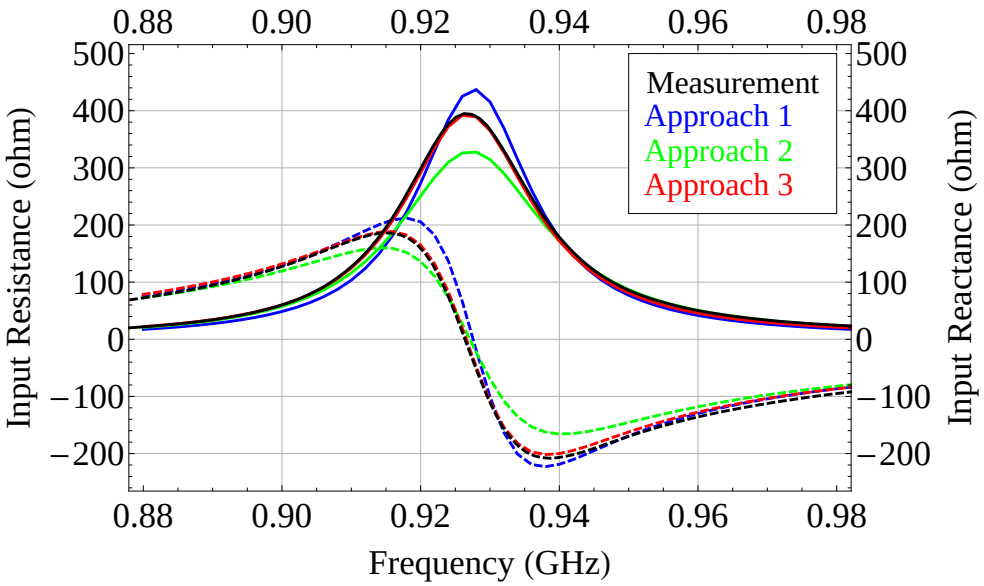

Figure 7.26: Real (solid) and imaginary (dashed) parts of the predicted and measured input impedance of the CBS antenna loaded with ferrite G-1006 as shown in Figure 7.22.

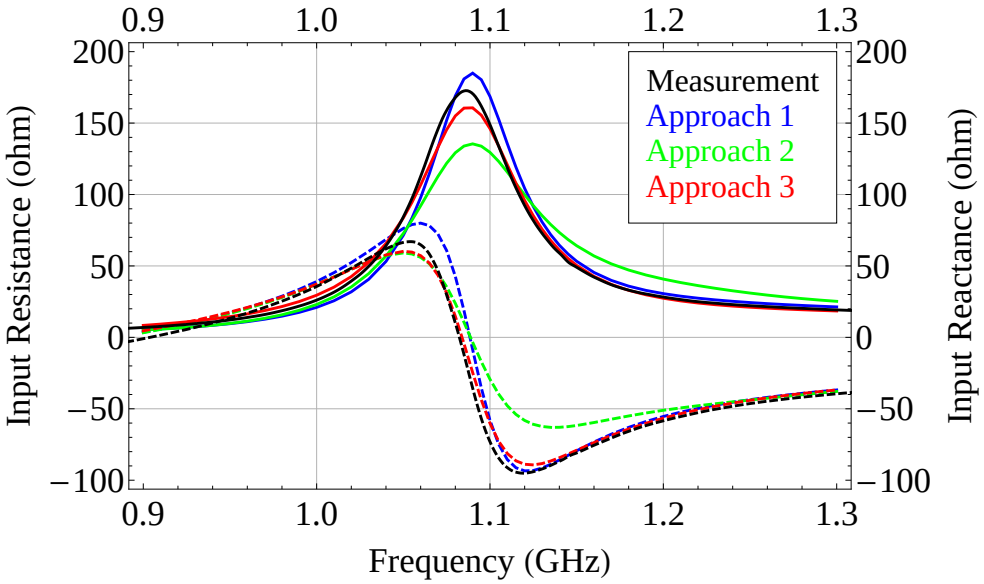

Figure 7.27: Real (solid) and imaginary (dashed) parts of the predicted and measured input impedance of the CBS antenna loaded with ferrite TT2-113 as shown in Figure 7.22.

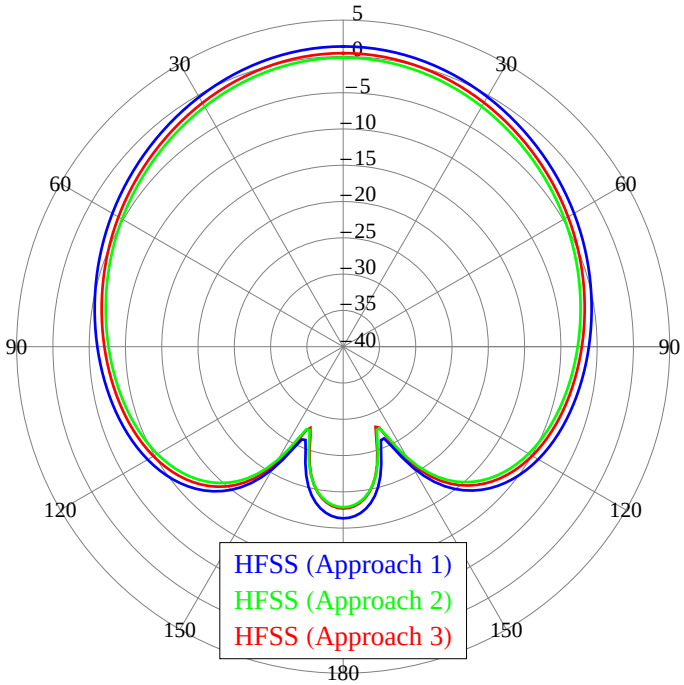

(a) E-plane

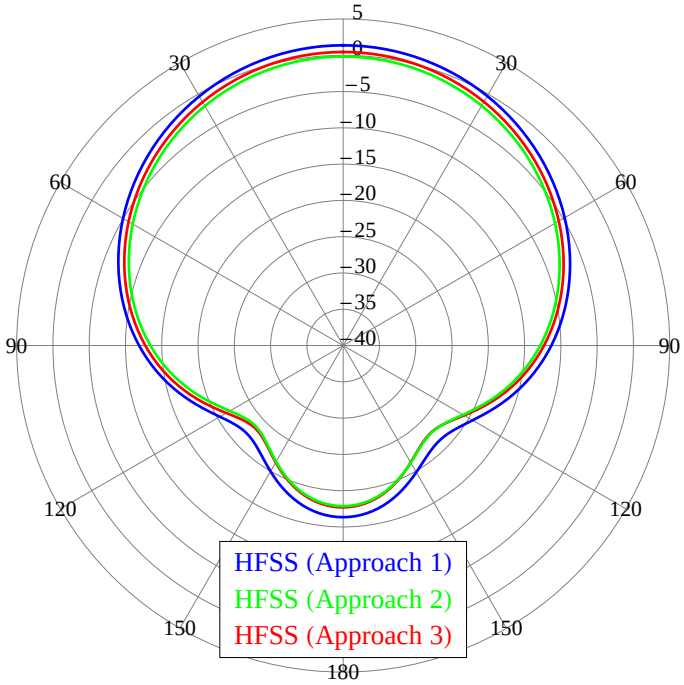

(b) H-plane

Figure 7.28: E- and H-plane radiation patterns.

Material parameters for the simulations of the input impedance and radiation patterns in Ansys HFSS are given in Table 7.9. The simulations and measurements of the input impedance when the cavity is loaded with one of the ferrites G-475, G-1006, or TT2-113 are shown in Figures 7.25, 7.26, and 7.27, respectively. Simulations of the radiation patterns at $f = 1.0$ GHz for the CBS antenna loaded with one layer of the G-475 ferrite are shown in Figure 7.28. It is clear from these figures that the simulations based on Approach 3 are in excellent agreement with measurements. Predictions based on the other two approaches exhibit lower accuracy but are not too bad overall. The most noticeable mismatch is the predicted peak amplitude of the real part of the input impedance curves; it is overestimated in Approach 1 and underestimated in Approach 2. The simulations of the radiation patterns are very similar showing that the performance of all three approaches is on par with each other.

Discussion.

Designs resented in this section utilize permanent magnets or an electromagnet in symmetric configuration to bias the ferrite material in the x-direction. For each design, three approaches were used to determine the magnetic field distribution inside the ferrite material. These distributions were then used in Ansys HFSS to obtain three simulations of the input impedance and radiation patterns.

Simulations in Figures 7.14 and 7.19 show that the internal magnetic field computed using Approach 3 differs significantly from the internal fields computed using Approaches 1 and 2. The red curve exhibits very non-uniform distribution as opposed to the uniform and nearly uniform blue and green distributions. However, as can be seen in Figures 7.15 and 7.20, simulations of the input impedance and radiation patterns are relatively insensitive to such obvious difference between the

computed internal fields. This observation suggests that the use of the more complex Approach 3 to compute the non-uniform internal magnetic field was unnecessary because sufficiently accurate predictions could be obtained using a simpler method based on the uniform Approach 1. This observation does not diminish the importance of Approach 3 and its ability to ensure accurate predictions, it simply indicates that in a certain limit Approach 3 converges to Approach 1. This limit can be attributed to the intensity of the internal magnetic field. Distributions in Figures 7.14 and 7.19 exhibit very strong magnetic fields inside the ferrite material. These fields are sufficiently strong to uniformly magnetized the ferrite to its saturation. In such a saturated state, ferrites exhibit low absorption losses which is also supported by the very sharp input impedance curves in Figures 7.15 and 7.20.

Another way to look at it is to examine what happens to the components of the permeability tensor as the intensity of the internal magnetic field approaches infinity. The components of the tensor (3.2) are represented by μ and κ which can be separated into real and imaginary parts [9]. These quantities have the following limits at infinity

$$\lim_{H^i \to \infty} (\mu' + j\mu'') = 1 + j0 \tag{7.4}$$

$$\lim_{H^i \to \infty} (\kappa' + j\kappa'') = 0 + j0 \tag{7.5}$$

Thus, as the internal field approaches infinity, the permeability tensor approaches unity, which implies that the magnetic properties of the ferrite material become less obvious and the magnetic resonance disappears. When the internal magnetic field is very strong, the ferrite acts as a dielectric material due to its remaining greater than unity permittivity. To support this argument, Figure 7.29 shows the distributions of the real and imaginary parts of the tensor component $\mu = \mu' + j\mu''$ along the center-line of the ferrite G-475 when it is biased by the symmetric configuration of four permanent magnets shown in Figure 7.17. The blue, green, and red distributions

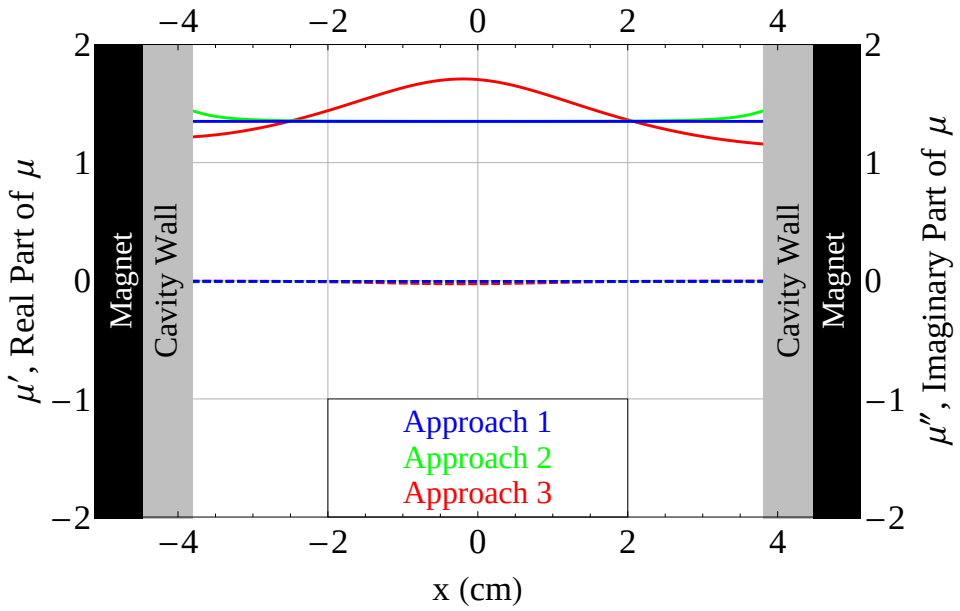

Figure 7.29: Real (solid) and imaginary (dashed) parts of the tensor component $\mu = \mu' + j\mu''$ along the center-line of the ferrite G-475 biased by four permanent magnets as shown in Figure 7.17.

represent the three approaches. As can be seen, the imaginary parts are zero and the real parts are in the vicinity of 1, which is in agreement with (7.4). The three distributions are not very different from one another, hence the reason why the performance of the three approaches is on par with each other.

Simulations in Figures 7.25 - 7.27 also demonstrate relatively good agrement between the three approaches. However, the internal magnetic field is not as strong as in the simulations with permanent magnets; therefore, such a good agreement cannot be explained by the same reasoning as above. To explain it, it should be emphasized that as far as the RF simulations is concerned, the three different approaches to compute the internal magnetic field result in three different permeability tensors. Thus, if the three approaches yield similar permeability tensors, then the simulations of the input impedance will also yield similar results.

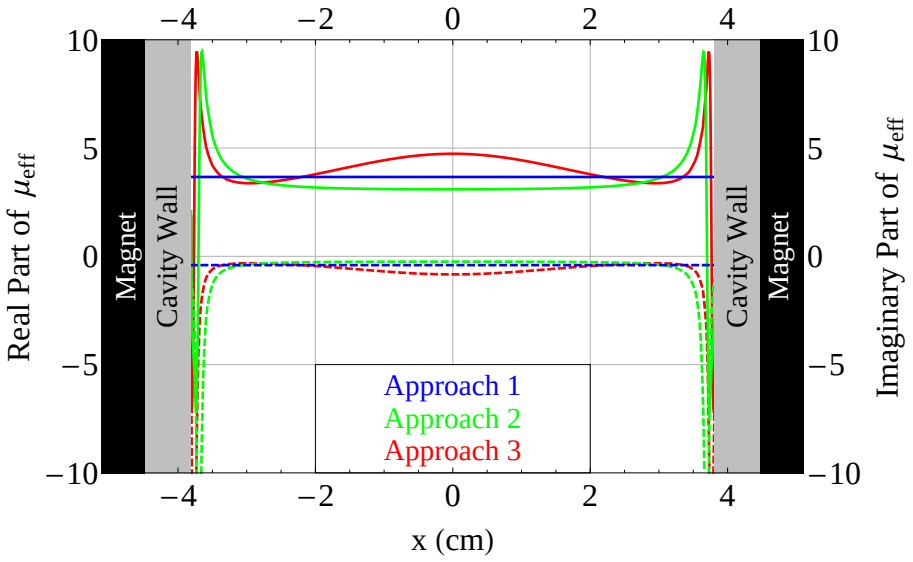

Figure 7.30: Real (solid) and imaginary (dashed) parts of the effective permeability μ_{eff} along the center-line of the ferrite G-475 biased by the electromagnet as shown in Figure 7.22.

As was mentioned before, the internal field distributions in Figure 7.24 are not severely non-uniform. Thus, even if averaging these distributions ignores some of the non-uniformities, it is not unreasonable to expect good accuracy even when the uniform blue distribution is used. Since the internal field distributions are similar, the permeability tensors computed using these distributions are also similar. Figure 7.30 demonstrates this statement graphically. It shows distributions of the real and imaginary parts of the effective permeability, μ_{eff}, defined by (6.4) and computed using three internal magnetic field distributions shown in Figure 7.24. As can be seen, the effective permeabilities are very similar, as a result, RF simulations also produce very similar results.

Thus, the three approaches yield the same results if the ferrite material is uniformly magnetized by a very strong magnetic field or if the internal magnetic field is not severely non-uniform. This appears to be the case when the ferrite is biased using the symmetric x-biasing configurations presented in this section.

7.4 Ferrite-Loaded CBS Antennas with Asymmetric X-Biasing.

Designs presented in this section utilize permanent magnets or an electromagnet to bias the ferrite material along its longest dimension, the x-dimension. But, unlike in the previous section, the magnets are only placed on either left or right side of the cavity. In other words, only one wall of the cavity is next to the pole of the magnet, the other (opposite) wall is free. Such a configuration is referred to as the *asymmetric x-biasing configuration*. The asymmetry implies asymmetric placement of the magnets with respect to the yz-plane. The applied magnetic field generated by such a configuration has H_x^a and H_z^a components. However, the effect of the H_z^a component on the internal magnetic field is not very strong and the H_z^i component of the internal field is much weaker than the H_x^i. Therefore, like in the previous section, the dominant component of the applied magnetic field for this biasing configuration is H_x^a. The magnitude of this component varies substantially from the wall near the pole of the magnet to the free wall.

The results in the previous sections demonstrated that Approach 3 can ensure accurate predictions but they did not show that this approach is much more accurate than Approaches 1 and 2. The main reason is the relatively uniform applied magnetic field due to the symmetric biasing configurations. To show the superiority of Approach 3, the non-uniformities of the applied magnetic field are enhanced by using the asymmetric x-biasing configurations presented here. Asymmetric placement of the magnets ensures that the applied magnetic field and, as a result, the induces internal magnetic field are severely non-uniform. The analysis in this section is essential for this study because it demonstrates the significance of the non-uniform applied magnetic field and the necessity to incorporate it in the modeling without averaging.

This section consists of the following sub-sections presenting three designs and the discussion of the results.

- Asymmetric x-biasing using two permanent magnets. Ferrite G-475.
- Asymmetric x-biasing using electromagnet.
  - Ferrite G-475
  - Ferrite G-1006
  - Ferrite TT2-113
- Asymmetric x-biasing using an electromagnet and different ferrite configuration. Ferrite G-475.
- Discussion.

The first two sub-sections present designs based on the ferrite configuration shown in Figure 7.1; the same configuration as in the previous section, one layer of the ferrite material on top of the probe. The third sub-section presents a different ferrite configuration in which the ferrite material is moved all the way to the aperture. Each sub-section presents simulations and measurements of the input impedance. In addition, the first sub-section also presents comparison of the simulated and measured radiation patterns. The last section presents discussion of the results.

Asymmetric X-bias Using Permanent Magnets.

The dimensions of the geometry and the biasing configuration are shown in Figure 7.31. The ferrite material is biased by two permanent magnets stacked on one side of the cavity as shown in the figure. The computer-aided design in Ansys Maxwell 3D is shown in Figure 7.32. The ferrite material is G-475 with the initial magnetization

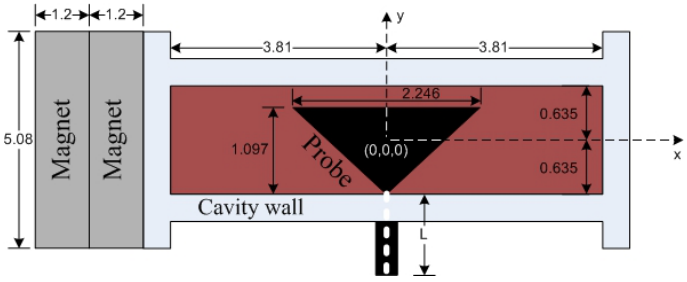

(a) Top view

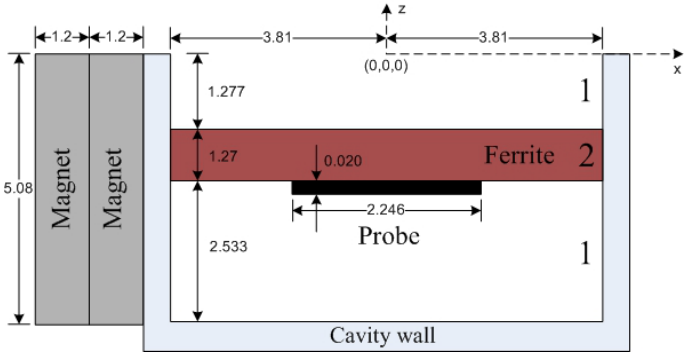

(b) Side view

Figure 7.31: Rectangular cavity loaded with one layer of the ferrite material biased in the x-direction using permanent magnets in asymmetric configuration (units of length: cm).

curve approximated by (5.11). The permanent magnets are NdFe35 with the uniform coercivity $H_c = 1,050$ (A/m).

The H_x^i component of the simulated internal magnetic field distributions are shown in Figure 7.33. The distributions are plotted along the center-line of the ferrite material. The blue, green, and red curves represent distributions computed using Approaches 1, 2, and 3, respectively. As can be seen, qualitatively and quantitatively the red distribution is very different from the blue and green distributions. It exhibits severe non-uniformity, with the field as high as 3,200 (Oe) at the cavity wall near the magnets and nearly zero at the opposite wall. The uniform blue distribution based on Approach 1 is computed as follows

$$H_x^i = H_x^a - N4\pi M_s = 868 - 0.0168 \times 500 \simeq 859 \text{ Oe} \tag{7.6}$$

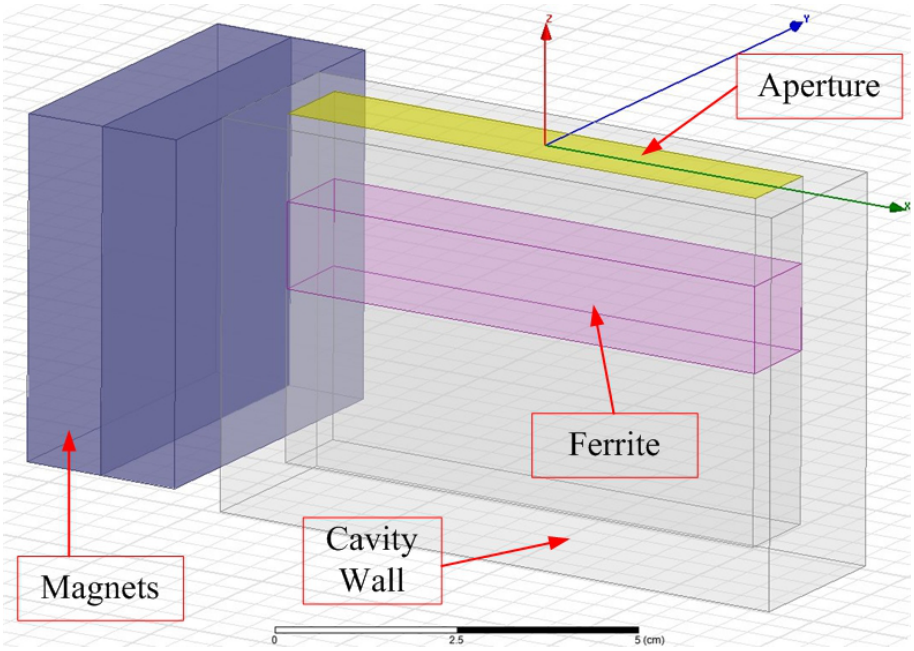

Figure 7.32: Computer-aided design in Ansys Maxwell 3D.

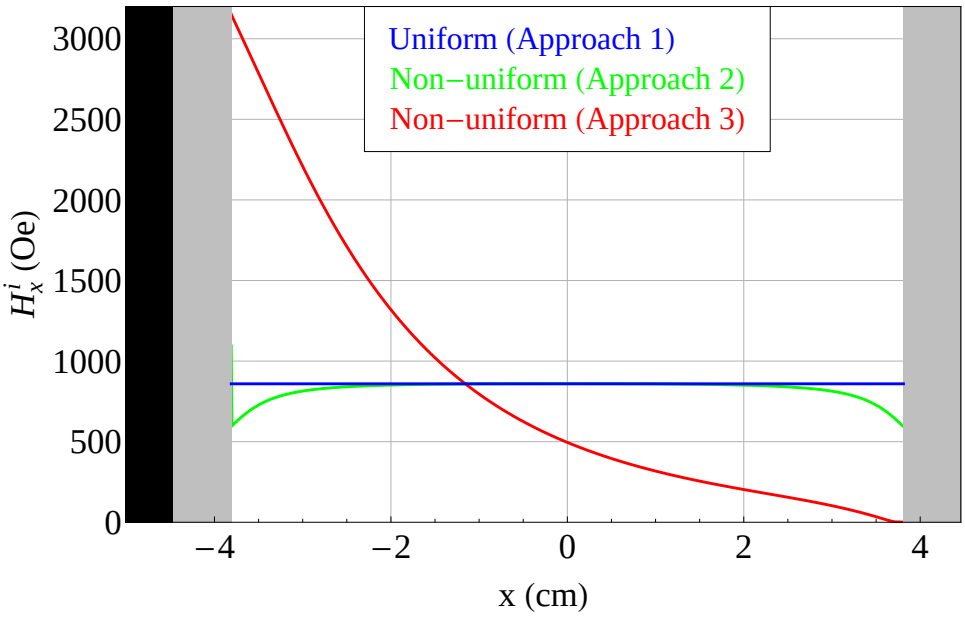

Figure 7.33: H_x^i component of the magnetic field inside the ferrite material along the ferrite center-line $(x, 0, -1.912)$ cm.

The distribution based on Approach 2 is for the most part uniform, but the non-uniformities are clearly visible near the ferrite-air interface. These none-uniformities are solely due to the magnetic field satisfying the boundary conditions at this interface. Neither the green nor blue distribution reflect the fact that the applied magnetic field is non-uniform. Thus, ignoring these non-uniformities resulted in very inaccurate computations of the internal magnetic field.

The RF simulations are performed using the Ansys HFSS model shown in Figure 7.1 and the material parameters in Table 7.10. Figure 7.34 shows the measured an simulated input impedances based on the internal field distributions in Figure 7.33. Approach 3 shows excellent agreement with measurements whereas Approaches 1 and 2 are very inaccurate. Using the non-uniform results and measurements as a baseline, the center frequency is off by $\simeq 40$ MHz, the predicted peak amplitude of the input resistance is $\simeq 1,000$ ohms, instead of 120 ohms. Figure 7.35 shows the E- and H-plane radiation patterns measured and simulated at $f = 0.94$ GHz when the cavity is flush-mounted on the square (30×30) cm ground plane. Like with the input impedance predictions, Approach 3 yields excellent results and Approaches 1 and 2 overestimate the gain by $\simeq 10$ dB.

Table 7.10: Material Parameters in Figure 7.31

Material	#	Thickness	Parameters
Air	1	1.9558	$\varepsilon_r = 1$
Ferrite: G-475	2	1.267	$\varepsilon_r = 13.35$, $g = 2.00$ $4\pi Ms = 500$ G, $\Delta H = 40$ Oe

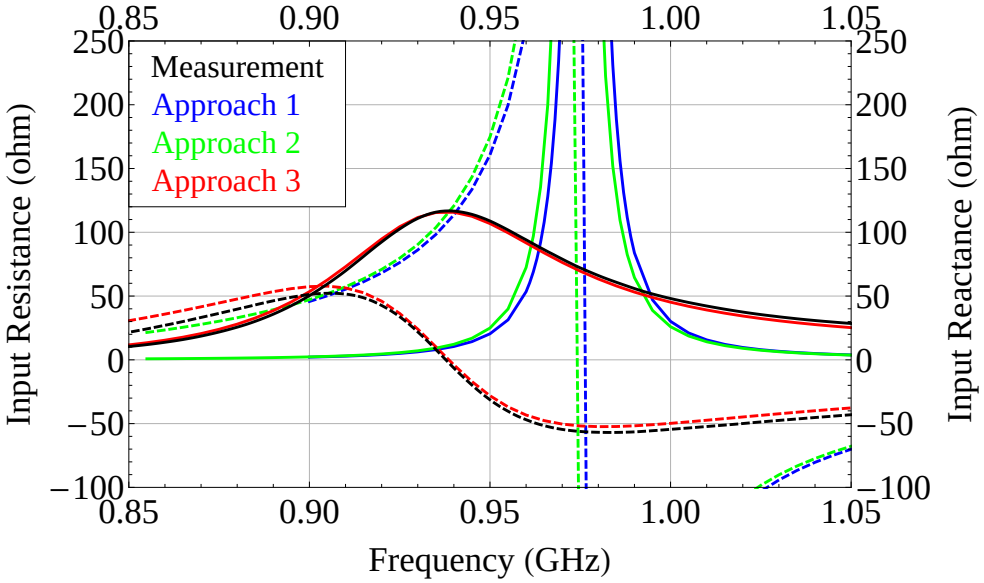

Figure 7.34: Real (solid) and imaginary (dashed) parts of the simulated and measured input impedance. Ferrite G-475.

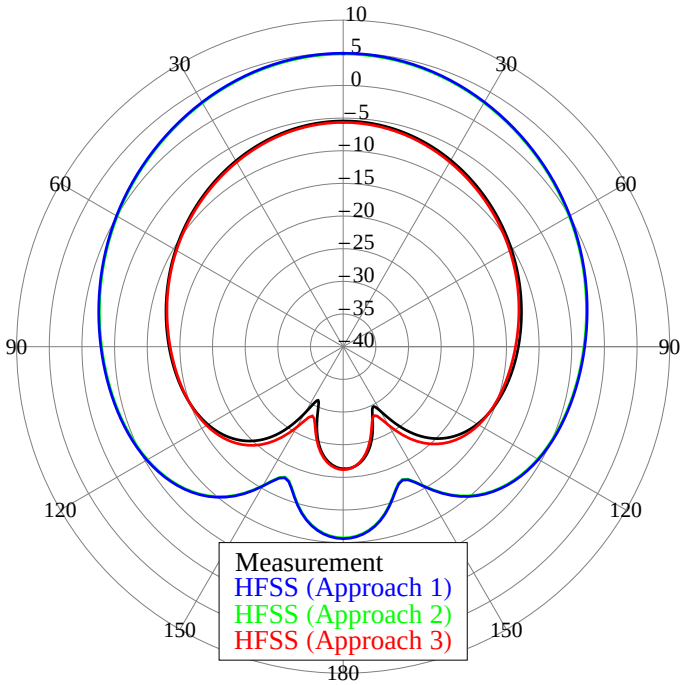

(a) E-plane.

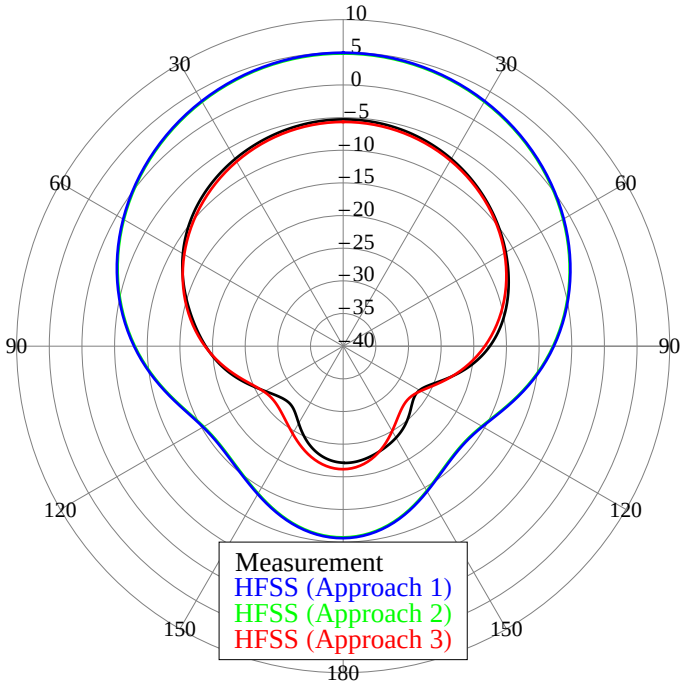

(b) H-plane.

Figure 7.35: Radiation patterns in the E- and H-planes at $f = 0.94$ GHz.

Asymmetric X-bias Using Electromagnet.

The geometry and the biasing configuration are shown Figure 7.36. To achieve asymmetric biasing in the x-direction, one half of the electromagnet is removed and the cavity is placed next to one of the poles of the electromagnet as shown in the figure. The computer-aided design in Ansys Maxwell 3D is shown in Figure 7.37.

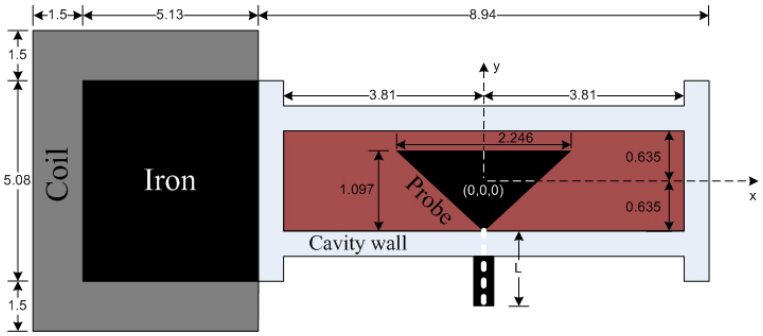

(a) Top view

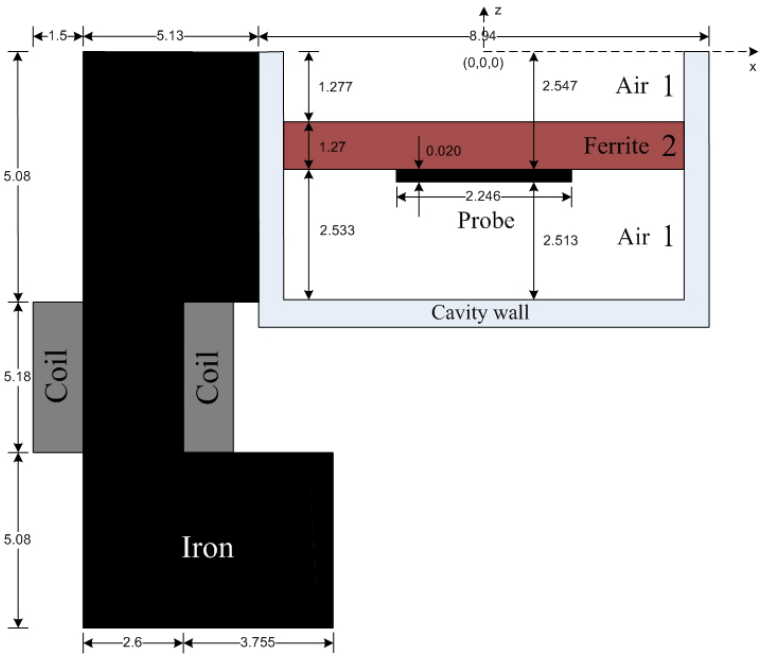

(b) Side view

Figure 7.36: Rectangular cavity loaded with one layers of the ferrite material biased in the x-direction using electromagnet in asymmetric configuration (units of length: cm).

Table 7.11: Current Excitation in the Coil Terminals.

Current Excitation	$I = 2.00$ amp	$I = 4.00$ amp	$I = 7.00$ amp
$Value$	1,700	3,400	5,959

The cavity was loaded with one of the ferrite materials: G-475, G-1006, or TT2-113. For the non-linear magnetostatic simulations, their initial magnetization curves are approximated by (5.11) with the corresponding adjustable parameters given in Table 5.2. The iron core of the electromagnet is modeled as the non-linear material, Steel-1008, from the Ansys Maxwell 3D library of materials. The coil is a solid copper object. The ferrite materials were subjected to three applied magnetic fields of various intensity. The intensity of the applied field was controlled by the current in the coil, which was set to $I = 2, 4, 7$ amp. The corresponding current excitations in the Ansys HFSS simulations are listed in Table 7.11.

Figure 7.38 shows simulated H_x^i component of the magnetic field inside the ferrite G-1006 when the current in the coil is $I = 4.00$ amp. The blue, green, and red curves represent distributions computed using Approaches 1, 2, and 3, respectively. The distributions are plotted along the center-line of the ferrite material, (x, 0, -1.912) cm. The green curve is obtained using Approach 2 with the uniform applied field $H_x^a = 201$ (Oe), and the uniform blue distribution based on Approach 1 is computed as follows

$$H_x^i = H_x^a - N4\pi M_s = 201 - 0.0168 \times 400 = 194 \text{ Oe} \tag{7.7}$$

Table 7.12 contains the applied and internal magnetic fields for all three ferrite materials at the three magnetization states. The magnetization state is determined by the current in the coil; $I = 2.00$ amp being the weakest and $I = 7.00$ amp the strongest magnetization state.

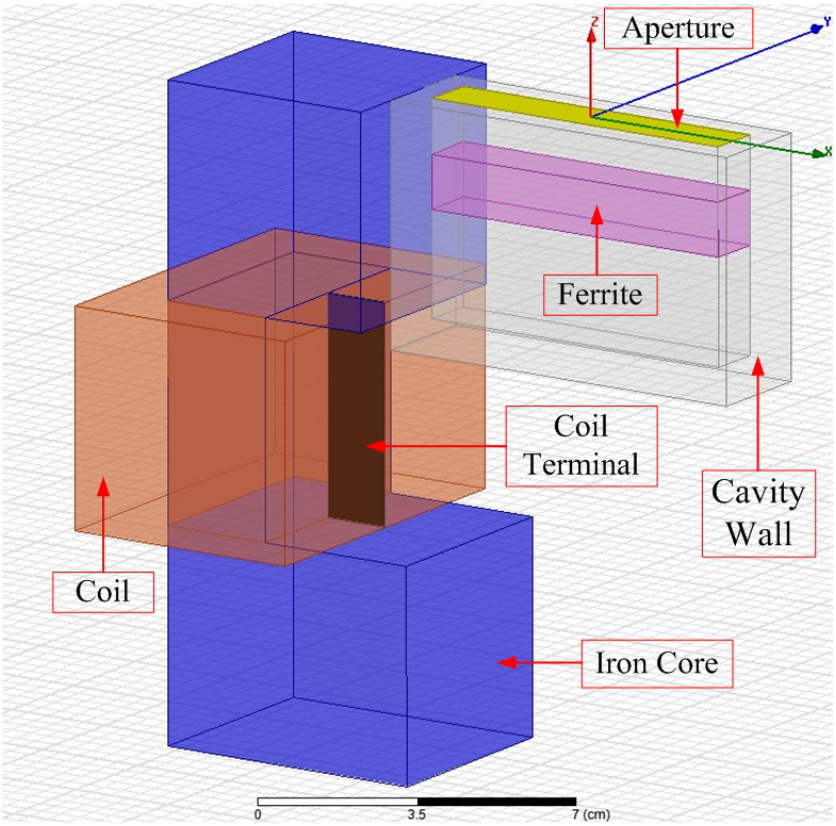

Figure 7.37: Computer-aided design in Ansys Maxwell 3D.

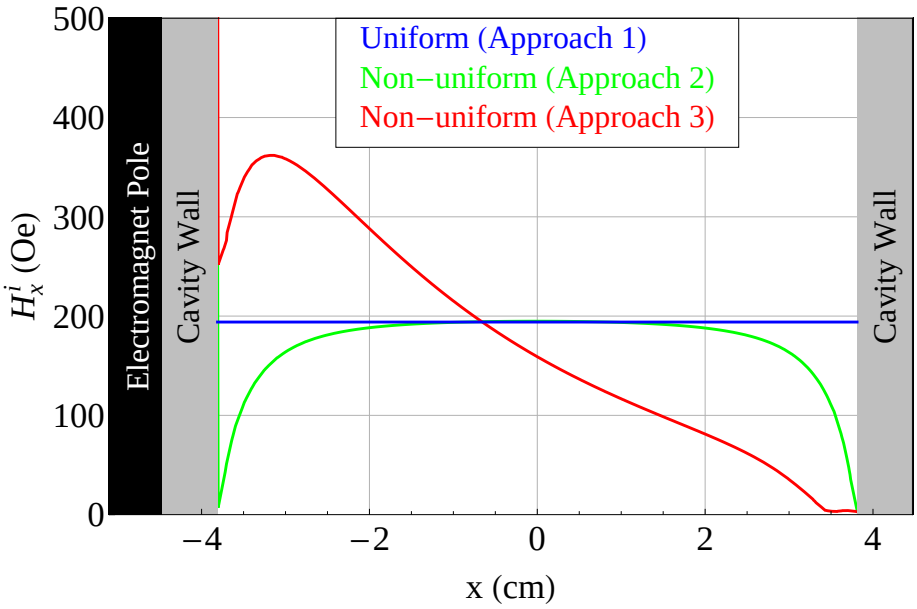

Figure 7.38: H_x^i component of the magnetic field inside the ferrite material along the ferrite center-line $(x, 0, -1.912)$ cm.

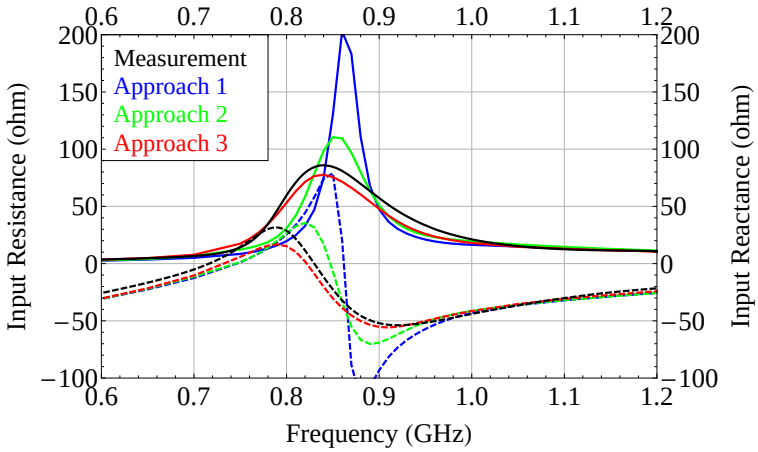

(a) I=2.00 amp.

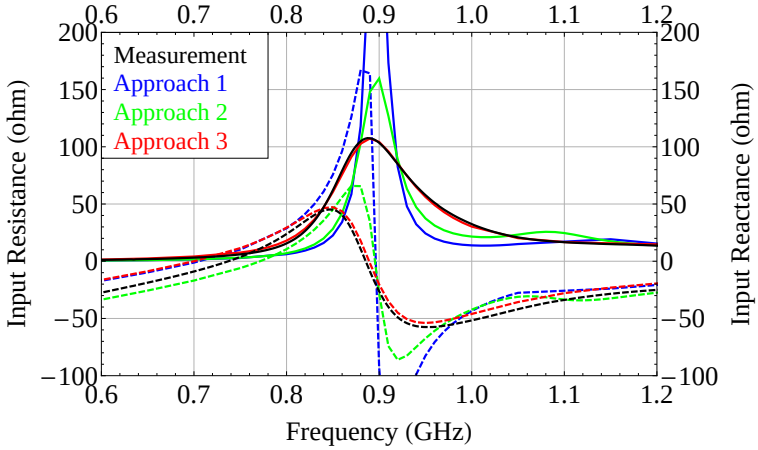

(b) I=4.00 amp.

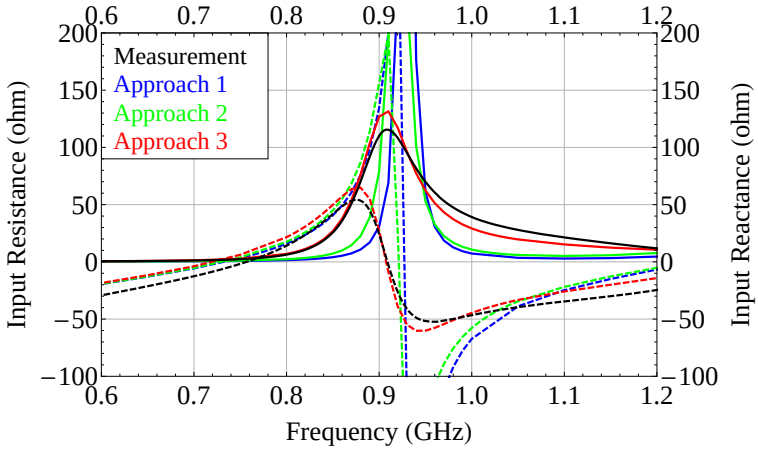

(c) I=7.00 amp.

Figure 7.39: Real (solid) and imaginary (dashed) parts of the predicted and measured input impedance of the CBS antenna loaded with ferrite G-475 as shown in Figure 7.36.

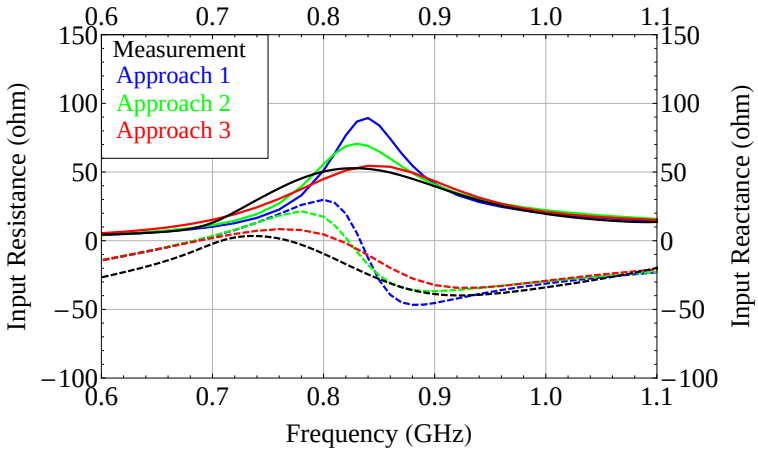

(a) I=2.00 amp.

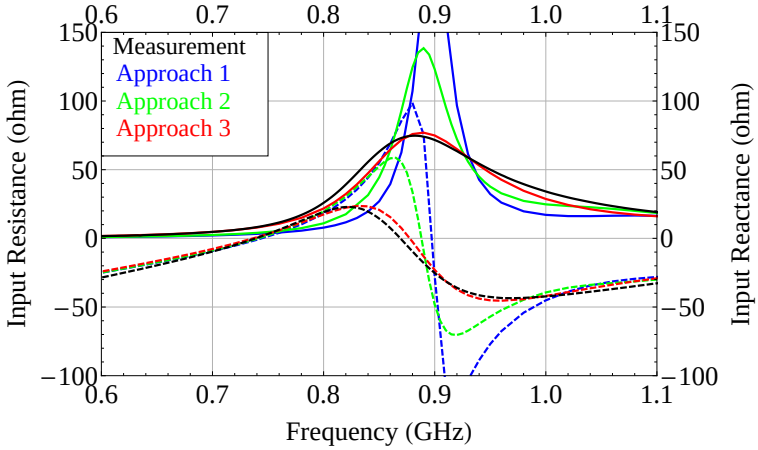

(b) I=4.00 amp.

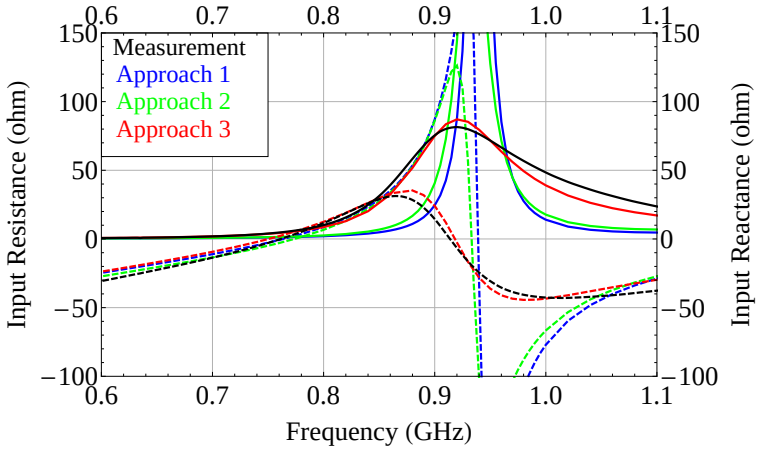

(c) I=7.00 amp.

Figure 7.40: Real (solid) and imaginary (dashed) parts of the predicted and measured input impedance of the CBS antenna loaded with ferrite G-1006 as shown in Figure 7.36.

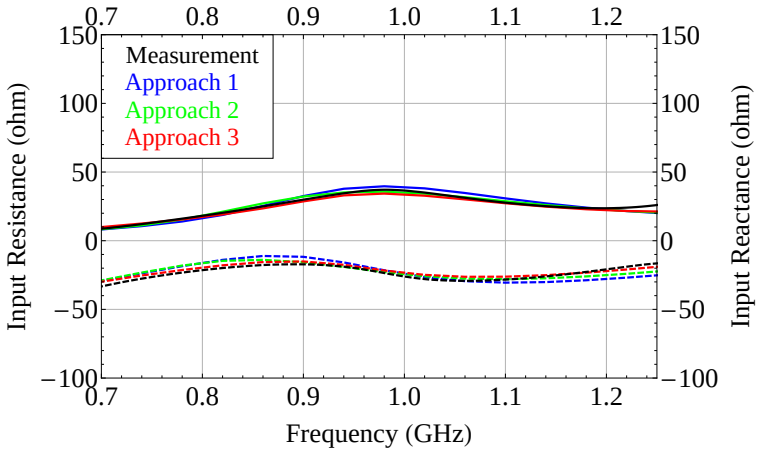

(a) I=2.00 amp.

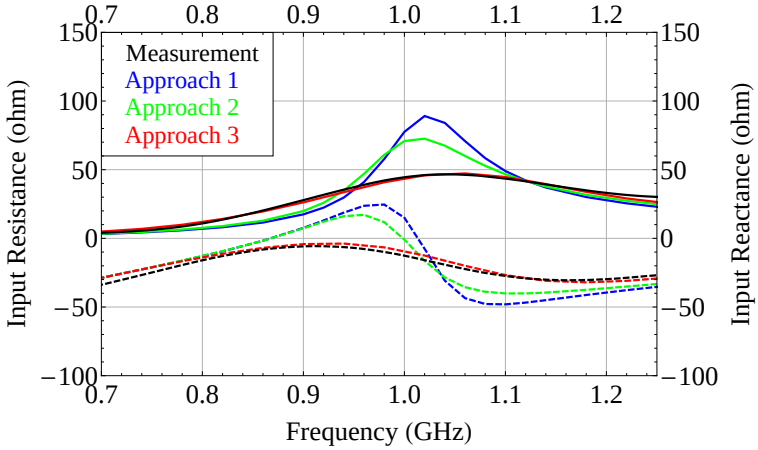

(b) I=4.00 amp.

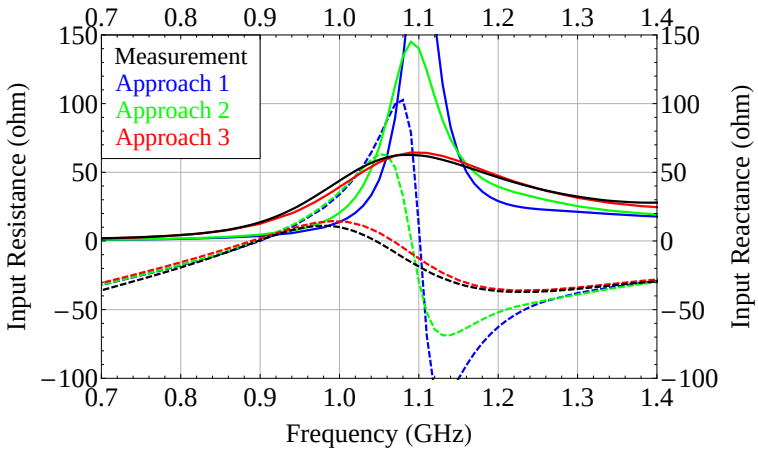

(c) I=7.00 amp.

Figure 7.41: Real (solid) and imaginary (dashed) parts of the predicted and measured input impedance of the CBS antenna loaded with ferrite TT2-113 as shown in Figure 7.36.

Table 7.12: Applied and Internal Magnetic Fields in Approaches 2 and 1.

Ferrite	I=2.00 amp H_x^a/H_x^i (Oe)	I=4.00 amp H_x^a/H_x^i (Oe)	I=7.00 amp H_x^a/H_x^i (Oe)
G-475	101/92	201/192	352/344
G-1006	101/94	201/194	352/345
TT2-113	101/91	201/191	352/343

Table 7.13: Ferrite G-475 Parameters.

Current	$4\pi Ms$ (G)	ΔH (Oe)	ε_r	g-factor
I = 2.00 amp	530	40	13.35	2.01
I = 4.00 amp	500	48	13.35	2.01
I = 7.00 amp	475	48	13.35	2.01

Table 7.14: Ferrite G-1006 Parameters.

Current	$4\pi Ms$ (G)	ΔH (Oe)	ε_r	g-factor
I = 2.00 amp	450	78	13.35	2.01
I = 4.00 amp	450	71	13.35	2.01
I = 7.00 amp	400	78	13.35	2.01

Table 7.15: Ferrite TT2-113 Parameters.

Current	$4\pi Ms$ (G)	ΔH (Oe)	ε_r	g-factor
I = 2.00 amp	600	100	8.3	1.54
I = 4.00 amp	600	100	8.3	1.54
I = 7.00 amp	575	100	8.3	1.54

Measurements and simulations of the input impedances are shown in Figures 7.39, 7.40, and 7.41 for the CBS antennas loaded with the ferrite G-475, G-1006 and TT2-113, respectively. These predictions were obtained using Ansys HFSS model shown in Figure 7.1 and the ferrite parameters in Tables 7.13, 7.14, and 7.15. Each figure includes three sets of simulations corresponding to the three magnetization states. As can be seen, predictions based on Approach 3 are in very good agreement with measurement. In most cases, Approaches 1 and 2 predict accurate resonant frequency, but substantially overestimated the peak amplitude of the input impedance. generally, the second best predictions are based on Approach 2, and the predictions based on Approach 1 are usually the worst.

Asymmetric X-biasing Using an Electromagnet and Different Ferrite Configuration.

This section presents a design with a different ferrite loading configuration. The ferrite is located in the aperture of the cavity instead of being on top of the probe, as in the previous designs. The geometry and the biasing configuration are shown in Figure 7.42.

The internal magnetic field in Approach 3 was computed using the same Ansys Maxwell 3D model as in Figure 7.37 but with the ferrite material moved up to the aperture. The material parameters for the non-linear magnetostatic problem are the same as in the previous sub-section; the ferrite is G-475 with its initial magnetization curve approximated by (5.11), the iron core is Steel-1008 and the coil is a solid copper object, the current in the coil is $I = 7.00$ amp and the current excitation in the coil terminal is $Value = 5,950$. The internal magnetic field in Approach 1 was found to be $H_x^i = 320$ (Oe) and the applied magnetic field in Approach 2 is $H_x^a = 328$ (Oe). The internal field distributions are very similar to those in Figure 7.38 and therefore are not shown here.

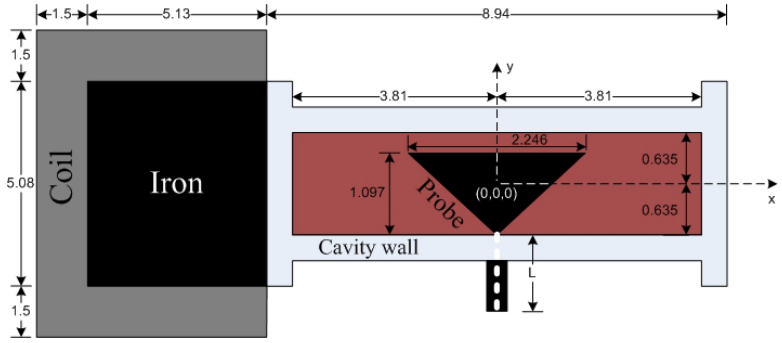

(a) Top view.

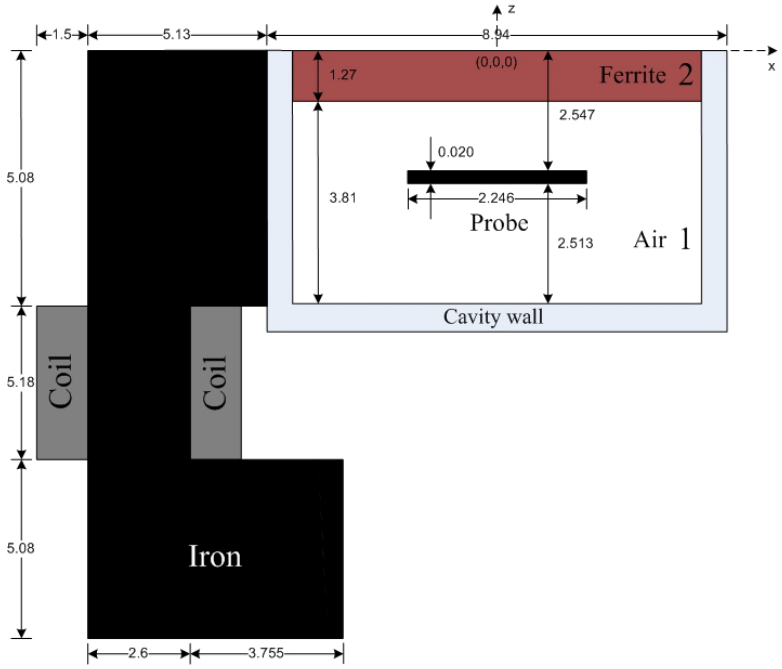

(b) Side view.

Figure 7.42: Rectangular cavity loaded with one layers of ferrite material biased in the x-direction using electromagnet in asymmetric configuration (units of length: cm).

Table 7.16: Material Parameters in Figure 7.42

Material	#	Thickness	Parameters
Air	1	3.81	$\varepsilon_r = 1$
Ferrite: G-475	2	1.27	$\varepsilon_r = 13.4$, $g = 2.01$ $4\pi Ms = 475$ G, $\Delta H = 48$ Oe

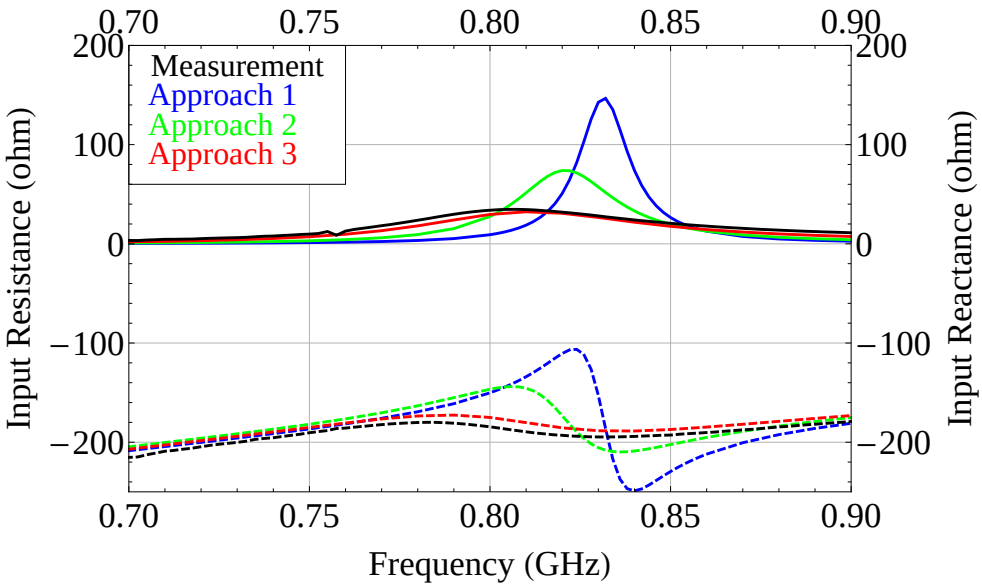

Figure 7.43: Real (solid) and imaginary (dashed) parts of the predicted and measured input impedance of the CBS antenna loaded with ferrite G-475 as shown in Figure 7.42.

Simulations and measurements of the input impedance are shown in Figure 7.43 and simulations of the radiation patterns in the E- and H-plane at $f = 0.81$ GHz in Figure 7.44. These simulations were obtained using the Ansys HFSS model shown in Figure 7.1 but with the ferrite material moved to the aperture. The material parameters in these simulations are given in Table 7.16. The simulations based on Approach 3 are in good agreement with measurements, whereas simulations based on Approaches 1 and 2 overestimate peak amplitude of the input impedance, as well as the resonant frequency. The predicted amplitude is greater than the measured one by $\simeq 100$ ohms and $\simeq 20$ ohms for Approaches 1 and 2, respectively. The resonant frequency is off by 20-30 MHz. Approaches 1 and 2 also predict stronger gain than Approach 3; Figure 7.44 shows that the gain is greater by $\simeq 12$ and $\simeq 5$ dB for Approaches 1 and 2, respectively.

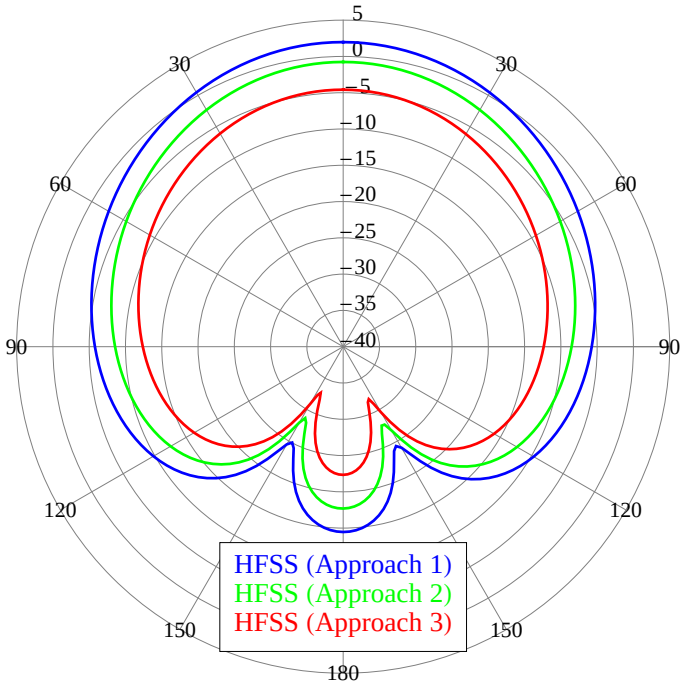

(a) E-plane.

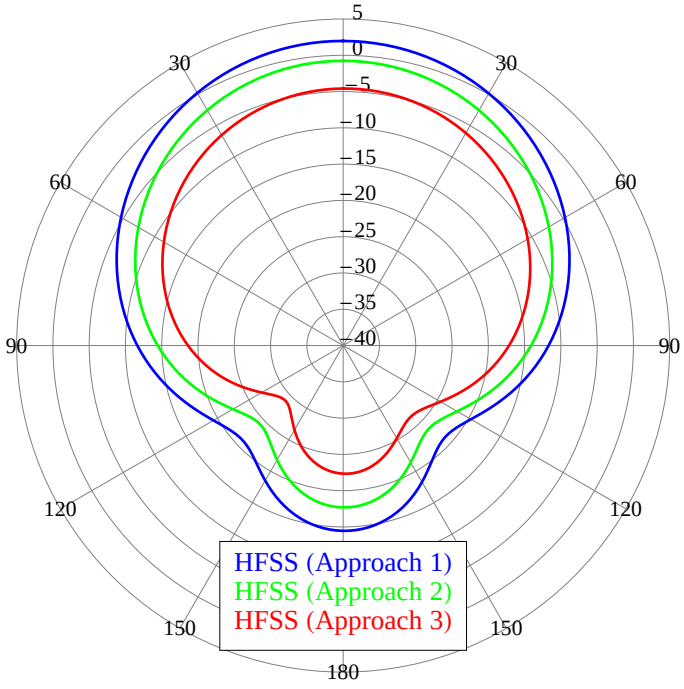

(b) H-plane.

Figure 7.44: E- and H-plane radiation patterns.

Discussion.

The pivotal point in this study is the demonstration that the non-uniformities of the applied magnetic field are significant and have to be incorporated in the modeling to attain accurate simulations. Results presented in this section provide such demonstration.

Simulations of the internal magnetic field in Figures 7.33 and 7.38 show that the applied magnetic field plays crucial role in shaping the distribution of the internal magnetic field. If the non-uniformities of the applied field are averaged, as is done in Approaches 1 and 2, the predicted internal field distribution looses some very important non-uniformities as well. This is especially evident in Approach 1, which predicts completely uniform internal field. Even the non-uniform distribution based on Approach 2 is inaccurate because it does not reflect that the ferrite material is biased by the asymmetric biasing configuration; qualitatively, this distribution is the same as the corresponding distribution in Section 7.3, where the symmetric biasing was considered (see Figure 7.14 or 7.19).

It was shown and explained in Section 7.3 that the effective permeabilities, computed using the internal field distributions from the three approaches, were not that different because the internal field distributions were similar. It is instructive to perform similar computations and analysis here. Figure 7.45 shows the real and imaginary parts of the effective permeability, μ_{eff}, defined by (6.4) and computed using the three internal magnetic field distributions shown in Figure 7.38. As can be seen, the effective permeabilities are very different. In Approach 1, for example, the real part of the effective permeability is always positive whereas in Approaches

2 and 3 it sometimes becomes negative. Parts of the ferrite where μ_{eff} is negative are cut-off. Such regions have significant impact on the radiation characteristics of the antenna, which is implicitly confirmed by the results presented in this section.

Comparisons of the simulated and measured input impedances and radiation patterns clearly demonstrate that approximating a severely non-uniform internal magnetic field with the uniform distribution is unacceptable because it leads to very inaccurate predictions. Approach 3, which does not perform such averaging, consistently yields much more accurate predictions than Approaches 1 and 2, which do perform the averaging.

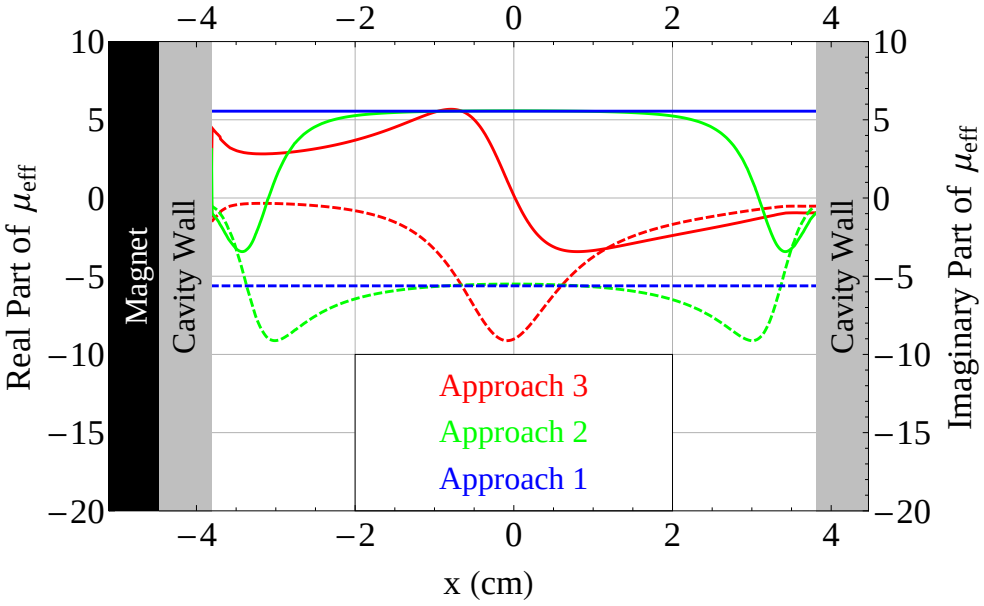

Figure 7.45: Real (solid) and imaginary (dashed) parts of the effective permeability μ_{eff} along the center-line of the ferrite G-1006 biased by the electromagnet as shown in Figure 7.38.

7.5 Ferrite-Loaded CBS Antennas with Asymmetric Z-Biasing.

The CBS antennas presented in this section are loaded with one layer of the ferrite material which is biased in the z-direction. The magnets are placed against the bottom wall of the cavity. Such configuration is referred to as the *asymmetric z-biasing configuration*. The asymmetry implies asymmetric placement of the magnets with respect to the xy-plane. Unlike in the previous sections, where the applied magnetic field has only one dominant component, H_x^a, the biasing field in this section has two equally important components, H_x^a and H_z^a.

The simulations and measurements presented in this section are interesting from the point of view that Approach 3 is a natural choice for the modeling of the CBS antennas loaded with the ferrite material which is biased in the direction perpendicular to the aperture (z-direction). The reason is the following. Biasing ferrite material in the direction perpendicular to the aperture imposes certain restrictions on where the magnets can be located. In particular, for the symmetric biasing in the z-direction, the magnets would have to be placed below, as well as above the aperture, and would interfere with the antenna radiation. To avoid such interference, the designer is restricted to placing the magnets only below the aperture. In Section 7.4, where the ferrite material was biased using the asymmetric x-biasing configuration, one may argue that there is no good reason to complicate matters by placing the magnets only on one side of the cavity and creating a severely non-uniform internal magnetic field. In this section, on the other hand, the designer may have no choice but to place the magnets asymmetrically with respect to the plane of the aperture. Since such biasing configuration will most likely lead to the non-uniform biasing of the ferrite material, the designer is forced to work with the non-uniform internal magnetic field. It was shown in the previous sections that in such cases Approaches

1 and 2 are likely to provide inaccurate predictions. Thus, the antenna designer is forced to look for an alternative, more accurate procedure. Approach 3 is such an alternative.

This section is divided into three sub-sections

- Asymmetric z-biasing using two permanent magnets. Ferrite G-475.
- Asymmetric z-biasing using electromagnet. Ferrite G-475.
- Discussion.

All the designs in this section are based on the ferrite configuration shown in Figure 7.1; one layer of the ferrite material on top of the probe. The first two sub-sections present comparison of the measured and simulated input impedances. In addition, the first sub-section also includes measurements and simulations of the antenna radiation patterns. The last section presents discussion of the results.

Asymmetric Z-Biasing Using Permanent Magnets.

The dimensions and the biasing configuration are shown in Figure 7.46. The ferrite material is biased in the z-direction (direction perpendicular to the aperture) by placing two stacked permanent magnets on the bottom sides of the cavity as shown in the figure. The computer-aided design in Ansys Maxwell 3D is shown in Figure 7.47. The ferrite material is G-475 with its initial magnetization curve approximated by (5.11). The permanent magnets are NdFe35 with non-uniform coercivity H_c; the numerical values for $H_{c(L)}$, $H_{c(M)}$, and $H_{c(R)}$ are given in Table 7.17.

The simulations of the H_z^i and H_x^i components of the internal magnetic field are shown in Figure 7.48. The distributions are plotted along the center-line of

Table 7.17: Coercivity H_c of the Permanent Magnets in Figure 7.47.

Magnet #	$H_{c(L)}$ (kA/m)	$H_{c(M)}$ (kA/m)	$H_{c(R)}$ (kA/m)
1, $(x = -5.74)$ cm	-1158	-727	-995
2, $(x = -6.94)$ cm	-1158	-727	-995

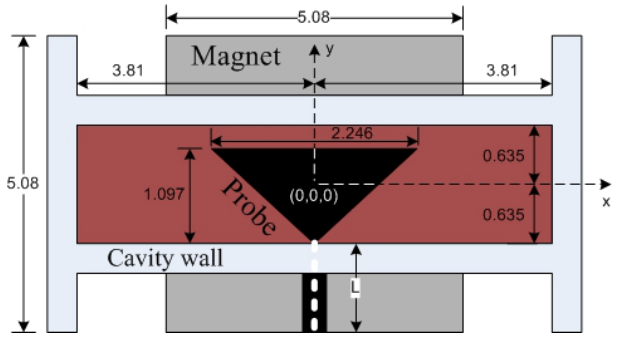

(a) Top view.

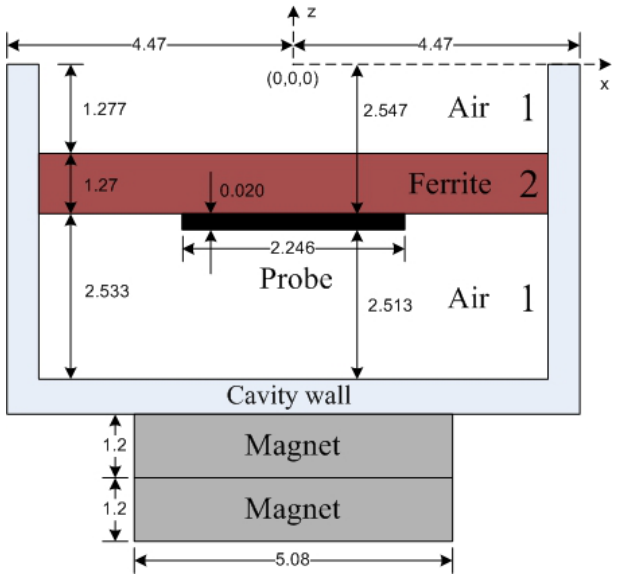

(b) Side view.

Figure 7.46: Rectangular cavity loaded with one layer of the ferrite material biased in the z-direction using permanent magnet in asymmetric configuration (units of length: cm).

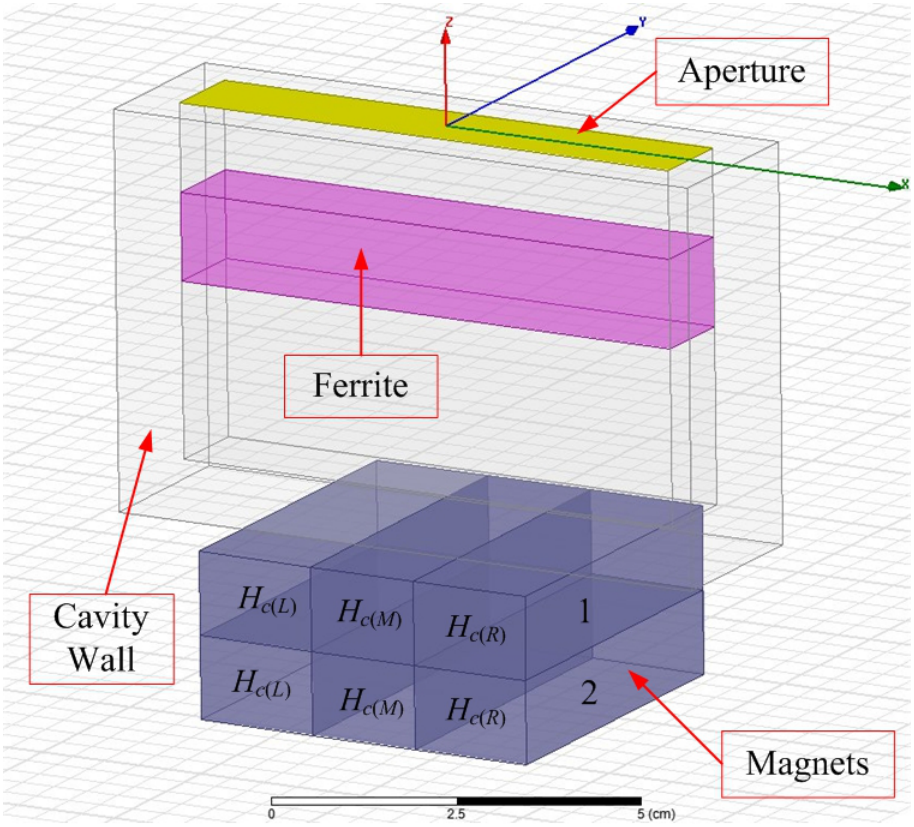

Figure 7.47: Computer-aided design in Ansys Maxwell 3D.

the ferrite material, (x, 0, -1.912) cm. The blue, green, and red curves represent distributions computed using Approach 1, 2, and 3, respectively. The green curve is obtained using Approache 2 with the uniform applied field $H_z^a = 481$ (Oe); volumetric average. The uniform blue distribution based on Approach 1 is computed as follows

$$H_z^i = H_z^a - N4\pi M_s = 481 - 0.4071 \times 500 = 280 \text{ Oe} \tag{7.8}$$

where the ballistic demagnetizing factor, $N = 0.4071$, was computed using (4.5). When this equation is compared with the similar equations in the previous sections, for example (7.1), it is seen that the ballistic demagnetizing factor is changed from $N = 0.0168$ to $N = 0.4071$. This is one of the consequences of biasing the ferrite material in a different direction; since the z-dimension of the ferrite material is smaller than its x-dimension, the ballistic demagnetizing factor is greater, i.e. closer to 1.

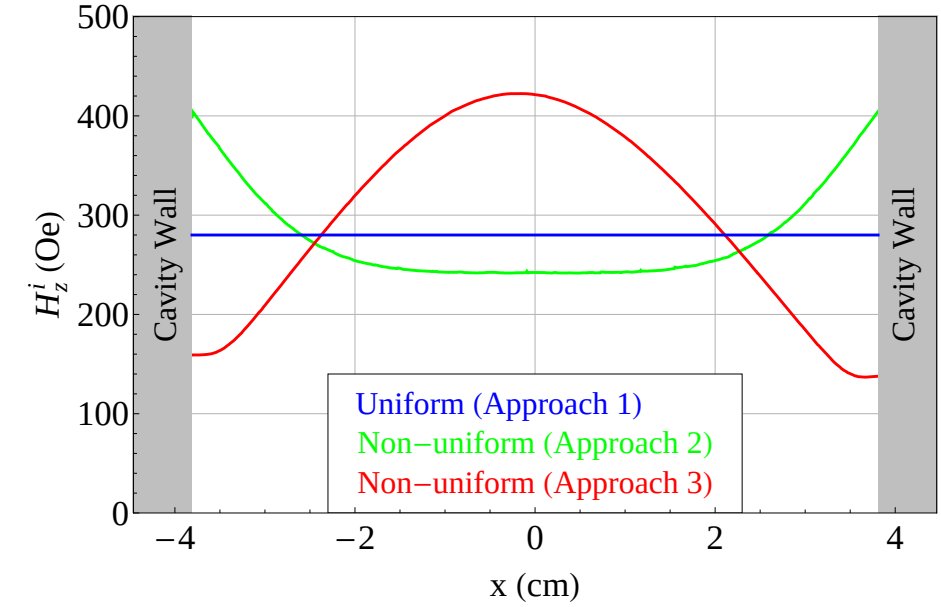

(a) H_z^i components.

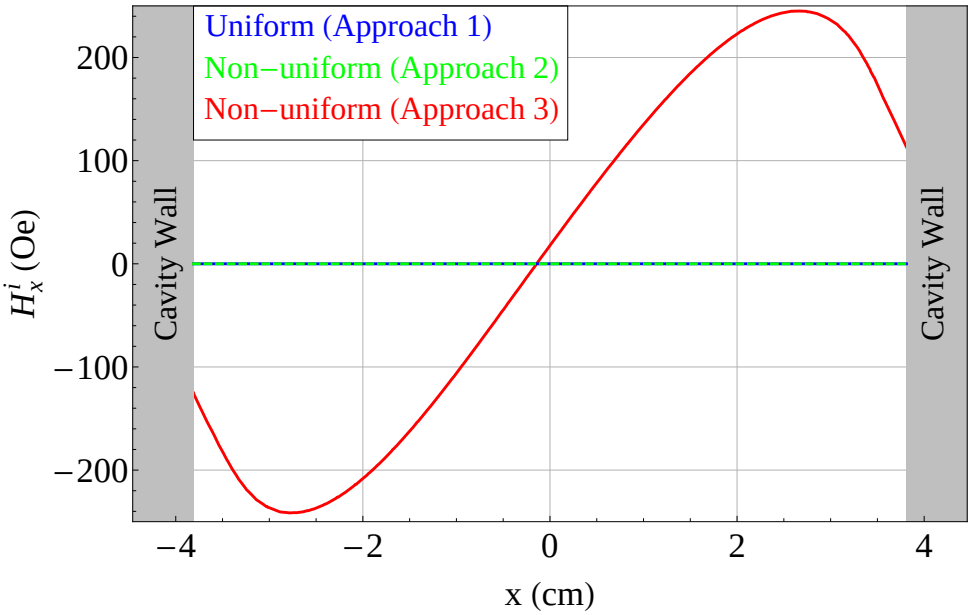

(b) H_x^i components.

Figure 7.48: H_z^i and H_x^i components of the magnetic field inside the ferrite material along the ferrite center-line, $(x, 0, -1.912)$.

Therefore, the demagnetizing term in Approach 1 is more significant when the ferrite material is biased along its shorter dimension. The internal magnetic field distributions in Figure 7.48 are symmetric with respect to the $x = 0$ plane (yz-plane). As before, the blue distribution is constant and the red and greed distributions are not. It is interesting to notice that qualitatively, the green distribution in Figure 7.48a looks almost like an inverted version of the red distribution; where the green curve is maximum, the red curve is minimum, and vice versa. Such opposite results can be understood by examining the difference between the applied magnetic fields used in Approaches 2 and 3. The vector plots of these fields in the xz-plane are shown in Figure 7.49. In Approach 2, the magnitude and direction of the applied field are uniform everywhere in the xz-plane; it has only H_z^a component (see Figure 7.49a). In contrast, the applied magnetic field in Approach 3 (Figure 7.49b) is non-uniform not only in terms of its magnitude, but also its direction; it has relatively strong H_x^a and H_z^a components near the walls of the cavity. Thus, it can be inferred that in Approach 2, the ferrite material is mainly magnetized in the z-direction, whereas in Approach 3 the direction of magnetization varies throughout the volume of the material. As a matter of fact, this can also be inferred from the plots of the internal magnetic field components in Figure 7.48. In Approach 2, the internal filed has only H_z^i component implying that the magnetization is along the z-direction. In Approach 3, the internal field has H_z^i and H_x^i components, which suggests that the magnetization is directionally non-uniform.

Simulations of the input impedance and the radiation patterns were obtained using Ansys HFSS model shown in Figure 7.1 and the material parameters in Table 7.18. The real (solid) and imaginary (dashed) parts of the predicted and measured input impedances are shown in Figure 7.50. The three simulations correspond to the three internal field distributions shown in Figure 7.48. As can be seen, the

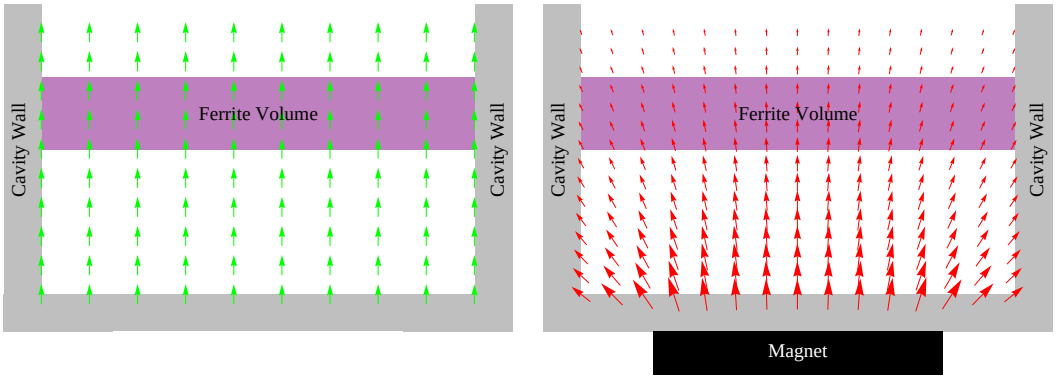

(a) Approach 2. (b) Approach 3.

Figure 7.49: Applied field H^a in the xz-plane.

simulation based on Approach 3 is in good agreement with measurements. The center frequency is off by $\simeq 8.0$ MHz, which corresponds to 0.8% error at $f = 0.95$ GHz and can be considered negligible. Simulations based on Approaches 1 and 2, are clearly inaccurate. The measured and simulated radiation patterns in the E- and H-planes are shown in Figure 7.51. The predictions based on Approach 3 are in excellent agreement with measurements, whereas Approaches 1 and 2 underestimate the gain by $\simeq 13$ and $\simeq 5$ dB, respectively.

Table 7.18: Material Parameters in Figure 7.46

Material	#	Thickness	Parameters
Air (top)	1	1.277	$\varepsilon_r = 1$
Air (bottom)	1	2.533	$\varepsilon_r = 1$
Ferrite: G-475	2	1.27	$\varepsilon_r = 13.35$, $g = 2.01$ $4\pi Ms = 500$ G, $\Delta H = 40$ Oe

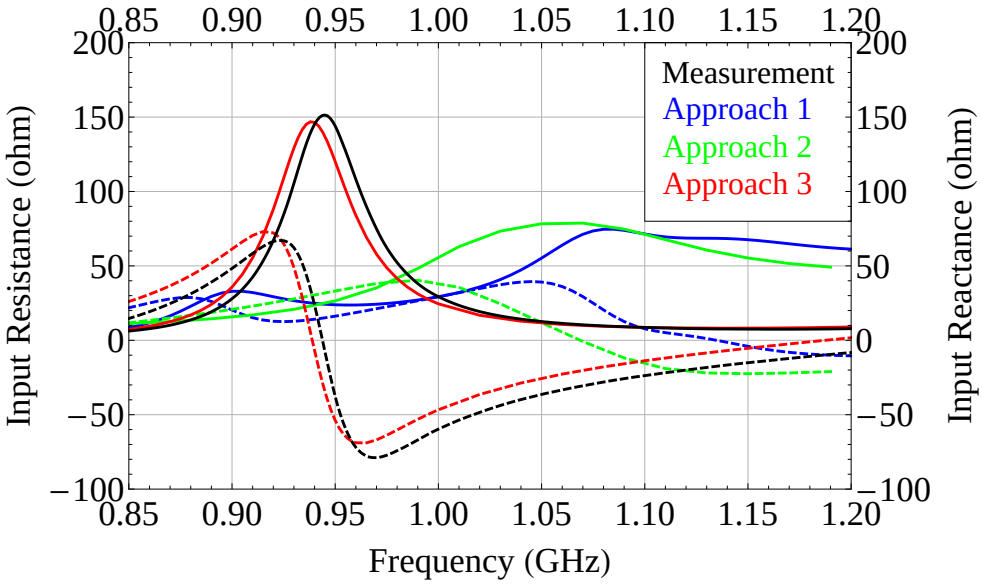

Figure 7.50: Real (solid) and imaginary (dashed) parts of the predicted and measured input impedance of the CBS antenna loaded with G-475 ferrite as shown in Figure 7.46.

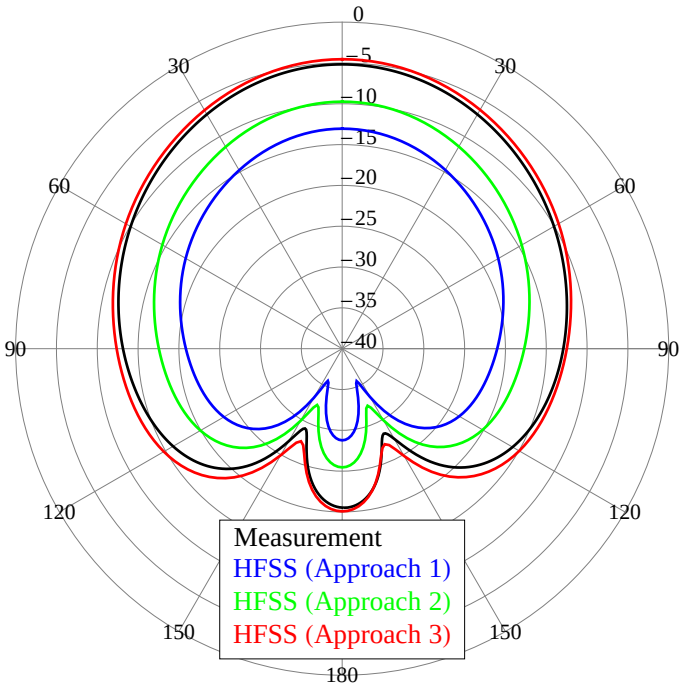

(a) E-plane

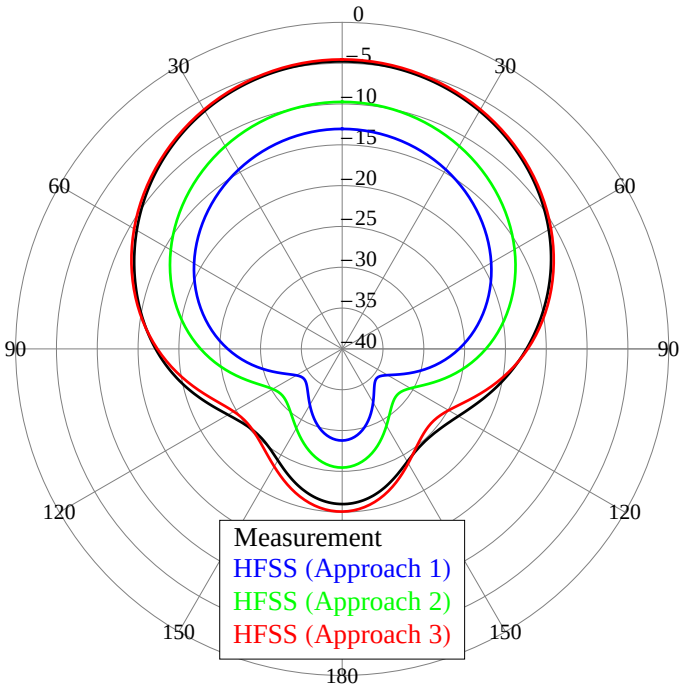

(b) H-plane

Figure 7.51: E- and H-plane radiation patterns.

The dimensions and the biasing configuration are shown in Figure 7.52. The ferrite material is biased in the z-direction, perpendicular to the aperture, by placing the

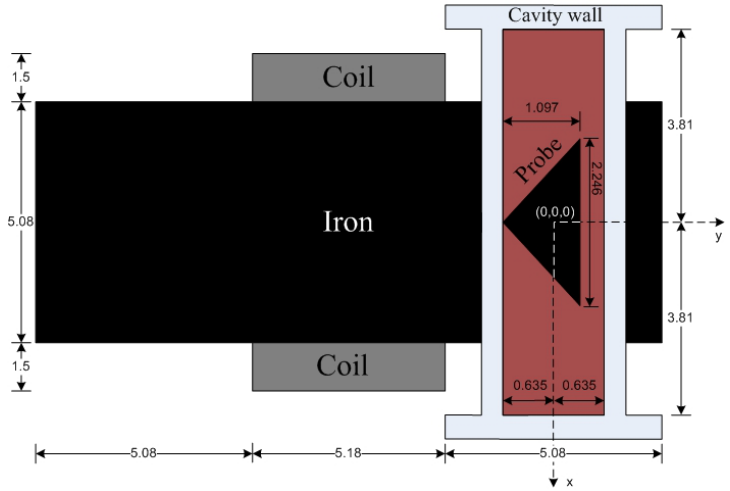

(a) Top view.

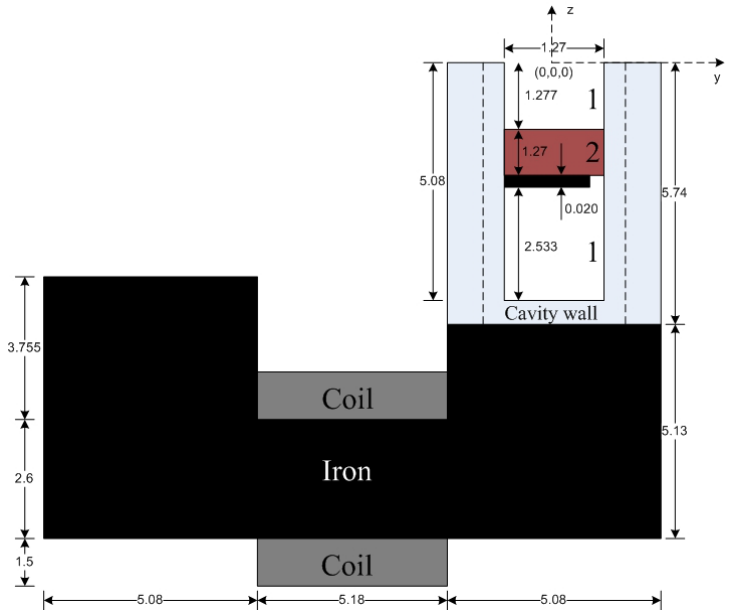

(b) Side view.

Figure 7.52: Rectangular cavity loaded with one layers of ferrite material biased in the z-direction using electromagnet in asymmetric configuration (units of length: cm).

bottom wall of the cavity on top of one of the poles of the electromagnet, as shown in the figure. The computer-aided design in Ansys Maxwell 3D is shown in Figure 7.53. The ferrite material is G-475 with its initial magnetization curve approximated by (5.11). The iron core is modeled as the non-linear material Steel-1008 from the Ansys Maxwell 3D library of materials, and the coil is modeled as a solid copper object. The current in the coil is $I = 4.00$ amp, and the current excitation in the coil terminal is

$$Value = I \times N = 4.00 \times 850 = 3,400 \tag{7.9}$$

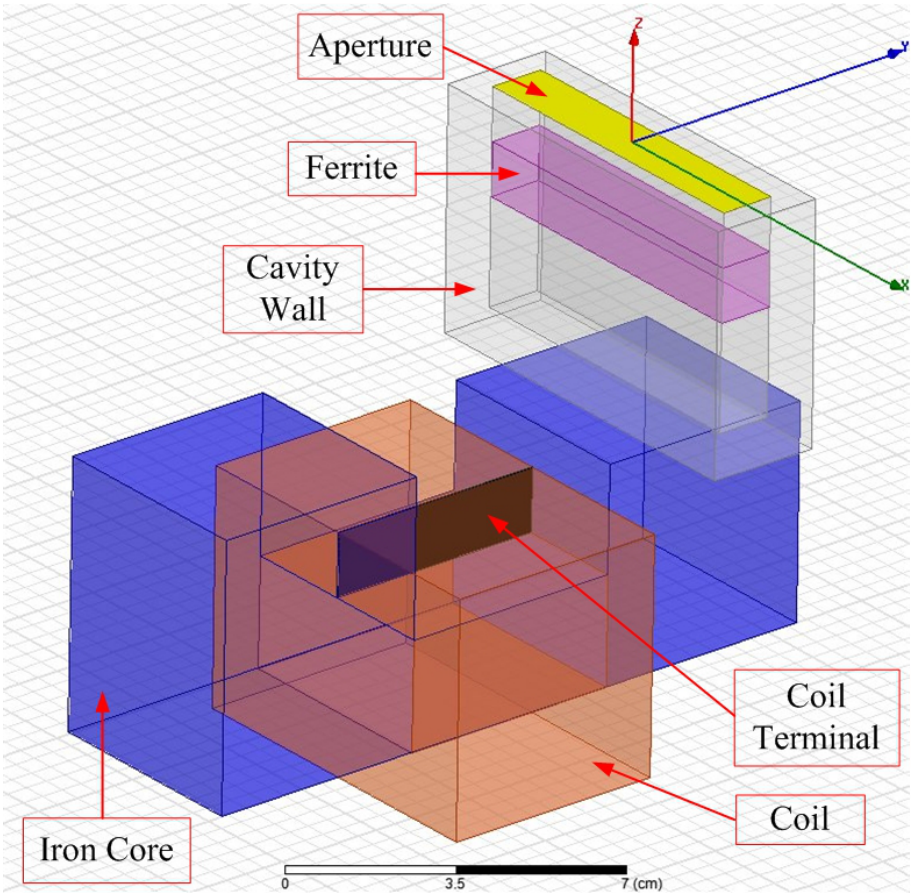

Figure 7.53: Computer-aided design in Ansys Maxwell 3D.

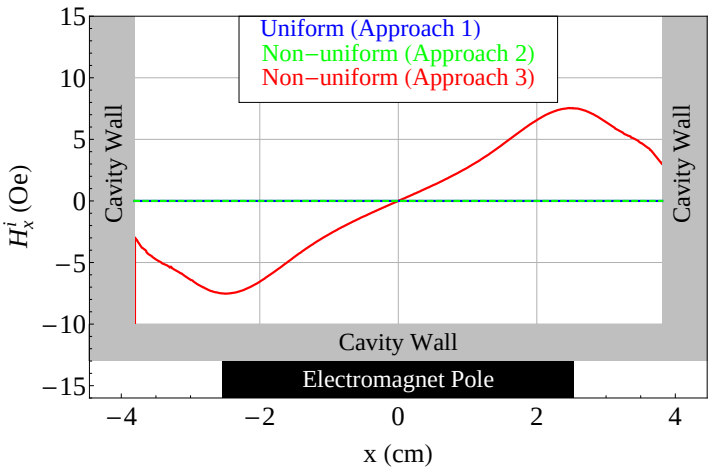

(a) H_x^i component.

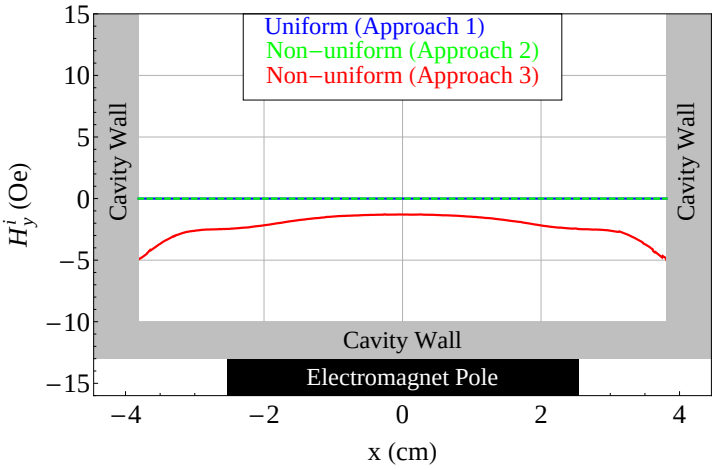

(b) H_y^i component.

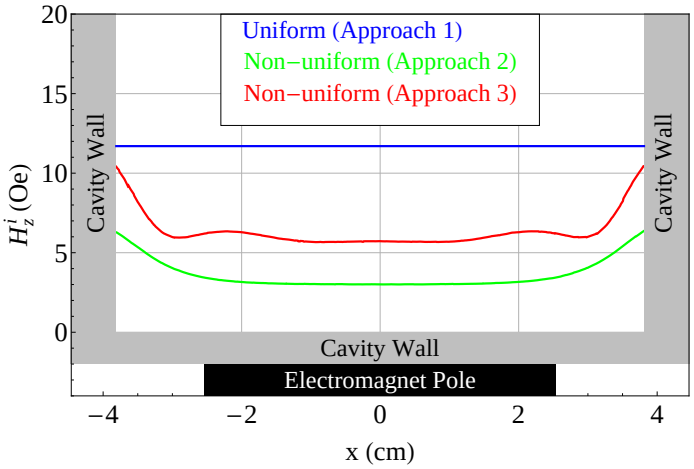

(c) H_z^i component.

Figure 7.54: Components of the magnetic field inside the ferrite material along the ferrite center-line, $(x, 0, -1.912)$.

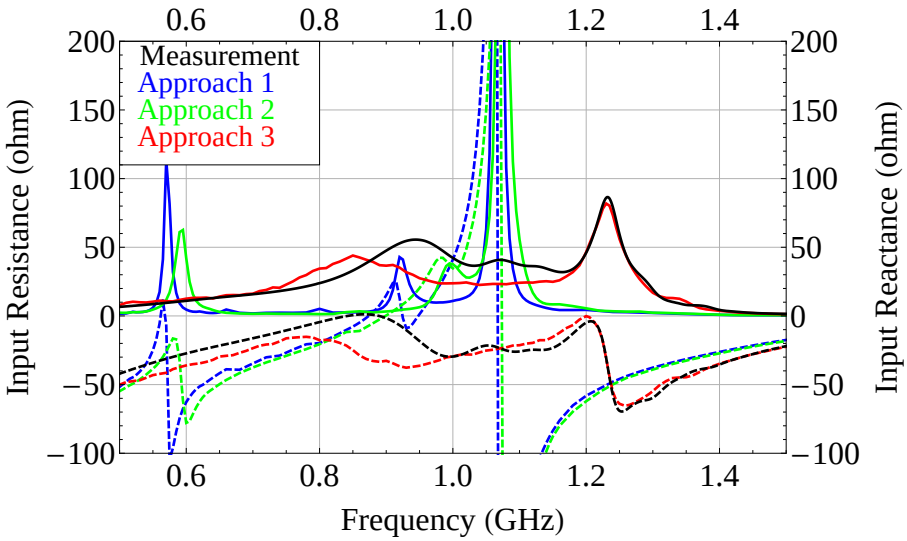

Figure 7.55: Real (solid) and imaginary (dashed) parts of the predicted and measured input impedance of the CBS antenna loaded with ferrite G-475 as shown in Figure 7.52.

The simulations of the components of the internal magnetic field are shown in Figure 7.54. As can be seen, Approaches 1 and 2 predict only one non-zero component, H_z^i, which is the consequence of the assumption that the applied magnetic field is uniform and has only one component, H_z^a. In contrast, Approach 3, which takes the non-uniform applied field into account, predicts three non-zero components. Even though these components are weak, they are on the same order of magnitude when compared to each other, which means that all three components are significant and should not be neglected.

Simulations and measurements of the internal magnetic field are shown in Figure 7.55. As can be seen, the part of the red curve around the second resonance is in good agreement with measurements but the part around the first resonance is not. The first predicted resonance is off by $\simeq 100$ MHz, 10% error at $f = 1.0$ GHz. Despite such mismatch, it is still obvious that Approach 3 is much more accurate than Approaches 1 and 2.

Discussion.

The main difference between the simulations in this section and the simulations in the previous sections is that the internal magnetic field has two significant components, H_z^i and H_x^i, as opposed to only one significant component, H_x^i, in the previous sections. This is the consequence of the appreciable directional non-uniformity of the applied magnetic field over the volume of the ferrite material, which can be clearly seen in Figure 7.49b.

It was pointed out in the beginning of Chapter 4 that the magnetic flux lines always form closed loops and that their direction cannot remain constant. Therefore, in general, the applied magnetic field along the center-line of the ferrite material has both H_x^a and H_z^a components. The significance of these components depends on how strong they are within the volume of the ferrite material. Since the orientation of the magnet is such that the biasing is in the z-direction, the H_z^a component is important by default. If the x-dimension of the magnet pole were the same or greater than the x-dimension of the ferrite material, the H_x^a component would be relatively weak, and it would be reasonable to assume that the applied field has only H_z^a component. Somewhat similar situation occurred in Section 7.4, where the applied magnetic field along the ferrite center-line has both H_x^a and H_z^a components but the latter is much weaker than H_x^a and its contribution is negligible. As can be seen from Figures 7.46 and 7.52, the x-dimension of the magnet pole is less than the x-dimension of the ferrite material, 5.08 cm versus 7.62 cm. As a result, the H_x^a component exhibits significant variation in magnitude and direction and should not be neglected. Since the direction of the internal field is mainly governed by the direction of the applied field, the internal field also has appreciable H_x^i component, as can be seen in Figure 7.48b.

The results presented in this section demonstrate the importance of the directional non-uniformity of the applied magnetic field. Failure of Approaches 1 and 2 to provide accurate predictions can be attributed to the fact that these approaches assume uniform applied magnetic field and ignore its directional non-uniformity. As a result, the directional non-uniformity of the internal magnetic field is also ignored. Approach 3, on the other hand, takes all components into account and therefore ensures more accurate predictions.

The effect of ignoring some of the components of the internal magnetic field can be observed on the frequency dependent permeability tensor. Approaches 1 and 2 assume only one non-zero component, H_z^i; therefore, the permeability tensor (3.2) can be written as

$$[\mu] = \begin{bmatrix} 1+\chi\cos^2(\theta_z) & j\kappa\cos(\theta_z) & 0 \\ -j\kappa\cos(\theta_z) & 1+\chi\cos^2(\theta_z) & 0 \\ 0 & 0 & 1 \end{bmatrix} = \begin{bmatrix} 1+\chi & j\kappa & 0 \\ -j\kappa & 1+\chi & 0 \\ 0 & 0 & 1 \end{bmatrix} \tag{7.10}$$

where the second equality follows because $\cos(\theta_z) = \frac{H_z^i}{|\vec{H}^i|} = 1$ since the internal field is $\vec{H}^i = \hat{a}_z H_z^i$. In Approach 3, the internal magnetic field has two non-zero components, $\vec{H}^i = \hat{a}_x H_x^i + \hat{a}_z H_z^i$. Therefore, the permeability tensor (3.2) can be written as

$$[\mu] = \begin{bmatrix} 1+\chi\cos^2(\theta_z) & j\kappa\cos(\theta_z) & -\chi\cos(\theta_z)\cos(\theta_x) \\ -j\kappa\cos(\theta_z) & 1+\chi(\cos(\theta_x)+\cos(\theta_z)) & j\kappa\cos(\theta_x) \\ -\chi\cos(\theta_z)\cos(\theta_x) & -j\kappa\cos(\theta_x) & 1+\chi\cos^2(\theta_x) \end{bmatrix} \tag{7.11}$$

where $\cos(\theta_z) = \frac{H_z^i}{|\vec{H}^i|}$ and $\cos(\theta_x) = \frac{H_x^i}{|\vec{H}^i|}$.

Quantities χ and κ are given by (3.3); in Approach 1 they are constant throughout the material and in Approaches 2 and 3 they are position dependent. The most obvious difference between (7.10) and (7.11) is that some of the off-diagonal entries in (7.10) are zero, whereas in (7.11) all the entries are non-zero. Thus, permeability tensor computed in Approaches 1 and 2 is very different from the tensor

computed in Approach 3. The results of this section attest that the simulations based on (7.10) are less accurate than the simulations based on (7.11). Therefore, the omission of the significant components of the internal magnetic field can substantially impair the accuracy of the predictions.

It should be noted that the relatively poor performance of Approach 3 in Figure 7.55 may be due to the very weak internal magnetic field. It can be deduced from Figure 7.54 that its magnitude is $|\vec{H}^i| \simeq 11$ ohms. Such low internal magnetic field suggests the possibility that the ferrite material is only partially saturated. Technically, the permeability tensor (3.2) is not applicable for the partially saturated states, because it is derived with the assumption that the material is saturated. Thus, it may be postulated that in Figure 7.55 Approach 3 does not perform as well as in the previous simulations because it is near the limit of its applicability due to the inability of the permeability tensor (3.2) to adequately represent partially magnetized ferrite materials.

Chapter 8

CONCLUSIONS

This dissertation advances the modeling and simulation of ferrite-loaded CBS antennas. The antennas considered here are loaded with the ferrite and dielectric materials which are subjected to a severely non-uniform applied magnetic field. It is common practice to average these non-uniformities and assume that the applied field is uniform. It was demonstrated that such an approach should be used with caution because a non-uniform applied magnetic field induces non-uniform internal magnetic field, which is a critical factor in the proper modeling and simulations.

Three approaches for the computation of the internal magnetic field were compared:

- Approach 1 based on the uniform applied and internal magnetic fields.
- Approach 2 based on the uniform applied and non-uniform internal magnetic fields.
- Approach 3 based on the non-uniform applied and internal magnetic fields.

It was shown that the accuracy of the input impedance simulations based on the approaches assuming uniform applied field deteriorates as the severity of the non-uniformities increases. Much better accuracy can be achieved if the non-uniform applied magnetic field distribution is explicitly included in the modeling. The procedure presented here clearly demonstrates this premise. Presented measurements and simulations of the input impedance and radiation patterns for the ferrite-loaded CBS antennas, biased using symmetric and asymmetric biasing configurations with permanent magnets or an electromagnet, support this statement. The simulations based on Approach 3 consistently demonstrated very good agreement with measure-

ments. Simulations based on Approaches 1 and 2 are usually inaccurate, unless the ferrite material is uniformly magnetized by a very strong magnetic field or if the internal magnetic field is not severely non-uniform. In such special cases, all three approaches yield good results. The directional non-uniformity of the applied magnetic field was also addressed and found to play very significant role. If some of the strong components of the internal magnetic field are omitted, the predictions become very inaccurate and do not compare well with measurements.

Chapter 9

RECOMMENDATIONS

The recommendations for the future work in this research topic can be summarized into three groups

- Improvement of the Fortran FEM code.
- Improvement of the radiation characteristics of the ferrite-loaded CBS antennas.
- Improvement of the permeability tensor for the partially magnetized ferrite materials.

Although the commercial software like Ansys HFSS is very flexible and versatile, a "home-built" personal FEM code can be invaluable in many ways. Writing such a code from scratch facilitates the learning process and reveals many intricacies of the analysis. It provides insight into the fundamental governing processes, and better understanding and interpretation of the results and phenomena. Therefore, the Fortran FEM code used in this study should not be discarded as a completely inferior tool in comparison with Ansys HFSS, but can be further developed and improved. One of the improvements is the possibility to use higher-order elements. Such modification will reduce the size of the global matrices and result in faster convergence of the numerical solution. Most of the integrals, however, will have to be evaluated numerically. Performing numerical integration efficiently in a least amount of time represents a challenge by itself. Another modification is the addition of the uniform theory of diffraction to take into account the finite dimensions of the ground plane. Also, the magnetostatic and RF parts of the Fortran codes can be combined and supplemented with a graphical user interface (GUI) to make them more user-

friendly. In addition, a very serious issue that needs to be addressed is the solution of the global finite element matrix. The tested iterative solvers appear to have very poor convergence rate and often stagnate whereas the direct solver used in this study is still rather slow. Thus, a better and faster solver is required to make the analysis using this Fortran code more efficient. Overall parallelization of the code can be considered as well.

Most of the simulations and measurements presented in this dissertation demonstrate very low gain, and the input impedance also suggest poor reflection coefficient. In order for the ferrite-loaded CBS antennas to be practical, these radiation parameters have to be improved. One way to do it is through shaping of the ferrite material. For example, some parts of the ferrite may be less important to the antenna radiation characteristics, meaning that these parts may be removed without significantly affecting the performance of the antenna. The dielectric and magnetic materials usually reduce the bandwidth and gain of the antenna therefore, by removing some of these materials may have a positive effect on the radiation characteristics. In addition, some areas in the cavity may be preferred for the placement of the ferrite material. For example, the last set of simulations and measurements in Section 7.4 demonstrates that moving the ferrite from the center of the cavity to the aperture significantly affects the input impedance of the antenna.

Finally, the last set of simulations and measurements in Section 7.5 indicates that the internal magnetic field is rather weak, which suggests that the ferrite material is partially saturated. As was explained in the *Discussion* part of the section, the expressions for the frequency dependent permeability tensor used in this study were derived with the assumption that the material is saturated and, technically, are not applicable for the partially saturated states. This is a known issue and characterization of such magnetization states has been attempted in the past. The empirical

formulas, as well as more rigorous derivations of the components of the permeability tensor were suggested in [57, 58, 25, 59, 60]. Nevertheless, at the time of writing this dissertation, no consistent and generally accepted treatment can be found in the literature. To be able to contribute in this area one would need to have a very good understanding of the domain processes and the governing physics, as well as substantial mathematical skills. In addition, this research may rely heavily on the experimentation with samples of various ferrite materials. Thus, working with and analyzing the performance of the partially saturated ferrite materials can be a very interesting and rewarding challenge.

REFERENCES

[1] D. J. Aggelakos and M. M. Korman, "Radiation from ferrite-filled apertures," *Proc. IRE*, vol. 44, pp. 1463–1468, Oct. 1956.

[2] D. B. Medved, "An electronic scan using ferrite aperture luneberg lens system," *IRE Trans. Microwave Theory Tech.*, vol. MTT-7, pp. 101–103, Oct. 1958.

[3] T. Chien and H. Unz, "Radiation from rectangular waveguide filled with ferrite slabs," *IRE Trans. Microwave Theory Tech.*, vol. MTT-13, no. 1, pp. 137–138, Jan. 1965.

[4] A. T. Adams, "Flush mounted rectangular cavity slot antennas - theory and design," *IEEE Trans. Antennas Propag.*, vol. AP-15, no. 3, pp. 342–351, May 1967.

[5] M. N. O. Sadiku, *Numerical Techniques in Electromagnetics*, 2nd ed. New York: CRC Press LLC, 2001.

[6] C. A. Balanis, *Advanced Engineering Electromagnetics*, 2nd ed. New Jersey: John Wiley & Sons, Inc., 2012.

[7] J. Jin, *The Finite Element Method in Electromagnetics*, 2nd ed. New York: John Wiley & Sons, Inc., 2002.

[8] A. Taflove and S. C. Hagness, *Computational Electromagnetics The Finite-Difference Time-Domain Method*, 3rd ed. Boston: Artech House, Inc., 2005.

[9] D. M. Pozar, *Microwave Engineering*, 3rd ed. New York: John Wiley & Sons, Inc., 2005.

[10] A. C. Polycarpou, "Finite element analysis of microwave passive devices and ferrite-tuned antennas," Ph.D. dissertation, Arizona State University, Tempe, AZ, 1998.

[11] M. N. Vouvakis, "Analysis of ferrite-loaded cavity-backed antennas using a hybrid finite element method," Master's thesis, Arizona State University, Tempe, AZ, 2001.

[12] A. C. Polycarpou, C. A. Balanis, J. T. Aberle, and C. R. Birtcher, "Radiation and scattering from ferrite-tuned cavity-backed slot antennas: Theory and experiment," *IEEE Trans. Antennas Propag.*, vol. AP-46, no. 9, pp. 1297–1306, Sep. 1998.

[13] V. G. Kononov, C. A. Balanis, A. C. Polycarpou, and C. R. Birtcher, "Nonuniform field modeling of ferrite-loaded cavity-backed slot antennas," *IEEE Trans. Antennas Propag.*, vol. 57, no. 10, pp. 3402–3405, Oct. 2009.

[14] M. N. Vouvakis, C. A. Balanis, C. R. Birtcher, and A. C. Polycarpou, "Ferrite-loaded cavity-backed antennas including nonuniform and nonlinear magnetization effects," *IEEE Trans. Antennas Propag.*, vol. AP-51, no. 5, pp. 1000–1010, May 2003.

[15] V. G. Kononov, C. A. Balanis, and C. R. Birtcher, "Field distribution modeling and measurements of ferrite-loaded cbs antennas," *IEEE Radio and Wireless Symposium*, 2011.

[16] C. A. Balanis, *Antenna Theory Analysis and Design*, 3rd ed. New Jersey: John Wiley & Sons, Inc., 2005.

[17] C. A. Balanis, Ed., *Modern Antenna Handbook*. New Jersey: John Wiley & Sons, Inc., 2008.

[18] D. B. Davidson, *Computational Electromagnetics for RF and Microwave engineering*, 2nd ed. New York: Cambridge University Press, 2011.

[19] J. M. Jin and J. L. Volakis, "A hybrid finite element method for scattering and radiation by microstrip patch antennas and arrays residing in a cavity," *IEEE Trans. Antennas Propag.*, vol. AP-39, no. 11, pp. 1598–1604, Nov. 1991.

[20] N. A. Spaldin, *Magnetic Materials Fundamentals and Applications*, 2nd ed. New York: Cambridge University Press, 2011.

[21] *Microwave Magnetic & Dielectric Materials*, Trans-Tech, 5520 Adamstown, MD 21710 USA, E-mail: transtech@alphaind.com, 2007.

[22] R. A. Waldron, *Ferrites an Introduction for Microwave Engineers*. London: D.Van Nostrand Company, Ltd., 1961.

[23] R. F. Soohoo, *Theory and Application of Ferrites.* New Jersey: Prentice Hall, Inc., 1960.

[24] A. J. Baden-Fuller, *Ferrites at Microwave Frequencies.* London: Peter Peregrinus, Ltd., 1987.

[25] M. S. Sodha and N. C. Srivastava, *Microwave Propagation in Ferrimagnetics.* New York: Plenum Press, 1981.

[26] D. K. Cheng, *Field and Wave Electromagnetics*, 2nd ed. New York: Addison-Wisley Publishing Company, Inc., 1989.

[27] G. Bertotti, *Hysteresis in Magnetism for Physicists, Material Scientists, and Engineers.* San Diego: Academic Press, Inc., 1998.

[28] D. Jiles, *Introduction to Magnetism and Magnetic Materials*, 2nd ed. London: Peter Peregrinus, Ltd., 1987.

[29] C. Kittel, "Theory of the dispersion of magnetic permeability in ferromagnetic materials at microwave frequencies," *Physical Review*, vol. 70, no. 5 and 6, pp. 281–290, Sep. 1946.

[30] P. P. Silvester and R. P. Gupta, "Effective computational models for anisotropic soft b-h curves," *IEEE Transactions on Magnetics*, vol. 27, no. 5, pp. 3804–3807, Sep. 1991.

[31] A. Ivanyi, *Hysteresis Models in Electromagentic Computation.* Budapest: Akademiai Kiado, 1997.

[32] I. D. Mayergoyz, *Mathematical Models of Hysteresis.* New York: Springer-Verlag, 1991.

[33] E. D. Torre, *Magnetic Hysteresis.* New Jersey: IEEE Press, 1999.

[34] S. Chikazumi, *Physics of Magnetism.* New York: John Wiley & Sons, Inc., 1964.

[35] C. Kittel, "Interpretation of anomalous larmor frequencies in ferromagnetic resonance experiment," *Physical Review, Letters to the Editor*, vol. 71, pp. 270–271, Jan. 1947.

[36] ——, "On the theory of ferromagnetic resonance absorption," *Physical Review*, vol. 73, pp. 155–161, Jan. 1948.

[37] D. Polder, "On the theory of ferromagnetic resonance," *Phylosophical Magazine Series 7*, vol. 40:300, pp. 99–115, 1949.

[38] P. J. B. Clarricoats, *Microwave Ferrites*. New York: John Wiley & Sons, Inc., 1961.

[39] V. G. Kononov, "Non-uniform field modeling of ferrite-loaded cavity-backed slot antennas," Master's thesis, Arizona State University, Tempe, AZ, 2007.

[40] H.-Y. Yang, J. Castaneda, and N. Alexopoulos, "Surface wave modes of printed circuits on ferrite substrates," *IEEE Trans. on Microwave Theory and Techniques*, vol. 40, no. 4, pp. 613 –621, Apr 1992.

[41] R. I. Joseph and E. Schlomann, "Demagnetizing field in nonelipsoidal bodies," *Journal of Applied Physics*, vol. 36, no. 5, pp. 1579–1593, May 1965.

[42] R. I. Joseph, "Ballistic demagnetizing factor in uniformly magnetized rectangular prisms," *Journal of Applied Physics*, vol. 38, no. 5, pp. 2405–2406, Apr. 1967.

[43] J. Simkin and C. W. Trowbridge, "Three-dimensional nonlinear electromagnetic field computations, using scalar potentials," *IEE Preceedings*, vol. 127, no. 6, pp. 368–374, Nov. 1980.

[44] J. S. Humphries, *Field Solutions on Computers*. New York: CRC Press LLC, 1998.

[45] T. Lyman, Ed., *Metals Handbook*, eigth ed. American Society for Metals, 1961.

[46] H. S. Newman and C. M. Krowne, "Analysis of ferrite circulators by 2-d finite-element and recursivegreen's function techniques," *IEEE Transactions on Microwave Theory and Techniques.*, vol. 46, no. 2, pp. 167–177, Feb. 1998.

[47] E. M. C. P. J. Rivas, J. M. Zamarro, "Simple approximation for magnetization curves and hysteresis loops," *IEEE Trans. Magnetics*, vol. MAg-17, no. 4, pp. 1498–1502, Jul. 1981.

[48] F. Ihlenburg, *Finite Element Analysis of Acoustic Scattering.* New York: Springer, 1998.

[49] U. S. Inan and A. S. Inan, *Engineering Electromagnetics.* California: Addison Wesley Longman, Inc., 1999.

[50] C. Kelley, *Iterative methods for linear and nonlinear equations.* Philadelphia: Society for industrial and Applied Mathematics, 1995.

[51] P. N. Brown and H. F. Walker, "Gmres on (nearly) singular systems," *SIAM J. Matrix Anal. Appl*, vol. 18, no. 1, pp. 37–51, Jan 1997.

[52] J. Shen, "Preconditioned iterative solvers for complex and unsymmetric systems of equations resulting from the hybrid fe-be method." *IEEE Transactions on Magnetics*, vol. 33, no. 2, pp. 1764–1767, Mar. 1997.

[53] D. R. F. Gerald L.G. Sleijpen and H. A. V. der Vorst, "Generalized conjugate gradient squared," *Journal of Computational and Applied Mathematics*, vol. 71, no. 1, pp. 125–146, Jul. 1996.

[54] G. L. Sleijpen and D. R. Fokkema, "Bicgstab(l) for linear equations involving unsymmetric matrices with complex spectrum," *Electronic Transactions in Numerical Analysis*, vol. 1, pp. 11–32, Sep. 1993.

[55] B. M. Irons, "A frontal solution scheme for finite element analysis," *Int. J. Numer. Methods Eng*, vol. 2, pp. 5–32, Mar. 1970.

[56] I. S. Duff and J. K. Reid, "The multifrontal solution of indefinite sparse symmetric linear," *ACM Transactions on Mathematical Software*, vol. 9, pp. 302–325, Sep. 1983.

[57] E. Schlomann, "Microwave behavior of partially magnetized ferrites," *Journal of Applied Physics*, vol. 41, no. 1, pp. 204–214, Jan. 1970.

[58] J. Green and F. Sandy, "Microwave characterization of partially magnetized ferrites," *IEEE Trans. on Microwave Theory and Thechniques*, vol. MTT-22, no. 6, pp. 641–645, Jun. 1974.

[59] M. Igarashi and Y. Naito, "Microwave permeability tensor of partially magnetized ferrites," *Microwave Symposium, 1976 IEEE-MTT-S International*, pp. 269–271, Jun. 1976.

[60] P. Gelin and K. Berthou-Pichavant, "New consistent model for ferrite permeability tensor with arbitrary magnetization state," *IEEE Trans. on Microwave Theory and Thechniques*, vol. 45, no. 8, pp. 1185–1192, Aug. 1997.

Appendix A

FEM FORMULATION

The electric field inside the cavity satisfies the following Helmholtz vector wave equation and the boundary conditions

$$\nabla \times [\mu_r]^{-1} \nabla \times \vec{E} - \beta_o^2 [\varepsilon_r] \vec{E} = 0 \tag{A.1}$$

$$\begin{aligned} &\vec{E}_{tan}(\vec{r} \in \text{ metallic parts}) = 0 \\ &\vec{E}(\vec{r} \in \text{ aperture}) = \vec{E}_a \\ &\vec{E}(\vec{r} \in \text{ coax excitation plane}) = E^{inc} + E^{ref} \end{aligned} \tag{A.2}$$

The Finite Element Method scheme to solving this problem is the following.

a) Assume approximate solution $\vec{E} \simeq \widetilde{\vec{E}}$ and form the residual $\vec{R}$

$$\vec{R} = \nabla \times [\mu_r]^{-1} \nabla \times \widetilde{\vec{E}} - \beta_o^2 [\varepsilon_r] \widetilde{\vec{E}} \tag{A.3}$$

b) Set the average of the weighted residual to zero, that is $\int \vec{N} \cdot \vec{R} d\Omega = 0$. Using integration by parts write (A.1) in the weak form

$$\int_\Omega (\nabla \times \vec{N}) \cdot ([\mu_r]^{-1} \nabla \times \widetilde{\vec{E}}) - \beta_o^2 \vec{N} \cdot ([\varepsilon_r] \widetilde{\vec{E}}) d\Omega = \oint_S (\hat{n} \times \vec{N}) \cdot ([\mu_r]^{-1} \nabla \times \vec{E}) dS \tag{A.4}$$

where $\vec{N}$ is the weighting function, Ω and S denote the volume of interest and the surface enclosing that volume, respectively, and $\hat{n}$ is the outwardly directed unit vector normal to S.

c) If necessary, manipulate/simplify (A.4). For our problem, the boundary conditions (A.2) indicate that the surface integral on the right-hand side (RHS) of (A.4) is non-zero only over the aperture and the coaxial cable excitation plane. Therefore, the RHS can be written as

$$\begin{aligned} \oint_S (\hat{n} \times \vec{N}) \cdot ([\mu_r]^{-1} \nabla \times \vec{E}) dS \; &= \int_{S_{aper}} (\hat{n} \times \vec{N}) \cdot ([\mu_r]^{-1} \nabla \times \vec{E}) dS \\ &+ \int_{S_{coax}} (\hat{n} \times \vec{N}) \cdot ([\mu_r]^{-1} \nabla \times \vec{E}) dS \end{aligned} \tag{A.5}$$

The quantity $\nabla \times \vec{E}$ in the first integral on the RHS is given by (5.1). Thus,

$$\int_{S_{aper}} (\hat{n} \times \vec{N}) \cdot ([\mu_r]^{-1} \nabla \times \vec{E}) dS = 2\beta_o^2 \int_{S_{aper}} (\hat{n} \times \vec{N}) \cdot \left([\mu_r]^{-1} \int_{S_{aper}} [\hat{a}_z \times \widetilde{\vec{E}}] \cdot \overline{\vec{G}}_o dS' \right) dS \tag{A.6}$$

The second integral in (A.4) requires some manipulations. Consider Figure A.1 depicting the coaxial cable and the coax-cavity interface. For simplicity of the discussion, the coordinate system is rotated so that the z axis coincides with the

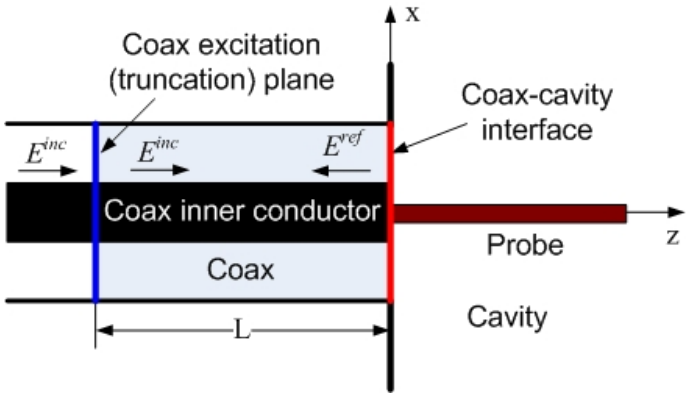

Figure A.1: Coaxial cable and coax-cavity interface.

axis of the coaxial cable. In the FEM model, the coaxial cable is truncated at a distance L from the coax-cavity interface. This truncation plane serves as the excitation plane for the problem. Although the field distribution at this point is, in general, not known, it can be written as the superposition of the incident and reflected fields, $E = E^{inc} + E^{ref}$. The incident field is the known field distribution excited in the coaxial cable during the physical experiment, usually it is the dominant TEM mode. The dominant mode propagates towards the coax-cavity interface where it is partially reflected back. In addition, the coax-cavity discontinuity results in creation of multiple higher-order modes. Thus, the field E^{ref} is the superposition of the reflected dominant mode and the higher-order modes. However, the dimensions of the coaxial cable and the frequency of operation ($\simeq 1$ GHz) are such that the higher-order modes are non-propagating and exist only in the vicinity of the discontinuity. Thus, provided that the length L is long enough, the only mode reaching the excitation plane is the propagating reflected dominant mode. In cylindrical coordinates, the dominant TEM mode of a coaxial transmission line is given by

$$\vec{E}^{inc} = \hat{a}_\rho \frac{E_o}{\rho} e^{-\gamma z} \tag{A.7}$$

where, E_o is the amplitude of the electric field, $\gamma = \alpha + \jmath\beta_z$, α is the attenuation constant, $\beta_z = \beta_o\sqrt{\epsilon_r \mu_r}$ is the coax wave number, and (ϵ_r, μ_r) are the relative permittivity and permeability of the coaxial cable, respectively. The total field at the excitation plane can be written as

$$\vec{E} = \vec{E}^{inc} + \vec{E}^{ref} = \hat{a}_\rho \frac{E_o}{\rho}(e^{-\gamma z} + Re^{\gamma z}) \tag{A.8}$$

where R represents the reflection coefficient. Taking the curl of (A.8), we obtain

$$\begin{aligned} \nabla \times \vec{E} &= \hat{a}_\phi \gamma \frac{E_o}{\rho}(-e^{-\gamma z} + Re^{\gamma z}) \\ &= \hat{a}_z \times \hat{a}_\rho \gamma \frac{E_o}{\rho}(-e^{-\gamma z} + Re^{\gamma z}) \\ &= \hat{a}_z \times \gamma(\vec{E} - 2\vec{E}^{inc}) \end{aligned} \tag{A.9}$$

Then, the second integral in (A.4) becomes

$$\begin{aligned} \int_{S_{coax}} (\hat{n} \times \vec{N}) \cdot ([\mu_r]^{-1} \nabla \times \vec{E}) dS &= \gamma \int_{S_{coax}} (\hat{n} \times \vec{N}) \cdot ([\mu_r]^{-1} (\hat{n} \times \widetilde{\vec{E}}) dS \\ &\quad -2\gamma \int_{S_{coax}} (\hat{n} \times \vec{N}) \cdot ([\mu_r]^{-1} (\hat{n} \times \vec{E}^{inc}) dS \end{aligned} \tag{A.10}$$

where $\hat{a}_z$ was replaced by $\hat{n}$ which in this integral is the unit normal vector to the coax excitation plane. Then, substituting (A.10) and (A.5) in (A.3) we get

$$\begin{aligned} &\int_\Omega (\nabla \times \vec{N}) \cdot ([\mu_r]^{-1} \nabla \times \widetilde{\vec{E}}) - \beta_o^2 \vec{N} \cdot ([\varepsilon_r] \widetilde{\vec{E}}) d\Omega \\ &-\gamma \int_{S_{coax}} (\hat{n} \times \vec{N}) \cdot ([\mu_r]^{-1} \hat{n} \times \widetilde{\vec{E}}) dS \\ &-2\beta_o^2 \int_{S_{aper}} (\hat{n} \times \vec{N}) \cdot \left([\mu_r]^{-1} \int_{S_{aper}} (\hat{n} \times \widetilde{\vec{E}}) \cdot \overline{\overline{G}}_o dS' \right) dS \\ &= -2\gamma \int_{S_{coax}} (\hat{n} \times \vec{N}) \cdot ([\mu_r]^{-1} \hat{n} \times \vec{E}^{inc}) dS \end{aligned} \tag{A.11}$$

If the whole domain Ω is discretized into elements and inside each element the solution is assumed to be of the form

$$\vec{E}^e = \sum_{j=1}^{T} \vec{N}_j^e E_j^e \tag{A.12}$$

where N_j^e are the interpolation functions and E_j^e are the unknown expansion coefficients representing the magnitude of the electric field along the edges of an element, and T is the number of the unknown coefficients; if the zeroth order tetrahedral elements are used, then T is six [7]. Thus, for each element e, (A.11) can be written in the form of a $(T \times T)$ matrix

$$[K^e + Y^e + B^e]\{E^e\} = \{b^e\} \tag{A.13}$$

where

$$K^e = \int_{\Omega^e} (\nabla \times \vec{N}_i) \cdot ([\mu_r]^{-1} \nabla \times \vec{N}_j) - \beta_o^2 \vec{N}_i \cdot ([\varepsilon_r] \vec{N}_j) d\Omega^e \quad \text{(A.14)}$$

$$Y^e = -2\beta_o^2 \int_{S^e_{aper}} (\hat{n} \times \vec{N}_i) \cdot \left([\mu_r]^{-1} \int_{S^e_{aper}} (\hat{n} \times \vec{N}_j) \cdot \overline{\vec{G}}_o dS'^e \right) dS^e \quad \text{(A.15)}$$

$$B^e = -\gamma \int_{S^e_{coax}} (\hat{n} \times \vec{N}_i) \cdot ([\mu_r]^{-1} \hat{n} \times \vec{N}_j) dS^e \quad \text{(A.16)}$$

$$b^e = -2\gamma \int_{S^e_{coax}} (\hat{n} \times \vec{N}_i) \cdot ([\mu_r]^{-1} \hat{n} \times \vec{E}^{inc}) dS^e \quad \text{(A.17)}$$